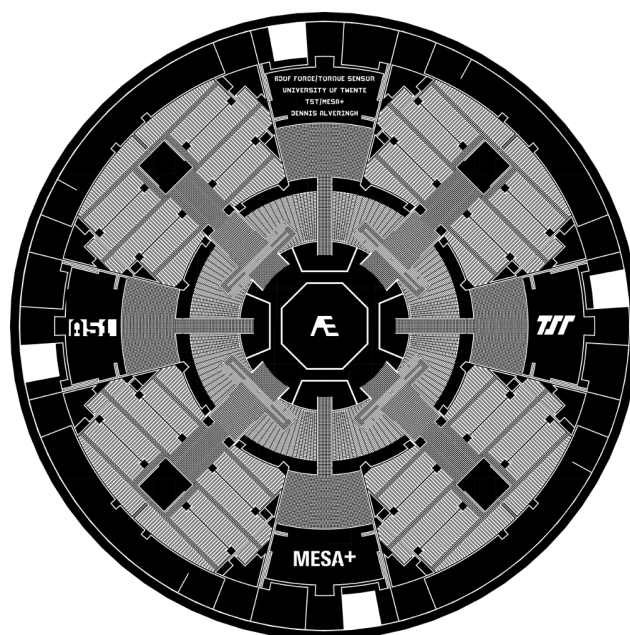


University of Twente  
MESA+ Institute for Nanotechnology  
Faculty of Electrical Engineering, Mathematics and Computer Science  
Department of Electrical Engineering  
Transducer Science and Technology Research Group

---

The Documentation  
of  
A Large Range Multi-Axis Capacitive Force/Torque Sensor Using a  
Single SOI Wafer by Alveringh et al.

---



---

*Author*  
Dennis Alveringh

*Committee*  
dr. ir. Remco Wiegink  
Robert Brookhuis MSc  
prof. dr. ir. Gijs Krijnen  
ing. Meint de Boer  
prof. dr. ir. Peter Veltink

---

*The frontpage shows the layout of the sensing structures of the sensor that will be described in this documentation.*

---

### **Abstract**

A miniature silicon capacitive force/torque sensor is designed and realized to be used for biomechanical applications and robotics. The sensor is able to measure the forces in three directions and two torques using four parallel capacitor plates and four comb-structures. Novel spring and lever structures are designed to separate the different force components and minimize crosstalk. The highly reproducible fabrication process is based on deep reactive ion etching of the two outer layers of a single silicon-on-insulator wafer and uses only two masks. The sensor has a force range of 2 N in shear and normal direction and a torque range of more than 6 N mm. It has a high sensitivity of 38 fF N<sup>-1</sup> and 450 fF N<sup>-1</sup> in shear and normal direction respectively. A calibration matrix is derived from the sensor's measured characteristics.

# Contents

<b>Introduction</b>	<b>1</b>
<b>1 Literature study</b>	<b>3</b>
1.1 Introduction . . . . .	4
1.2 Capacitive force sensors with silicon springs . . . . .	6
1.3 Capacitive force sensors with polymer springs . . . . .	12
1.4 Piezoresistive force sensors with silicon springs . . . . .	18
1.5 Piezoresistive force sensors with polymer springs . . . . .	22
1.6 Conclusion . . . . .	24
<b>2 Theory</b>	<b>25</b>
2.1 Introduction . . . . .	26
2.2 Concepts for a six degrees of freedom stage . . . . .	27
2.3 Concepts for sensing structures . . . . .	31
2.4 Mathematical model . . . . .	32
2.5 Design of the suspended core . . . . .	38
2.6 Design of the sensing structures . . . . .	41
2.7 Conclusion . . . . .	45
<b>3 Fabrication</b>	<b>47</b>
3.1 Introduction . . . . .	48
3.2 Design of the fabrication process . . . . .	49
3.3 Fabrication report . . . . .	55
3.4 Discussion and conclusion . . . . .	59
<b>4 Characterization</b>	<b>61</b>
4.1 Introduction . . . . .	62
4.2 Characterization of the suspended core . . . . .	63
4.3 Characterization of the sensor . . . . .	65
4.4 Discussion and conclusion . . . . .	68
<b>Conclusion</b>	<b>70</b>
<b>References</b>	<b>71</b>
<b>List of figures</b>	<b>74</b>
<b>A Symbols, quantities and constants</b>	<b>77</b>
<b>B Paper for publication</b>	<b>80</b>
<b>C Conference abstract</b>	<b>91</b>
<b>D Technical fabrication process document</b>	<b>94</b>

## Introduction

This documentation consists of four parts and several appendices that contain the details of the sensor proposed in the paper by Alveringh et al. [1]: A Large Range Multi-Axis Capacitive Force/Torque Sensor Realized in a Single SOI Wafer. It can be seen as an extension of the paper to provide details about the design, explain design choices and help reproducing the sensor.

This documentation is divided in four parts: theory, fabrication, characterization and literature study. Each part is a stand-alone report including an introduction and conclusion. The part ‘theory’ describes different concepts, a derivation of the mathematical model of the chosen concept and the details of all the design steps of the sensor. The part ‘fabrication’ describes the theory and the design of the fabrication steps and provides a report of the actual process. The part ‘characterization’ describes the measurement setup and results that characterizes the sensor. The part ‘literature study’ describes several other force/-torque sensors using different technologies.

This documentation ends with an overall conclusion. The paper for publication, the conference abstract and the technical fabrication process document are included in the appendices.

---

## Introduction to the subject

Miniaturized multi-axis force/torque sensors are widely used in medical applications, tactile sensing and robotics. Many prostheses, for example, require safe and comfortable interaction with people who underwent amputation of a part of a limb. Bad fitting between the socket of the prosthesis and the residual limb may cause pain and even damage to the underlying blood vessels [28, 25]. Measuring the shear forces and normal forces between the socket and the residual limb is possible with multiple small force sensors. The socket of the prosthesis can use this information to adjust the shape of the socket, making the load distribution as comfortable and healthy as possible.

Other applications are in the field of characterization of the human body. For example, power measurements of the human hand are important for rehabilitation purposes or the optimization of the endurance of athletes [39]. These power measurements can be done with force/torque sensors, accelerometers and gyroscopes at each joint integrated in a glove (figure 1).

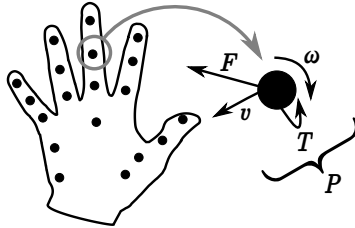


Figure 1: Power measurements of the human hand using force sensors, accelerometers and gyroscopes. The power  $P$  in one element is equal to  $\vec{F} \cdot \vec{v} + \vec{T} \cdot \vec{\omega}$ .

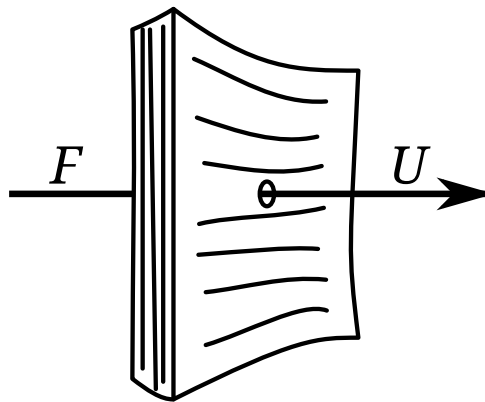
Force sensors are also very interesting for robotics. Humanoid robots [19] or robotic hands [8] have to interact with the environment. Force sensors on top of the fingers and toes help the robot to measure load distributions on the hands and feet. Even the difference between rough and flat surfaces may be sensed by the robot.

For the three mentioned applications, a few specific requirements are applicable:

- the sensor should measure multiple (preferably six) degrees of freedom;
- the sensor is small, preferably less than  $1 \text{ cm}^2$  with a thickness of less than 1 mm;
- the sensor should be able to handle human forces, i.e. at least a few newtons.

Commercially available non-MEMS load cells support high force ranges, but are often too large to integrate in the applications mentioned above. There are MEMS-based force and torque sensors available in literature, but many lack the support for measuring torques [13, 21] or forces [2]. Besides, many sensors only support forces in the milli newton or micro newton range [10, 29, 24]. The fabrication process of most MEMS-based sensors is still in an experimental stage [13, 21, 24, 36, 6], they use non-trivial polymer technologies or crucial wafer bonding steps in the process. The latter property makes the existing force sensors even less attractive, since above specified applications need tens of these expensive sensors per device.

However, a few force/torque sensors with piezoresistive readout satisfy most of the requirements. But sensors with capacitive readout have a better temperature performance, lower drift and higher sensitivity [33]. We present a miniature easy to fabricate multi-axis capacitive force/torque sensor with a large range. The sensor is initially developed for quantitative measurement of the interaction forces and torques between human fingers and the environment as a cheaper alternative for the sensor of Brookhuis et al. [6] But given its large force range and small dimensions, the sensor can also be used for other biomechanical applications or robotics.



---

*Author*  
Dennis Alveringh

*Supervised by*  
dr. ir. Remco Wiegerink  
Robert Brookhuis MSc

## 1.1 Introduction

This literature study is originally done as a preliminary exploration for the design and fabrication of a microelectromechanical system (MEMS) based force/torque sensor. The purpose of this part at the end of this documentation is to give a context for the realized sensor.

This literature study describes state-of-art MEMS force sensors with their performance, range, construction and fabrication. A selection is made based on the following two conditions:

- it uses fabrication technology existing in the MESA+ nanolab of the University of Twente, e.g. bulk micromachining in silicon, wafer bonding and polymer deposition;
- the sensor should have at least one characteristic, and therefore inspiring, property for tactile sensing, i.e. there should be support for multiple degrees of freedom and/or a large range of force.

This part starts with a section where four different categories of sensors will be outlined. This part continues with brief summaries of the papers ordered per category. Especially the performance of the sensors, the design and the fabrication will be summarized. The author chose for small summaries of many different papers instead of extensive analyses of just a few papers.

### Types of force/torque sensors

All force sensors in this part use the operating principle described in figure 1.1. A force is applied on a spring system which causes a displacement in the sensor structure. The sensing structures produce an electric quantity at the output (e.g. voltage, capacitance or resistance) directly dependent of the displacement.

Bell et al. of reference [3] published in 2005 an overview of the characteristics of actuators, force sensors and displacement sensors that were published last years. Since force sensors are most interesting for this study, only the results for the sensors will be shown here. Bell et al. divided the sensors in different working principles (capacitive and piezoresistive for example) and plotted the resolution and frequency in diagrams dependent of the force.

It seems that using capacitance as readout method is not common for forces above 1 mN, most designers chose for piezoelectric or piezoresistive materials in this range. But in fact, there are papers ([6] and [13] for example) published after this paper of Bell et al. with a capacitive readout and support for forces above 1 mN.

Although Bell et al. described more categories, this part has only four categories of MEMS sensors that can be made with the existing technology in the MESA+ nanolab. Table 1.1 shows the four categories and their corresponding section in the part.

Table 1.1: Four types of force/torque sensors

	Silicon	Polymer
Capacitive	Section 1.2	Section 1.3
Piezoelectric	Section 1.4	Section 1.5

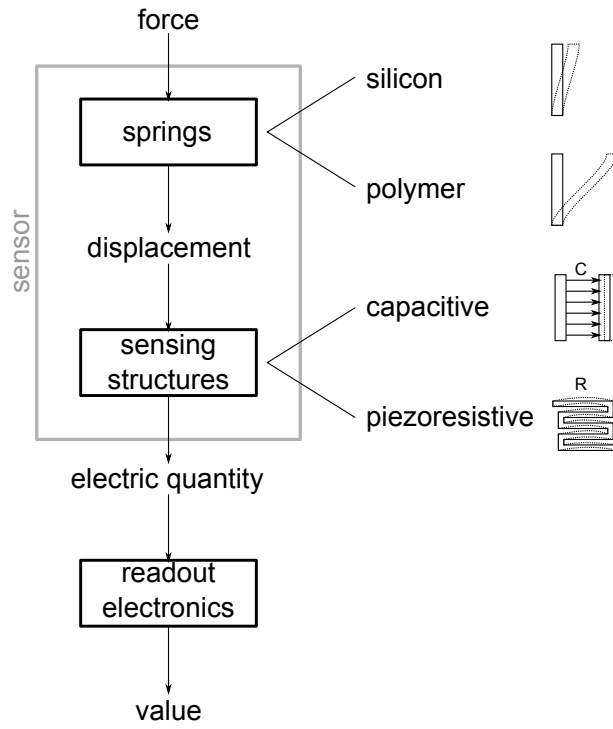
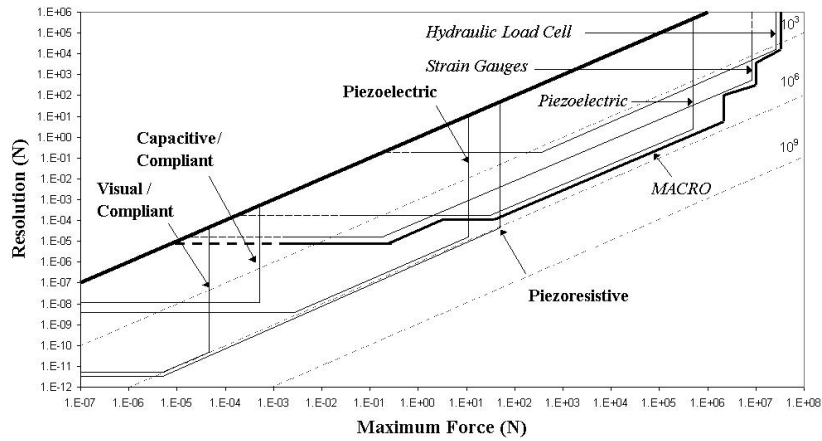
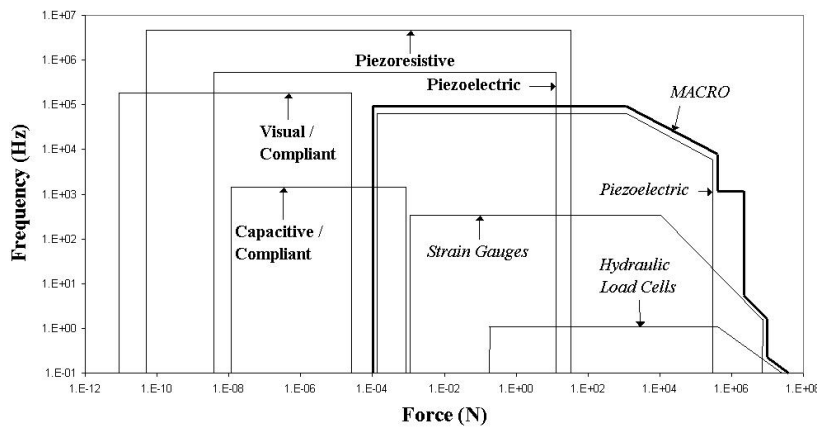


Figure 1.1: Common operating principle of MEMS force sensors.



(a) Resolution versus maximum force of sensors.



(b) Frequency versus force of sensors.

Source: Bell et al. [3]

Figure 1.2: MEMS actuators and sensors: observations on their performance and selection for purpose from Bell et al.

## 1.2 Capacitive force sensors with silicon springs

Capacitive force sensors are using a change in capacitance as measurement for force, caused by a closing/opening gap between or change in overlapping area of electrodes. Silicon is used for the springs of all sensors in this section. It has a high Young's modulus and yield strength compared to polymers and many metals. Silicon is able to survive high stresses and is therefore a suitable material for large range force sensors. This section describes several sensors using a silicon spring system and capacitive readout.

Wiegerink et al. presented a silicon based capacitive load cell [42] in 2000 that was able to measure loads up to 10 kN. The sensor consists of a top and bottom electrode separated by a spring. A normal force results in a reducing change in gap and increasing capacitance between the two electrodes. The spring consists of several silicon pillars that can be compressed. The electrodes are located between the pillars. The structures were made in two wafers which were bonded together.

Brookhuis et al. of the same research group developed a more advanced version of the sensor in 2012. The paper in reference [6] presents a force sensor that is capable of measuring normal force and torque around two axes. Even though the sensor has multiple degrees of freedom, it can handle large forces: 50 N of normal force and moments can be measured up to 25 N mm and is therefore proposed as a sensor for biomechanical applications. The sensor uses the same spring system as Wiegerink et al., but now the pillars can bend to make shear displacements possible. The bottom electrode consists of four quadrants to distinguish the different directions.

Fabrication is done using a highly doped silicon top wafer and a silicon on insulator (SOI) bottom wafer. Deep reactive ion etching (DRIE) is used to create the pillar spring elements. The bonding of the wafers is based on silicon fusion bonding.

The sensor has a sensitivity of  $16 \text{ pF N}^{-1}$  in normal direction and  $2.7 \text{ pF N}^{-1} \text{ mm}$  for applied torques. The sensor was improved in the same year to a six degrees of freedom sensor with support for shear forces up to 10 N [7].

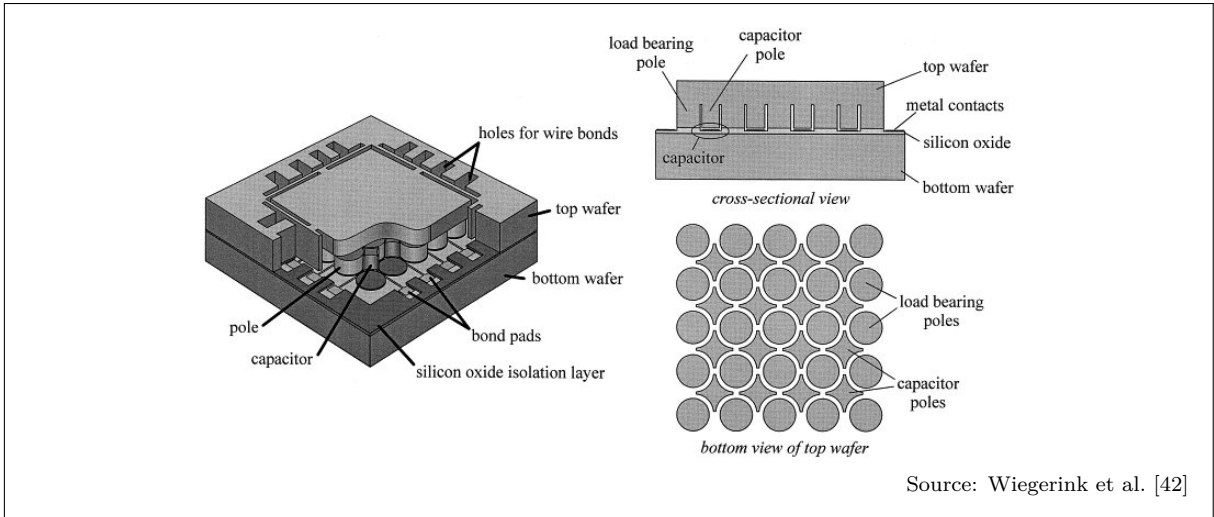


Figure 1.3: The quasi-monolithic silicon load cell for loads up to 1000 kg with insensitivity to non-homogeneous load distributions from Wiegerink et al.

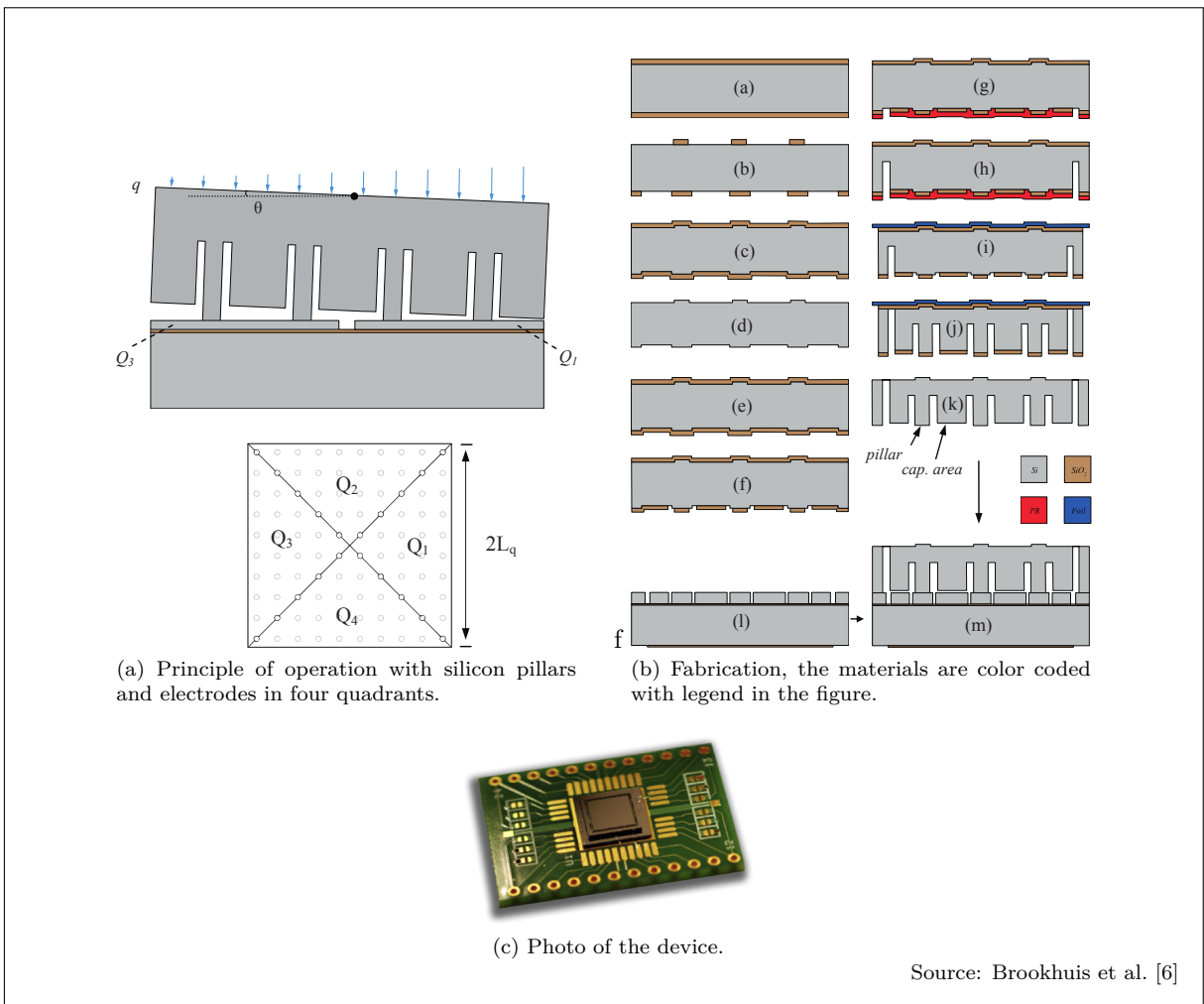


Figure 1.4: The 3D force sensor for biomechanical applications from Brookhuis et al.

As Brookhuis et al. uses parallel plate capacitors and springs under the end-effector, Sun et al. proposes a completely different sensor in 2002. This sensor is two degrees of freedom and has edge-supported springs. It has comb-structures in two orientations to measure two shear forces. It is developed for purposes as biomaterial characterization and material science.

The same research group improved the design with Beyeler et al. in 2009 by making the sensor capable of measuring in six degrees of freedom up to 1000  $\mu\text{N}$  for translations and 2.6 mN mm for rotations with micro-newton and nano-newtonmeter resolution respectively. This sensor consists of a movable body of silicon supported by four springs in the same horizontal plane. Multiple capacitors are used for readout and determine the direction of displacement of the movable body. Parallel plate capacitors parallel to the body and the bulk change in gap due to normal forces and torques and can be measured differentially. Finger shaped capacitors change in gap by in-plane movements and can be measured differentially.

The bottom layer is patterned with electrodes and support for the top layer. The top layer consists of a second wafer bonded to the support of the bottom layer. The finger shaped capacitors and the springs are made in the top layer by DRIE.

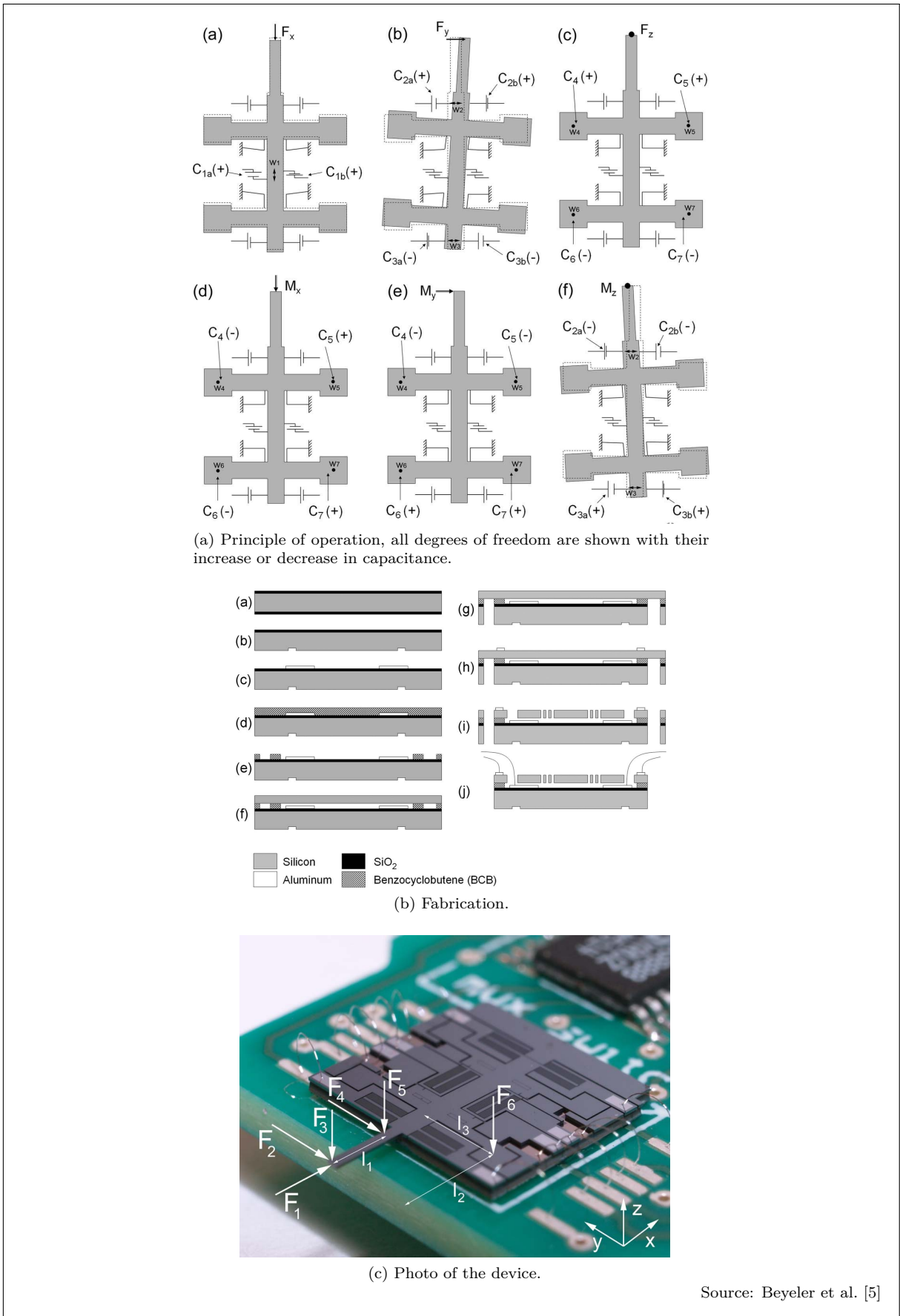


Figure 1.5: A six-axis MEMS force-torque sensor with micro-Newton and nano-Newtonmeter resolution from Beyeler et al.

The earlier described sensors are six degrees of freedom sensors. Following sensors are only one degree of freedom sensor, but have other unique properties.

The sensor of Chu et al. published in 2007 [10] has an overall dimension of 3.6 mm by 1 mm by 10  $\mu\text{m}$  and is designed for purposes as micro-assembly and living cell manipulations. This sensor measures force in one direction, but has thanks to a displacement reduction mechanism and finger-shaped capacitors a very high accuracy. The maximum force is 11 mN. The capacitance change with this force is about 175 fF to 200 fF. The sensor consists of a lever system that reduces the displacement due to the applied force and transforms it to a horizontal displacement moving two set of combs closer to the anchored combs. This increases the capacitance.

Fabrication is started by patterning and etching a glass wafer. Then, single crystal silicon is anodically bonded to the glass wafer. A metal layer is deposited for better electrical conductivity. The silicon with metal is etched to form the device.

Muhammad et al. made in 2011 a sensor with multiple elements of one degree of freedom and with support to forces up to 24 mN. It is developed for a biomimetic fingerpad. Typical of the sensor is the very cost-efficient fabrication. Each element consists of an edge supported stage. Bending of the stage causes a closing gap and increasing capacitance.

The fabrication is done in a SOI wafer. The device layer is etched using DRIE and a release etch was performed to release the stage. Gold is evaporated on the chip to form good contacts for wire bonding. Wire bonding was done on both layers of the SOI wafer as can be seen in figure 1.7b.

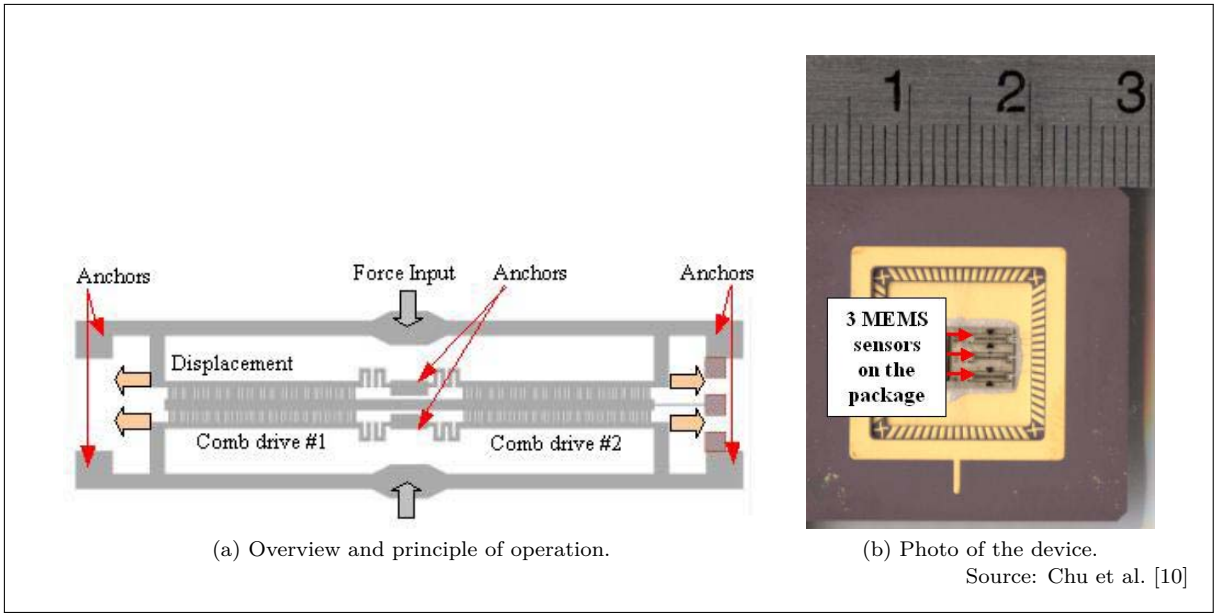


Figure 1.6: Design of a high sensitivity capacitive force sensor from Chu et al.

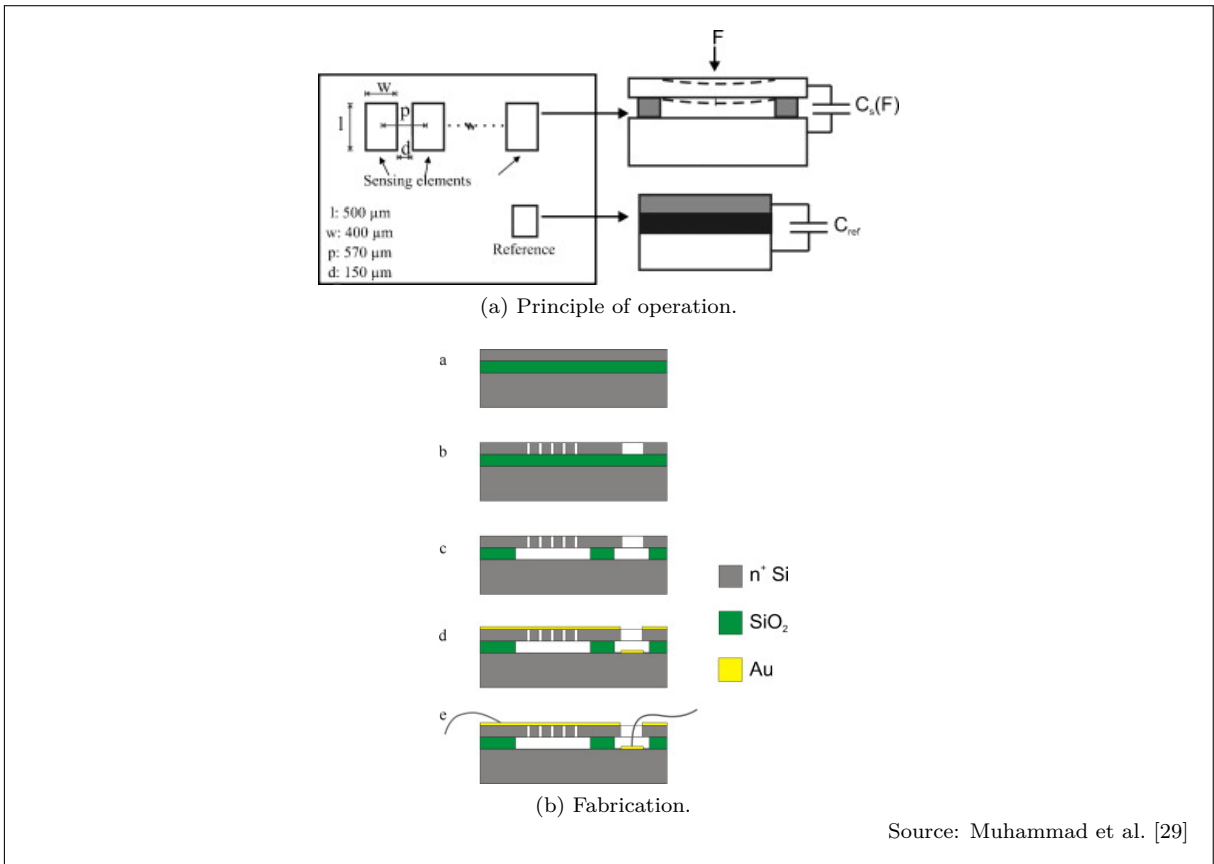


Figure 1.7: Development of a bioinspired MEMS based capacitive tactile sensor for a robotic finger from Muhammad et al.

### 1.3 Capacitive force sensors with polymer springs

The paper in [27] by Lötters et al. describes as one of the first papers (1999) the polymer polydimethylsiloxaan (PDMS) as a mechanically interesting material for MEMS. It begins with mechanically interesting facts about PDMS: it's unique flexibility between 100 kPa and 3 MPa for example. The experiments with the results that are proposed in this paper are mainly about the performance of PDMS when it comes to usage in microfabrication. PDMS was spun upon wafers with varying speeds between 1000 rpm and 5000 rpm with 20 s and 60 s spin time. The coating was exposed to UV light and was cross linked. The thickness dependent on the speed and time are plotted in figure 1.8a. The shear modulus dependent on the frequency (figure 1.8b) and temperature (figure 1.8c) are measured using two discs with PDMS between them. A torque is applied on one of the discs and the movement due to this torque is measured. It appears that the frequency has no effect on the shear modulus. The temperature has a linear positive effect on the shear modulus. The adhesion of PDMS on silicon oxide after using a primer (TMSM) is very good following to Lötters et al. It was not possible to separate the PDMS from the silicon with manual peel tests. Adhesive strenghts up to 180 kPa with PDMS on a polished surface were measured.

Although Lötters et al. gave essential mechanical information about PDMS, the stress-strain relationship and it's linearity for high stresses is not inspected. Wang [41] did measurements for a graduation project in 2011 on several types of PDMS. A setup was made with weights to apply force, a scale under the sample to measure the applied force and a gauge above the sensor to measure the deformation, see also figure 1.9a. The obtained compressive stress-strain relation was linear for relative large stresses as can be seen in figure 1.9b. The printed figure is for one of the types of PDMS, but all tested PDMS types had a linear stress-strain curve.

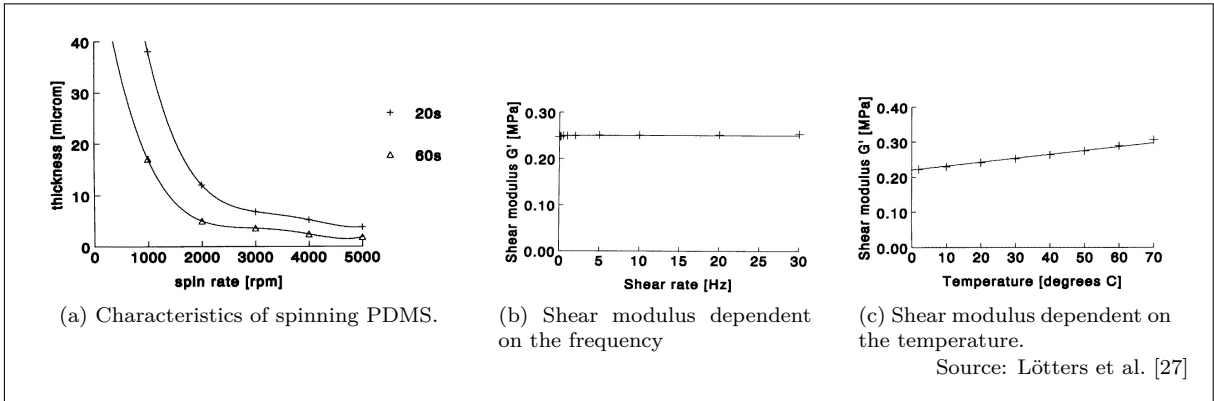


Figure 1.8: The mechanical properties of the rubber elastic polymer polydimethylsiloxane for sensor applications from Lötters et al.

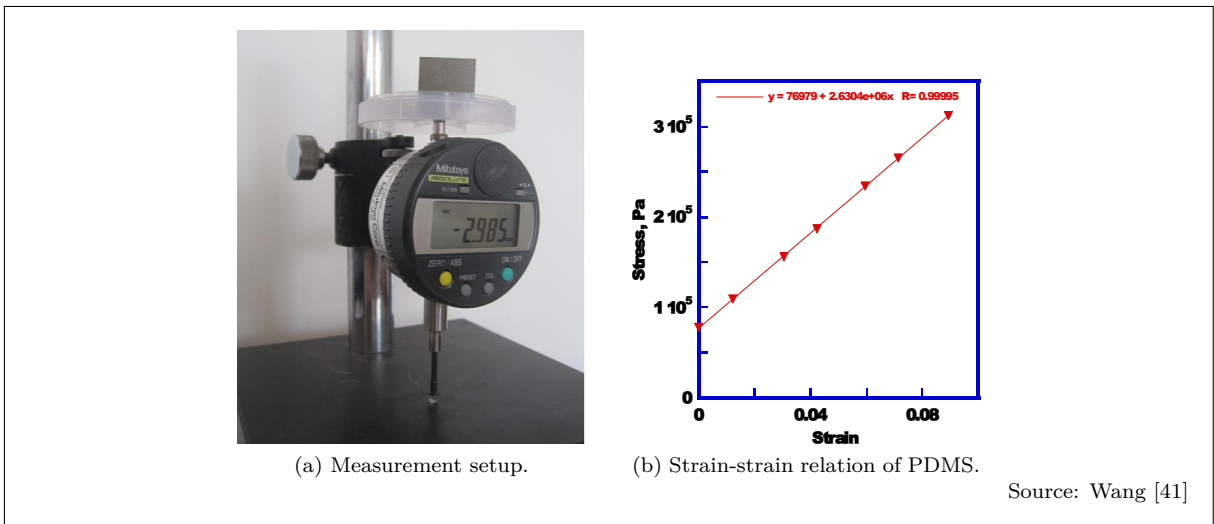


Figure 1.9: Polydimethylsiloxane Mechanical Properties Measured by Macroscopic Compression and Nanoindentation Techniques from Wang

SU-8 is another polymer that may be used as spring material for force sensors. Its Young's modulus is much higher than the one of PDMS (more than  $4 \cdot 10^3$  times higher). However, SU-8 can be patterned with very high aspect ratios. There is a bonding step needed to mount the end-effector of the sensor to the SU-8 pattern. This crucial fabrication step is analyzed in literature.

Pan et al. [32] patterned several materials on two silicon wafers with photolithography in 2002. The two wafers were bonded using the commercial available EV501 bonder. There is no voltage applied to the wafers. The bonding temperature and the bonding force are varied and the effects of these parameters are shown in figure 1.10b and figure 1.10c respectively. It is concluded in the paper that SU-8 is a very good bonding material due to its epoxy feature. There is also concluded that a layer thickness of 100  $\mu\text{m}$  is possible.

An example of an early force sensor using a flexible spring system can be found in reference [9], already in 1995. Chase and Luo proposed a relative simple sensor design using a flexible layer enclosed by two capacitor plates. The sensor is capable of measuring normal and shear force. The range of operation is unknown for the authors only provide the displacement information of their sensor. The sensor consists of four bottom capacitor plates and a floating top capacitor plate. The plates are made on polyimide (PI) layers. Unfortunately, it is not given what the real spring material is.

An example of the full design process of a sensor based on PDMS can be found in reference [24] of 2008. The sensor is made for robotics and prosthetics. Lee et al. explains the design, fabrication and measurements of a force sensor with PDMS as spring material. A four by four array of these sensors was used to determine the range of 10 mN with sensitivities of  $2.5\% \text{mN}^{-1}$ ,  $3.0\% \text{mN}^{-1}$ , and  $2.9\% \text{mN}^{-1}$  for the x-, y-, and z-directions, respectively. The sensor's principle of operation is based on four air gaps in a polymer (PDMS). The polymer is flexible making the air gaps able to be compressed. There are capacitor plates above and below each air gap. Differential change in capacitance can be used to measure shear forces and common change in capacitance can be used to measure the normal force.

Silicon wafers were used as a mold for the PDMS layer. Three PDMS layers, one with the bumps on top, one with the top electrodes and one with the bottom electrodes, are bonded together and form the complete device.

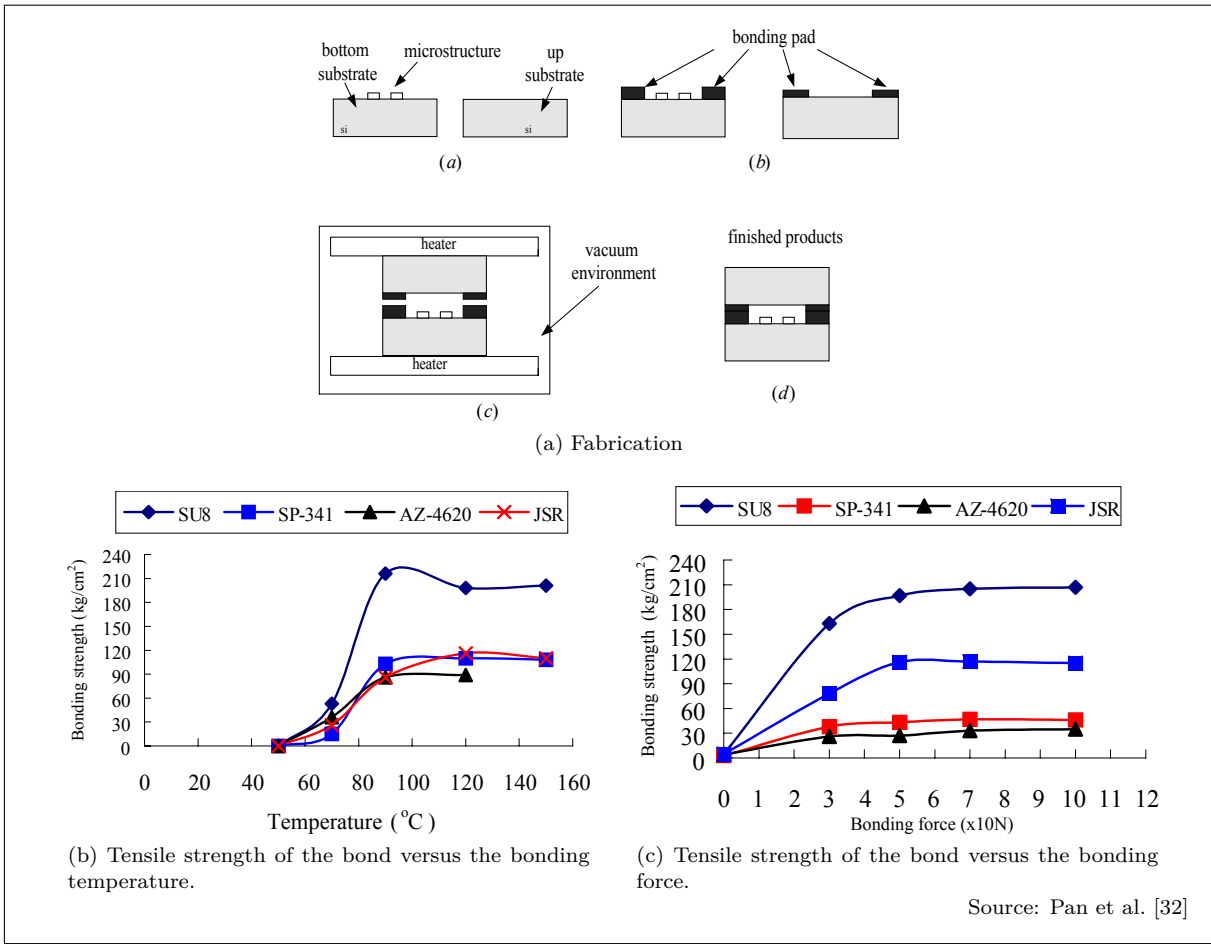


Figure 1.10: A low-temperature wafer bonding technique using patternable materials from Pan et al.

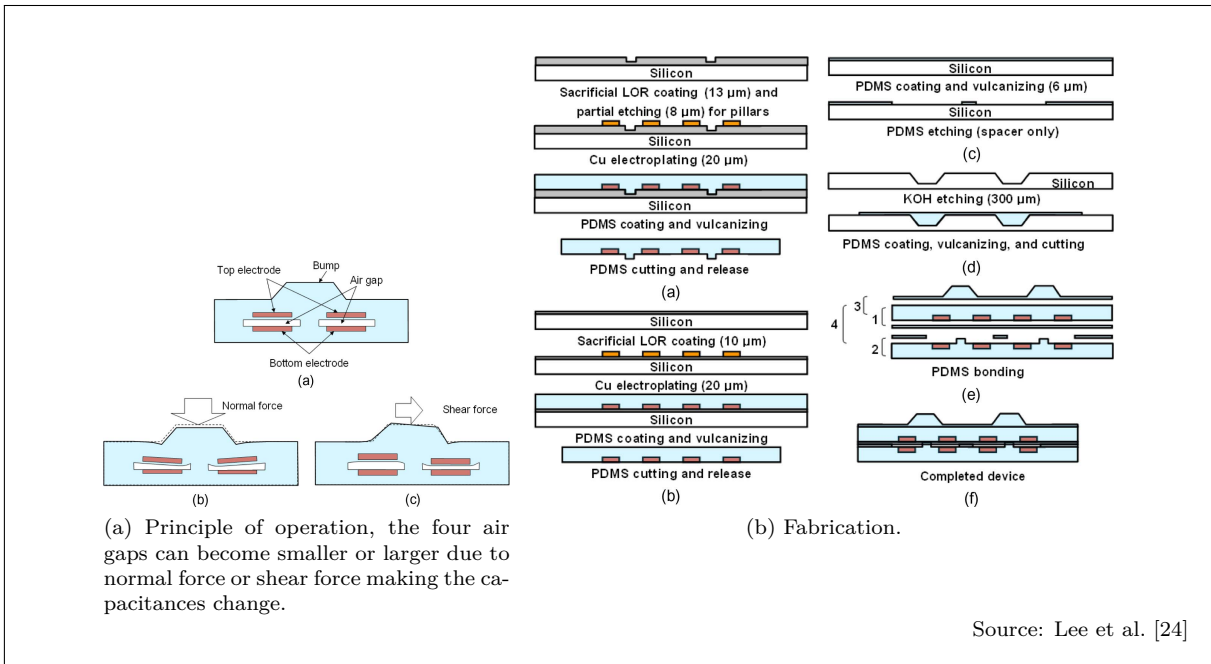


Figure 1.11: A normal and shear force measurement using a flexible polymer tactile sensor with embedded multiple capacitors from Lee et al.

The sensor of reference [13] by Dobrzynska and Gijs in 2010 uses PI as spring material and has the ability to measure in one degree of freedom (normal force). Because of the higher stiffness of PI compared to the more trivial PDMS as spring material, the sensor can handle much higher forces: Dobrzynska and Gijs measured until 3 kN with a sensitivity of approximately  $1 \text{ fF N}^{-1}$ . The goal for this sensor is that it will become a part of a measurement system for feet. Two levels of finger-like conducting microstructures form four redundant capacitors. The whole sensor is embedded in PI. The two levels of microstructures come closer when a force is applied. The bond pads are on the lower level; the authors made a via from the higher to the lower level.

The fabrication starts with a sacrificial layer of aluminum. PI was spun on top of this layer. Then, the lower electrode was sputtered. The second layer of PI was spin coated and using a photoresist with a smooth slope, a slope was etched in the top layer of PI. The second electrode with via was sputtered after this. And finally, the last layer of PI was spun, openings for bond pads were etched and the sacrificial layer with wafer were removed.

Sensors with the measurement electronics on the same chip are not very common. Hence, one summary of such a sensor might be a good addition to this literature study. Liu et al. with the paper in reference [26] of 2011 describe the combined process of the fabrication of the micro mechanics in combination with CMOS<sup>1</sup>. The designers measured the sensors with different thicknesses of the flexible layer, the most robust sensor had a range of 2.4 mN and a sensitivity of  $1.5 \text{ mV mN}^{-1}$ . The sensor works simply with multiple floating capacitor plates buried in PDMS arranged in a circular formation. Capacitor plates below the polymer are connected to the readout electronics made of CMOS.

The whole sensor is made using surface micromachining. The designers did not do the CMOS process themselves, this is done by an external company. Fabrication of the capacitor plates is done in the CMOS process. The holes are etched and the PDMS polymer is cast between the capacitor plates by the designers themselves.

---

<sup>1</sup>Complementary metal oxide semiconductor

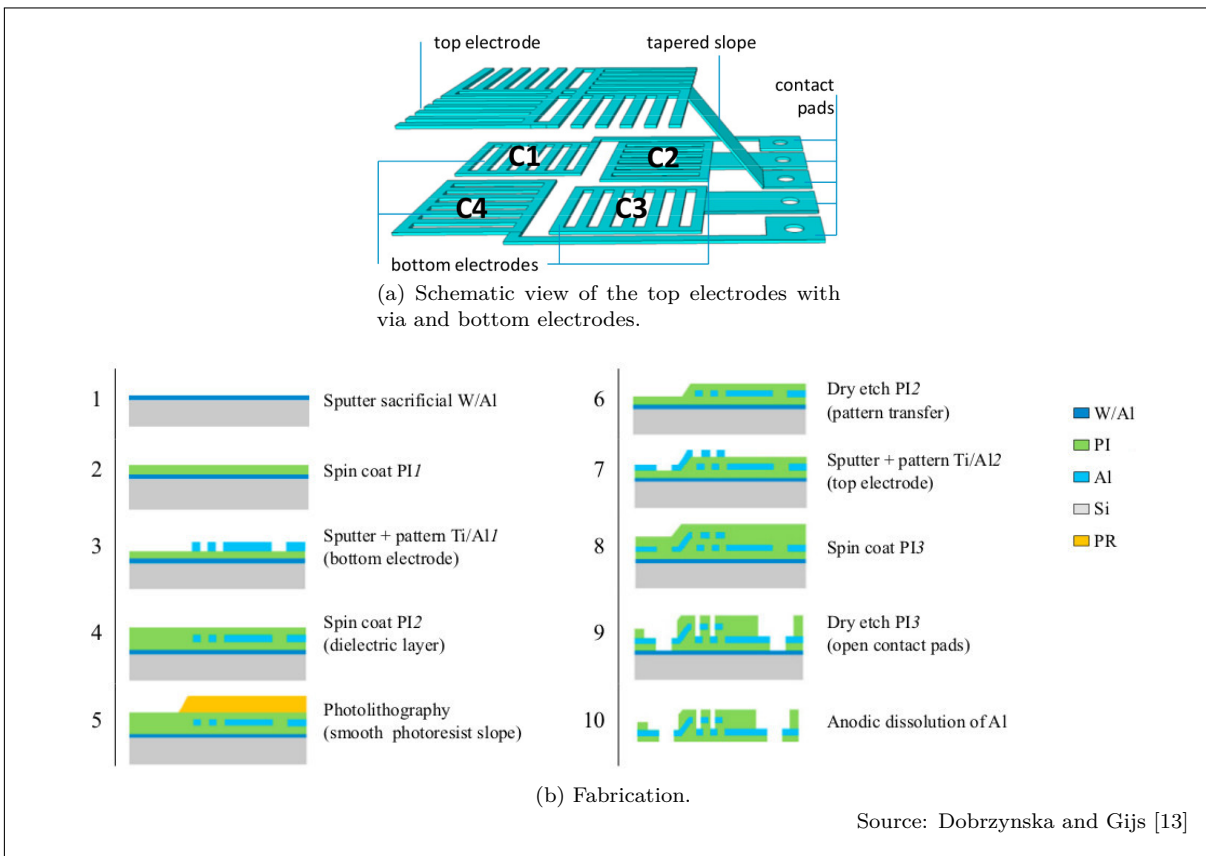


Figure 1.12: Capacitive flexible force sensor from Dobrzynska and Gijs.

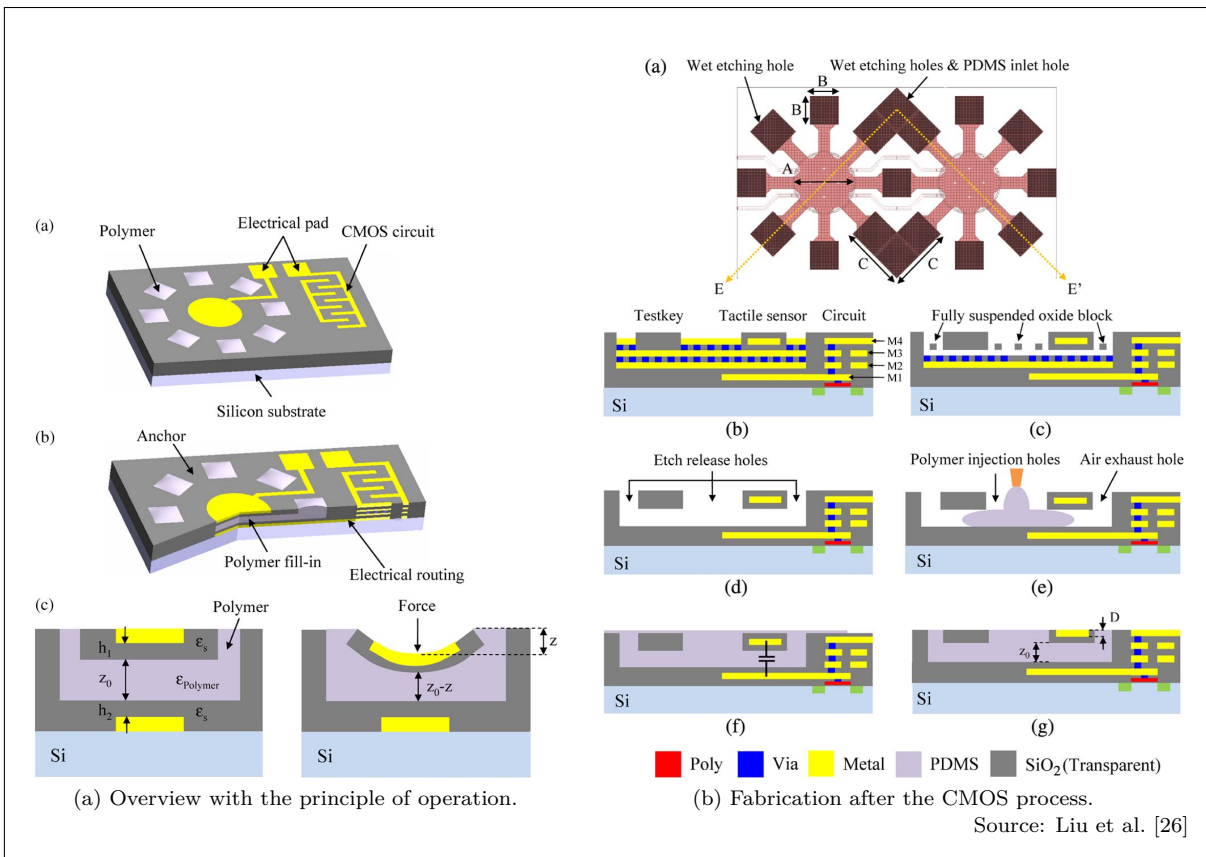


Figure 1.13: Development of a CMOS-Based Capacitive Tactile Sensor With Adjustable Sensing Range and Sensitivity Using Polymer Fill-In from Liu et al.

## 1.4 Piezoresistive force sensors with silicon springs

Another common way for readout of force sensors is using piezoresistive elements. These elements change in resistivity dependent of the applied stress. The design of these sensors are quite different than capacitive sensors, for the elements itself must be deformed.

In 2005, Beccai et al. came with a three-axial force sensor made in silicon and uses piezoresistive elements for measurements. It was developed for biomechanical measurements for prosthetics. The sensing chip consists of a stylus mounted on a plus-shaped spring allowing the three translations. There is a carrier chip that is connected by flip-chip bonding on the sensing chip. This method allows a thin sensor which makes it suitable for flexible skin implementation in prosthetics. The mechanical structures in the sensing chip was made using Advanced Silicon Etching, a deep dry etching process, in a SOI wafer. The p-type piezoresistors were obtained by ion implantation of boron. The sensor can manage forces until 2 N in all directions with high linearity (better than 99%).

The plus-shaped springs are quite common for silicon-based piezoresistive force sensors, but the fabrication can be completely different. Wisitsoraat et al., for example, made a sensor in 2007 described in their paper in reference [43] that can be made with low costs and uses surface micromachining. Fabrication is started by patterning a photoresist sacrificial layer on a glass substrate. The plus-shaped construction is deposited on and around the sacrificial layer. The structure is released by etching the photoresist. The sensor measures in the  $\mu\text{N}$  range with a sensitivity of  $0.2\text{ mV } \mu\text{N}^{-1}$ .

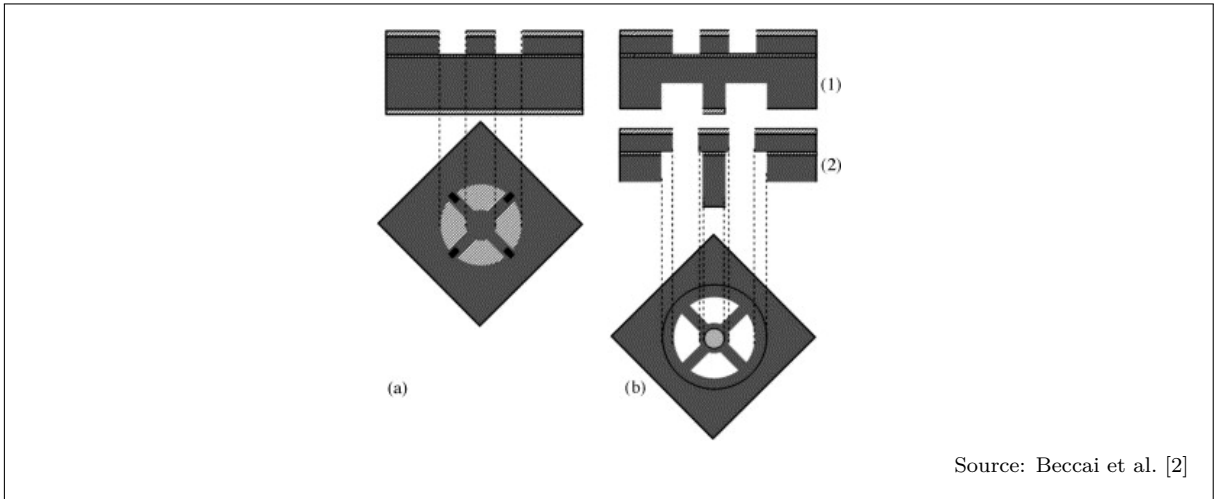


Figure 1.14: Design and fabrication of a hybrid silicon three-axial force sensor for biomechanical applications from Beccai et al.

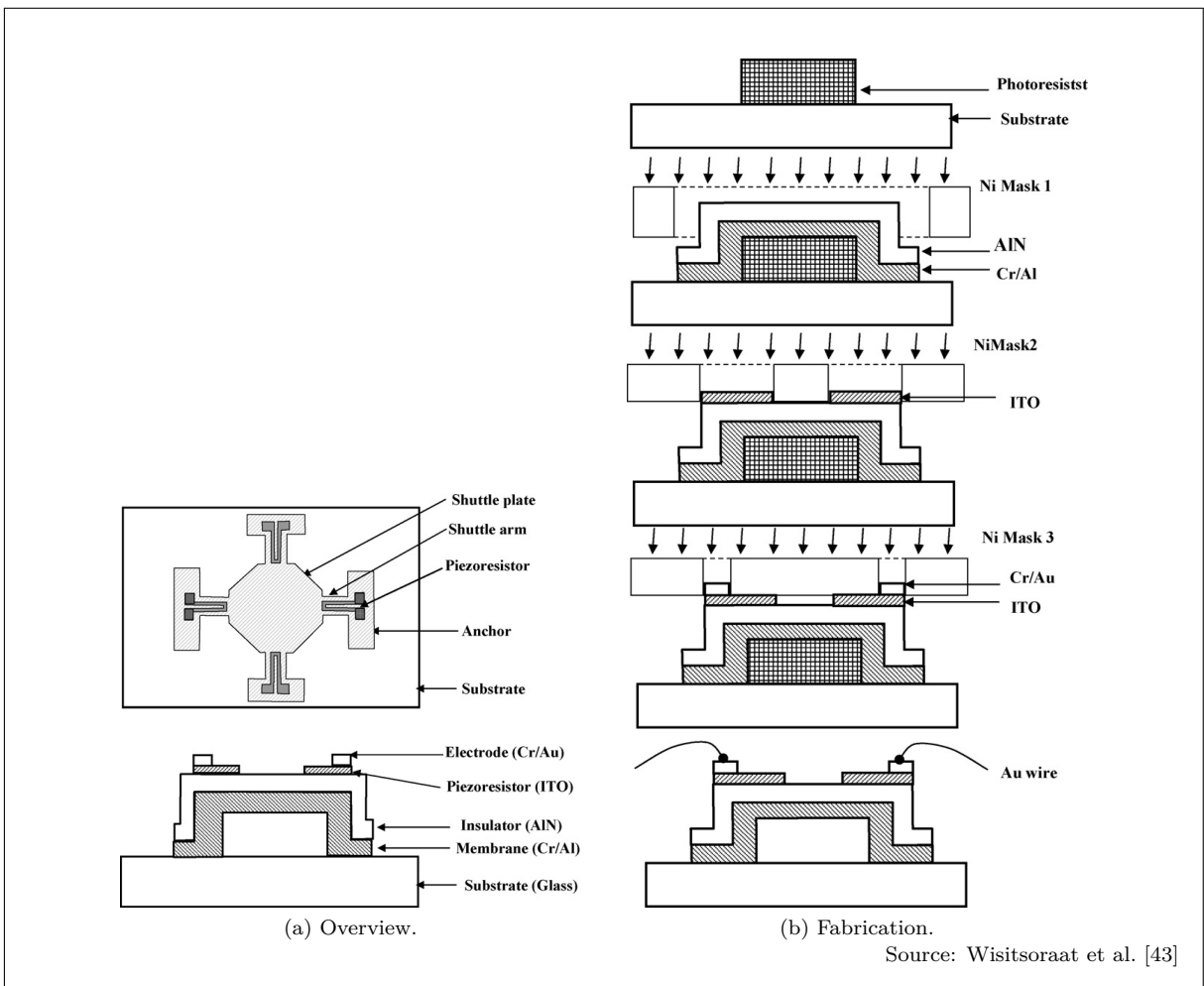


Figure 1.15: A Low cost thin film based piezoresistive MEMS tactile sensor from Wisitsoraat et al.

The sensor proposed in [38] by Tibrewala et al. in 2008 was made with bulk micromachining, like Beccai et al. did, but has a different and less complicated fabrication process. It also features experiments how the piezoresistors should be placed on the beams. It concludes that the T-form placement has the highest sensitivity in both directions. The sensor can handle a maximum force of 25 mN in all directions. Fabrication is done using an n-type wafer with a patterned layer of silicon dioxide. p-Diffusion is performed to form the strain gauges. KOH etching is used at the bottom of the wafer to form the plus-shaped spring.

The sensor in [40] by Wang et al. in 2009 is another plus-shaped sensor. Characteristic of the sensor is its application: it is designed for minimally invasive surgery. The sensor is tested until 1 mN and performed with a better resolution than 3  $\mu$ N.

Fabrication is described in detail in the paper. Bulk micromachining in a SOI wafer is used to form the plus-shaped structure. Boron implantation is done to make the piezoresistors. A pyrex glass wafer is anodic bonded to the SOI wafer and acts as overload protection.

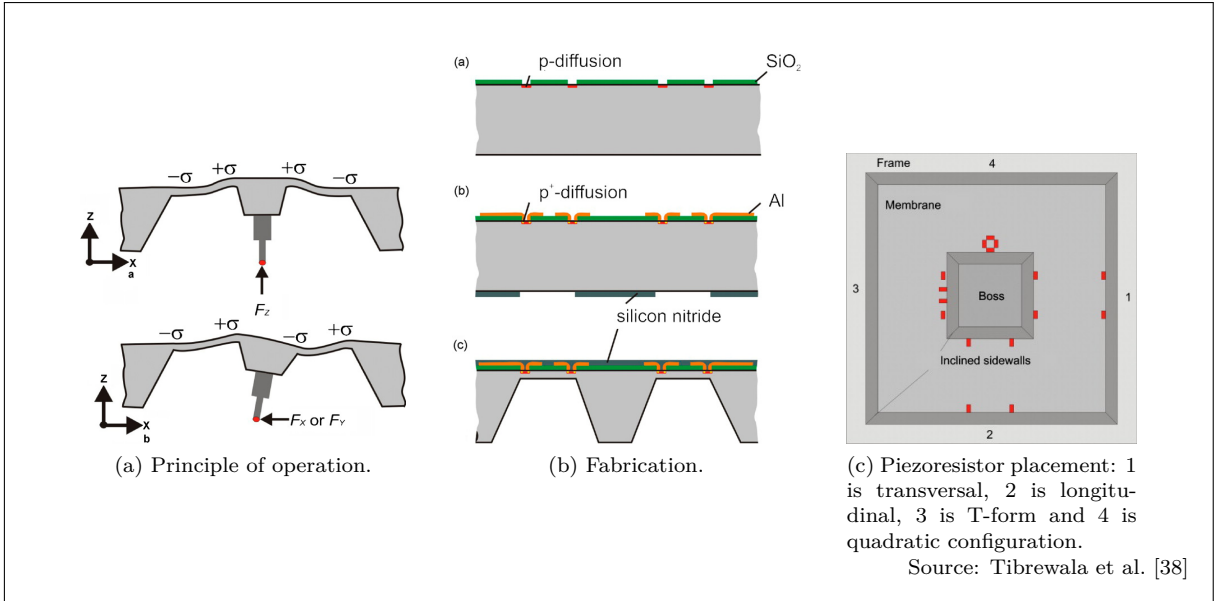


Figure 1.16: Simulation, fabrication and characterization of a 3D piezoresistive force sensor from Tibrewala et al.

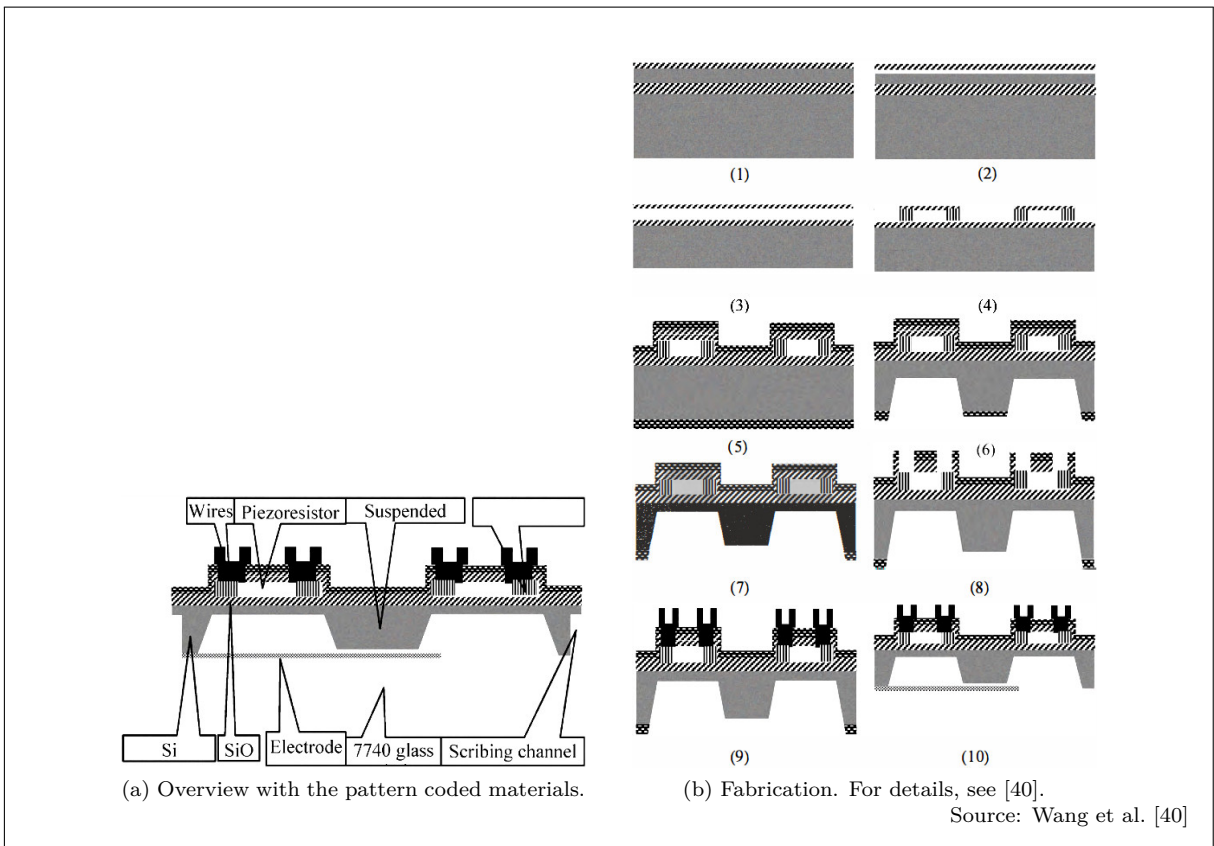


Figure 1.17: An integrated MEMS tactile tri-axial micro-force probe sensor for Minimally Invasive Surgery from Wang et al.

## 1.5 Piezoresistive force sensors with polymer springs

One can use polymer springs for force sensors instead of silicon springs in combination with piezoresistive elements, just as described previously with capacitive readout. But, because piezoresistive elements are flexible too, the complete sensors can be made flexible. Hwang et al. proposes a sensor [21] in 2007 that is completely flexible and is applicable in robotics. The sensor can handle 4 N of normal and shear force. Quantitative sensitivity information is not mentioned in the paper, but it is said that it is relatively low and the sensor is therefore inaccurate for small loads. Sensing is done with four strain gauges between a top layer of PDMS and a bottom layer of PI. Electrical connections on the top layer are connected to the strain gauges using vias.

A layer of PI is spin coated on a silicon wafer with a small layer of silicon dioxide. After patterning the gauges and electrical interconnections, the PI layer is released from the silicon wafer by etching out the silicon dioxide layer. The PI layer with strain gauges is attached on a ductile PDMS substrate using adhesive Kapton film.

A completely different way of using piezoresistive elements in a flexible material is done by Takei et al. Takei et al. present a sensor [36] in 2012 based on a flexible polymer layer for lingual motion sensing. The paper describes measurement results of shear stresses and pressures that occur in the mouth by humans swallowing water. The sensor should withstand therefore a shear stress of 2 kPa and a pressure of 20 kPa. The principle of operation is based on three piezoresistive cantilevers oriented in three directions immersed in PDMS. Two cantilevers are folded in vertical direction to measure the shear forces. The third cantilever is similar to a bending bridge and measures the normal force.

All cantilevers are made, following to [30] of the same research group, by etching in a SOI wafer and sputtering chrome and nickel layers. A magnetic field bends two of the cantilevers in vertical direction. After the fabrication of the actual sensor mechanisms, a PDMS layer is added.

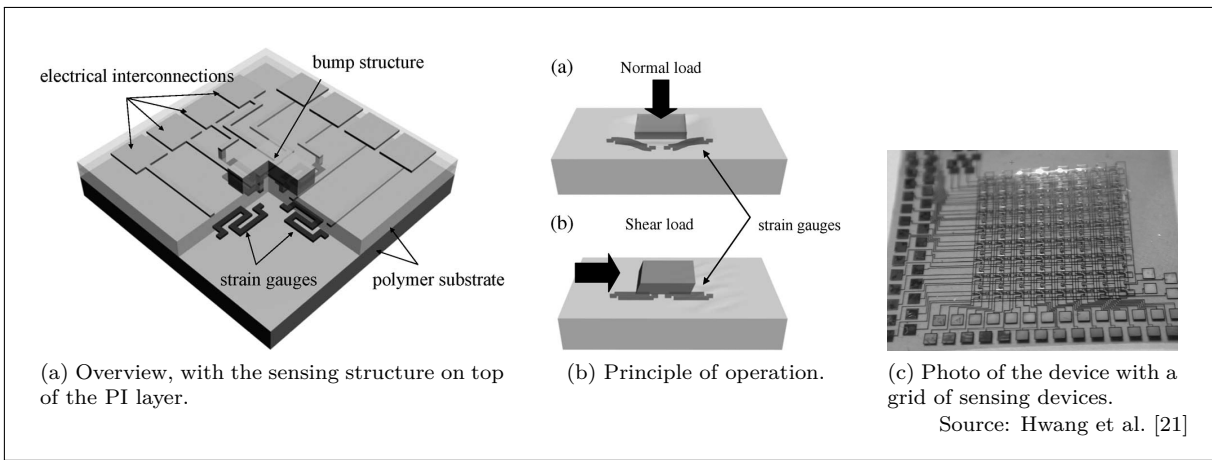


Figure 1.18: A polymer-based flexible tactile sensor for both normal and shear load detections and its application for robotics from Hwang et al.

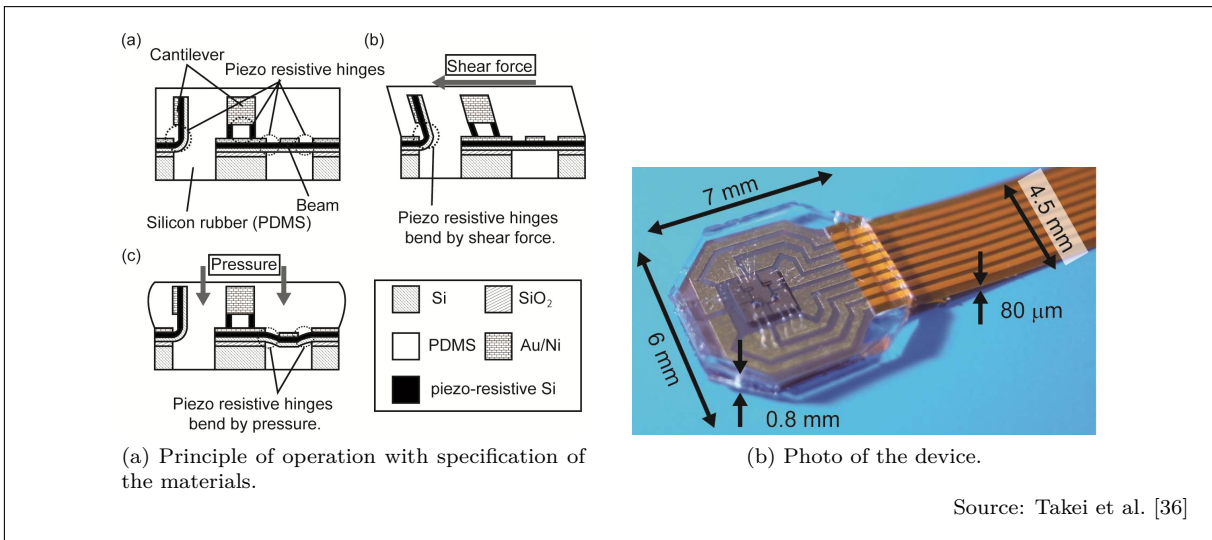


Figure 1.19: A triaxial force sensor for lingual motion sensing from Takei et al.

## 1.6 Conclusion

This part summarized the working principles, fabrication and performance of 15 sensors. All sensors are categorized in four categories: capacitive force sensors with silicon springs, capacitive force sensors with polymer springs, piezoresistive force sensors with silicon springs and piezoresistive force sensors with polymer springs.

All sensors met the requirements for this literature study: all sensors can be fabricated with the technology that exists in the MESA+ nanolab of the University of Twente and all sensors have at least one characteristic property for tactile sensing.

The sensors are summarized in table 1.2.

Table 1.2: Overview of the force sensors described in this part.

Author	Year	DOF <sup>a</sup>	Spring material	Output <sup>b</sup>	Range <sup>c</sup>	Performance <sup>cd</sup>
Brookhuis et al.	2012	6	Silicon	Capacitive	10 N	16 pF N <sup>-1</sup>
Beyeler et al.	2009	6	Silicon	Capacitive	1 mN	1 μN
Muhammad et al.	2011	1	Silicon	Capacitive	24 mN	N/A <sup>g</sup>
Chu et al.	2007	1	Silicon	Capacitive	11 μN	18 fF mN <sup>-1</sup>
Lee et al.	2008	3	PDMS	Capacitive	10 mN	2.5 % mN <sup>-1</sup>
Dobrzynska and Gijs	2010	1	PI	Capacitive	3 kN	1 fF N <sup>-1</sup>
Liu et al.	2011	1	PDMS	Capacitive <sup>e</sup>	2.4 mN	1.5 mV mN <sup>-1</sup>
Chase and Luo	1995	1	N/A <sup>g</sup>	Capacitive	N/A <sup>g</sup>	N/A <sup>g</sup>
Beccai et al.	2005	3	Silicon	Piezoresistive	2 mN	<1 %
Tibrewala et al.	2008	3	Silicon	Piezoresistive	25 mN	N/A <sup>g</sup>
Wang et al.	2009	3	Silicon	Piezoresistive	1 mN	3 μN
Wisitsoraat et al.	2007	3	AlN Cr/Al	Piezoresistive	1 μN	0.2 mV μN <sup>-1</sup>
Takei et al.	2012	3	PDMS	Piezoresistive	2 kPa	N/A <sup>g</sup>
Hwang et al.	2007	3	PDMS	Piezoresistive	4 N	N/A <sup>g</sup>

<sup>a</sup> Degrees of freedom.

<sup>b</sup> Quantity that is measured at the output of the sensor.

<sup>c</sup> For 6DOF and 3DOF sensors in shear direction, for 1DOF sensors the supported direction.

<sup>d</sup> Can be the sensitivity (in F N<sup>-1</sup> for example), resolution (in N for example) or error (in % for example).

<sup>e</sup> With on-chip readout electronics.

<sup>f</sup> This is not a typographical error, the elastic material silicone is meant here.

<sup>g</sup> Not available or not applicable.

Silicon based capacitive force sensors combine classical fabrication techniques with freedom in design. The sensing structures only need two capacitor plates which can be placed and oriented in several ways (e.g. parallel plates or combs). This literature study proves the very different possibilities for this category of sensors.

Capacitive sensors with polymer springs may allow even more freedom in design, since the capacitor plates are not forced to be supported by silicon structures but may be floating in a thick polymer layer. However, using polymers in sensors requires less trivial fabrication steps.

The freedom in design for piezoresistive silicon based force sensors is more limited. This literature study shows that most designers choose for a plus-shaped sensor with piezoresistive elements attached to the beams. The fabrication of piezoresistive force sensors is also not very diverse: the sensing structures are mostly made using surface micromachining (p-diffusion) and the mechanical structures is mostly made using a back etch in the wafer.

Using a polymer as spring material for piezoresistive sensors gives designers more freedom. A thick polymer layer submerges the sensing elements, making it possible to place and orientate the sensing structures in every arbitrary way. But as it applies to all polymer sensors, the fabrication is not yet as trivial as the well-known silicon technology.

$$\frac{d^2}{dx^2} \left( EI \frac{d^2 u}{dx^2} \right) = q$$
$$\nabla \cdot \vec{E} = \frac{\rho}{\epsilon}$$

## 2.1 Introduction

This part describes the full design flow for a capacitive force/torque sensor. Capacitive force/torque sensors use a spring mechanism to convert forces (or torques) in displacements. These displacements cause capacitor plates change in gap or change in overlapping area. The change in capacitance can be measured electrically.

Five requirements, which are derived from the requirements in the overall introduction, are taken as guideline through the design process:

- the sensor should be relatively trivial to fabricate using well-known technologies and the technology should be highly reproducible, i.e. the fabrication should take less than two months;
- the sensor should support measurements in multiple degrees of freedom;
- the sensor should have a competing sensitivity, in comparison with with the sensors summarized in the literature study;
- the sensor should be able to handle human forces, e.g. multiple newtons;
- the sensor should be small, preferable less than  $1\text{ cm}^2$  with a thickness of less than 1 mm.

It is not possible to make above requirements more specific (e.g. give quantitative values to the sensitivity or force range), since some requirements may interfere with other requirements.

The design is roughly divided in two parts: the spring mechanism and the sensing structures. It starts with a brief overview of three concepts for the spring mechanism. The advantages and disadvantages of the concepts are compared. Then, several possible sensing structures are proposed for the chosen spring mechanism. This part continues with the derivation of a mathematical model of the whole sensor. After this, simulations and the details of the design are described.

## 2.2 Concepts for a six degrees of freedom stage

Most force sensors are based on measuring a displacement rather than the force directly. A system of springs convert the force to a displacement. This section describes multiple spring systems with their stiffness in shear and normal direction obtained by finite element method (FEM) simulations. Besides, the maximum stress of all concepts is determined. The concepts are briefly described; more detailed descriptions of the models and simulations are in section 2.5.

The simulations were done using COMSOL Multiphysics 4.3.0.151.

### 2.2.1 Bottom supported springs of SU-8

This concept is based on the negative photoresist SU-8 as spring material. Typical of SU-8 is that it can be patterned with very high aspect ratios. It's Young's modulus is 4.02 GPa and it's maximum stress (after a hard bake) is 34 MPa [12]. The latter property must be interpreted as a guideline, as the material will fail with a different stress in different directions.

#### Stiffness

A model of a six degrees of freedom stage is made in COMSOL (figure 2.5). A cylinder of polysilicon with a diameter of 1 cm and thickness of 500  $\mu\text{m}$  is used as stage. Several small pillars of SU-8 support the stage at the bottom. The number of pillars and the diameter of the pillars is swept and the stiffness and maximum stress is investigated. A diameter of 300  $\mu\text{m}$  and a length of 300  $\mu\text{m}$  for the pillars that are located in a grid with a distance of 1250  $\mu\text{m}$  from each other turned out to have the optimal behavior. A stress of 12 MPa at maximum for 10 N of shear load with a stiffness of 12  $\text{N } \mu\text{m}^{-1}$  is obtained. For a normal load of 10 N, a stress of 3.6 MPa at maximum with a stiffness of 50  $\text{N } \mu\text{m}^{-1}$  is obtained.

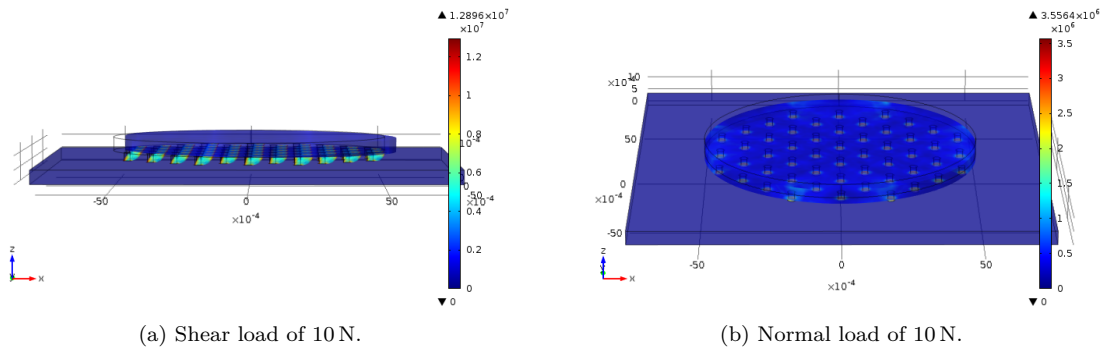


Figure 2.1: FEM simulation of the bottom supported springs of SU-8 concept. The colors represent the von Mises stress in Pa.

#### Fabrication

Since SU-8 is a photoresist that can be patterned with very high aspect ratios, many mechanical structures are possible, e.g. mechanical application can be achieved like was done in reference [6]. However, a rigid stage is needed as end-effector of the sensor and must be bonded on top of the pillars. Two methods were reviewed for bonding a rigid stage to SU-8 pillars.

##### *SU-8 bonding*

SU-8 is an epoxy based material that may be bonded to another SU-8 layer under pressure and with the right temperature. Pan et al. did this for SU-8 layers of 100  $\mu\text{m}$  [32]. A bonding strength of 20.6  $\mu\text{m}$  was measured in the publication. However, the bonding process with SU-8 is still not trivial microfabrication and may require many experiments before it can be used in the design of a force/torque sensor.

##### *Through-hole mounting*

By supporting the SU-8 pillars inside holes in the stage, a strong bond will be made. Figure 2.2 describes schematically how this could be done. Holes will be etched in a silicon wafer. Another etch forms small bumps at both sides of each chip. The etched wafer will be bonded on another wafer. The structure

will be filled with SU-8 and exposed through the holes of the top wafer. After development and rinsing, pillars of SU-8 are made between the two wafers.

It must be noticed that SU-8 has a high viscosity; it may be difficult to rinse away all the undeveloped SU-8.

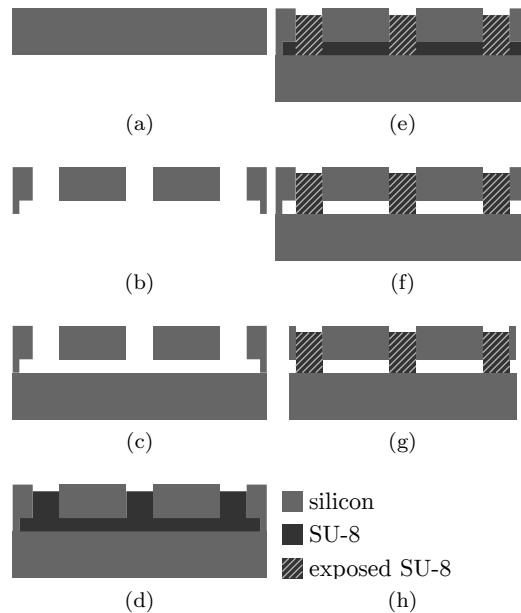


Figure 2.2: SU-8 pillars in holes: (a) a silicon wafer, (b) etching holes in the wafer with small bumps at both sides of the chip, (c) bond the wafer on top of another silicon wafer, (d) fill the structure with SU-8, (e) expose SU-8 through the holes of the top wafer, (f) develop and rinse, (g) saw or etch the wafer in chips.

### Capacitor integration

Capacitors may be made between the top and bottom layer. Patterning of SU-8 allows the capacitor structures be very close to each other, which increases sensitivity.

### 2.2.2 Bottom supported springs of PDMS

Instead of SU-8 as spring material, another polymer can be used. Polydimethylsiloxane (PDMS) is a polymer with a very low Young's modulus (750 kPa [27]) compared to other polymers. Its stress/strain relation is linear until a stress of approximately 300 kPa [41].

#### Stiffness

In COMSOL, a stage of polysilicon with a diameter of 1.5 cm and thickness of 400  $\mu\text{m}$  is modelled. A layer of PDMS acts as support and is directly mounted at the bottom of the stage. The PDMS layer has a thickness of 30  $\mu\text{m}$ . The model turns out to have a stress of 238 kPa at maximum for 10 N of shear load with a stiffness of 1.5  $\text{N } \mu\text{m}^{-1}$ . For a normal load of 10 N, a stress of 58 kPa at maximum with a stiffness of 77  $\text{N } \mu\text{m}^{-1}$  is obtained.

#### Fabrication

One solid layer of PDMS can be used as spring system, as is done in the simulation. But to achieve a sufficient capacitance over stiffness ratio, the layer of PDMS should be less stiff and the electrodes should be closer to each other. Patterning PDMS can reduce the stiffness in all directions and allows close capacitor structures. For example, PDMS pillars can be made with capacitor electrodes between the pillars. Unfortunately, patterning PDMS is not as trivial as patterning a photoresist like SU-8.

### Capacitor integration

Capacitors may be realized inside the flexible layer or at the top and bottom layer. Achieving high sensitivity will be difficult, since this requires the capacitor electrodes to be close to each other.

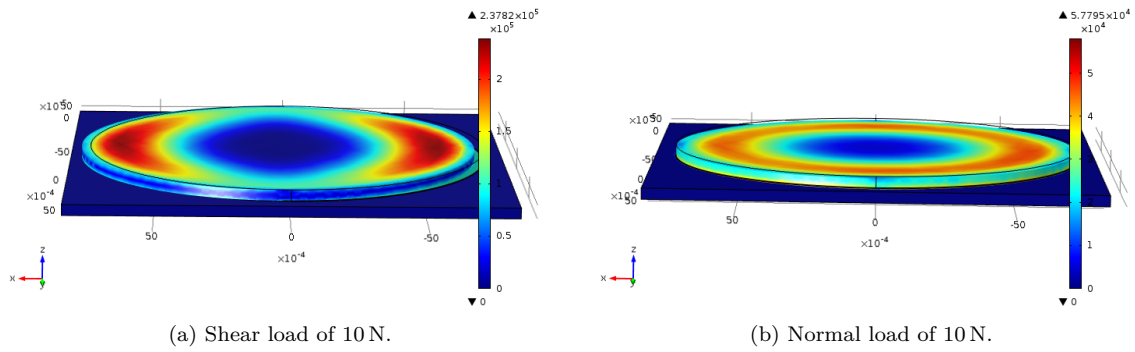


Figure 2.3: FEM simulation of the bottom supported springs of PDMS concept. The colors represent the von Mises stress in Pa.

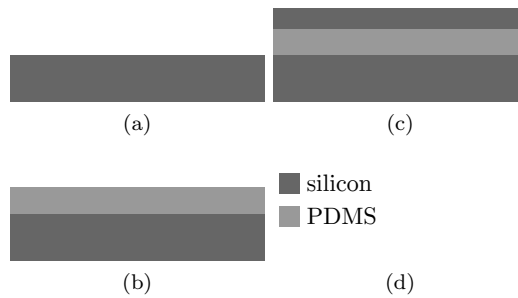


Figure 2.4: PDMS sensor fabrication: (a) a silicon wafer (b) application of one solid layer of PDMS (c) bonding or growing another layer of silicon

### 2.2.3 Edge supported springs of silicon

Previous two concepts are bottom supported. A six degrees of freedom stage can be also supported at the edges. As silicon is the most trivial material for microfabrication, this material is taken as starting point. A circular six degrees of freedom stage needs a point symmetric system of springs which are compliant in two directions. The v-shaped spring is the simplest implementation that obeys above specifications.

#### Stiffness

A stage of polysilicon with a diameter of 2.5 mm and thickness of 380  $\mu\text{m}$  is modelled as end-effector. The stage is supported by 15 v-shaped springs consisting of two right-angled flexures of 490  $\mu\text{m}$  per flexure. A stress of 448 MPa at maximum with a stiffness of 8.3 N  $\mu\text{m}^{-1}$  was found for 10 N of shear load. For a normal load of 10 N, a stress of 363 kPa at maximum with a stiffness of 7.6 N  $\mu\text{m}^{-1}$  was found.

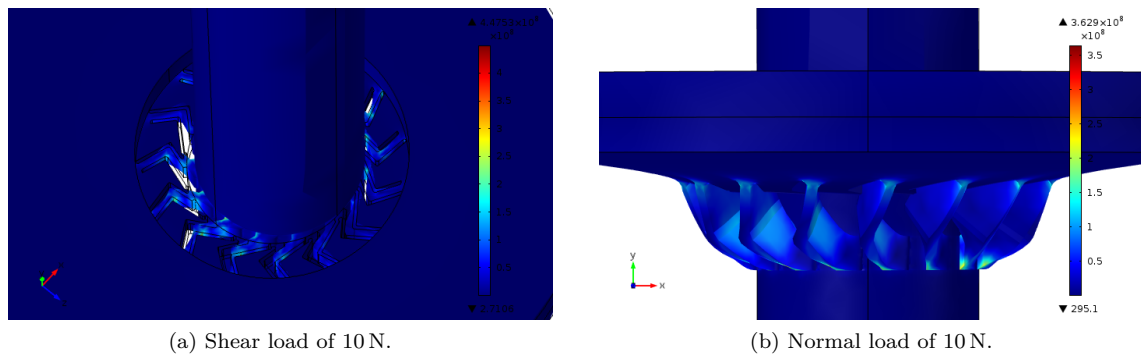


Figure 2.5: FEM simulation of the edge supported springs of silicon concept. The colors represent the von Mises stress in Pa.

## Fabrication

The fabrication of this concept should be quite straight-forward. The stage can be made by through-wafer etching. This should be very anisotropic, deep reactive ion etching is a common method to achieve deep anisotropic etches. The sensing structures can be made in another wafer which can be bonded to the stage wafer. Also silicon-on-insulator wafers may be used. These wafers have three layers: one thick layer of silicon, one very thin isolation layer of silicon dioxide and one thin layer of silicon.

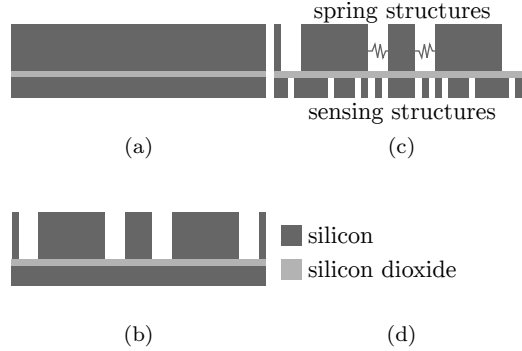


Figure 2.6: Edge supported sensor fabrication: (a) a silicon-on-insulator wafer (b) etch of the springs in the upper layer (c) etch of the sensing structures in the device layer

## Capacitor integration

Capacitors can be simply made in the bottom layer of silicon. Comb-structures are possible for example.

### 2.2.4 Concept comparison

Table 2.1 compares the three proposed concepts. The simulated stiffnesses in shear and normal direction are summarized. The capacitor integration gives a qualitative impression of how capacitor structures may perform in the design. Trivial microfabrication gives a qualitative impression of how many fabrication steps are needed and if there is much documentation available.

Table 2.1: Comparison of the proposed concepts

	Shear stiffness	Normal stiffness	Capacitor integration	Trivial fabrication
Pillars of SU-8	$12 \text{ N } \mu\text{m}^{-1}$	$50 \text{ N } \mu\text{m}^{-1}$	0	–
Solid PDMS	$1.5 \text{ N } \mu\text{m}^{-1}$	$77 \text{ N } \mu\text{m}^{-1}$	–	0
Edge-supported silicon	$8.3 \text{ N } \mu\text{m}^{-1}$	$7.6 \text{ N } \mu\text{m}^{-1}$	+	+

A stage with SU-8 pillars may perform very well: the low stiffness in combination with mechanical amplification results in high sensitivity. A disadvantage of this concept is the non-trivial fabrication, since bonding a rigid stage on top of SU-8 pillars may require a lot of preliminary experiments.

A stage supported by a solid layer of PDMS is very compliant in shear direction and stiff in normal direction. The stiffness in normal direction can be decreased, but results in a larger distance between the capacitor electrodes. Obtaining a good stiffness/capacitance ratio can be done by using pillars or rings, but this makes the fabrication more difficult.

A silicon edge-supported stage can be tuned to have equal stiffness in all directions and allows multiple kinds of capacitor integration. It uses fabrication methods that are well-known by MESA+.

Since the latter concept has no expected inconveniences and it has the possibility to achieve high sensitivities, this concept is chosen.

## 2.3 Concepts for sensing structures

Two shear forces, one normal force and three torques should be measured with the sensor. Hence, sensing structures should be able to measure displacements in the corresponding directions and rotations.

Comb-structures are very common MEMS structures to achieve large capacitances. Comb-structures can be used to measure shear displacements: one can attach the structures directly to the six degrees of freedom stage like is illustrated in figures 2.7a and 2.7b. Mechanical spring and lever systems can be implemented to support the comb-structures and discriminate the force components, examples of these are illustrated in figures 2.7c and 2.7d. Also mechanical amplification is possible, 2.7e shows how this can be implemented. Most examples are designed for measuring shear forces and torques around the normal axis. 2.7e is also able to measure normal force and the torques around the shear axes, as can be seen in figure 2.8b.

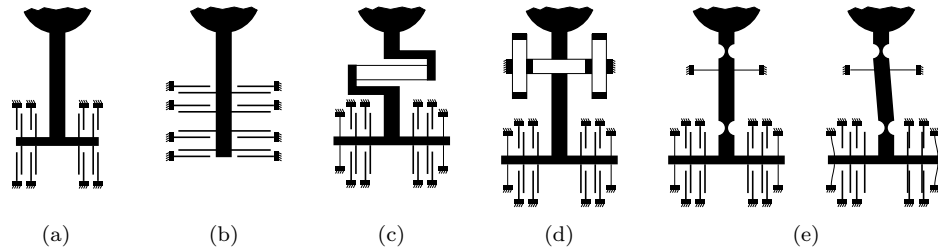


Figure 2.7: Sensing structures for shear forces and torques around the normal axis.

Normal forces and the torques around the shear axes can also be measured using parallel plates with the handle layer, like is illustrated in figure 2.8a.

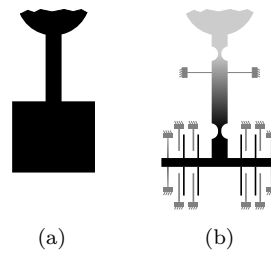


Figure 2.8: Sensing structures for normal forces and the torques around the shear axes.

The sensing structures should be robust and its behavior should be completely known in the design phase. The design in figure 2.7c is therefore chosen as sensing structure for shear displacements; the structure is supported may be supported at multiple places and its behavior is easy to model. The simple parallel plate structure in 2.8a is chosen for sensing normal displacements. It has less complicated joints and levers compared with 2.8b.

## 2.4 Mathematical model

In this section, a model for the chosen concept is derived using fundamental physics. But first, the principle of operation using the chosen concepts of sections 2.2 and 2.3 will be summarized.

### 2.4.1 Principle of operation

The sensor consists of a suspended core which is fabricated in the handle layer of an SOI wafer. The suspended core is supported by v-shaped silicon springs. An applied load to the suspended core will result in a displacement. In-plane displacement caused by a shear force is measured by comb-structures present in the device layer and results in a differential change in gap between the comb-fingers (figure 2.9).

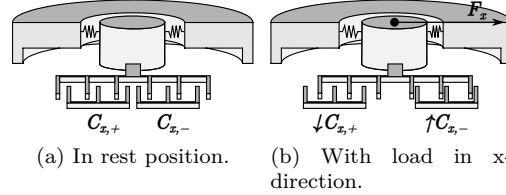


Figure 2.9: Principle of operation for shear forces.

A normal force results in an out-of-plane displacement, which is measured by parallel plate electrodes (figure 2.10b). By differential measurement of two opposite electrodes (figure 2.10c), the applied torque is determined.

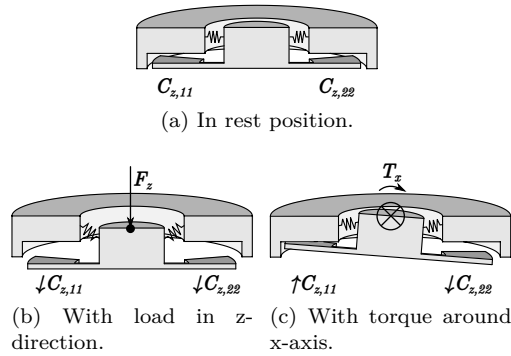


Figure 2.10: Principle of operation for normal forces and torques.

### 2.4.2 Mathematical model of the mechanics of the stage

All spring systems that are going to be used in the design of the sensor are bending beams. The Euler-Bernoulli beam theory is a cornerstone of mechanical engineering in the past century and covers the behavior of deflecting beams due to lateral loads.

#### Euler-Bernoulli beam theory

The Euler-Bernoulli beam equation describes the relationship between deflection and load [18]:

$$\frac{d^2}{dx^2} \left( EI \frac{d^2 u}{dx^2} \right) = q, \quad (2.1)$$

with  $E$  Young's modulus,  $I$  the second moment of area,  $u$  the deflection,  $x$  the horizontal coordinate of a point at the beam and  $q$  the distributed load (as force per unit of length).

Young's modulus  $E$  and the second moment of area  $I$  may be assumed constant; equation 2.1 becomes:

$$EI \frac{d^4 u}{dx^4} = q \quad (2.2)$$

The force is at the end  $L$  of the beam in one point. This can be defined by a Dirac delta function  $\delta(x - L)$ .

$$EI \frac{d^4 u}{dx^4} = F\delta(x - L) \quad (2.3)$$

Integration at both sides of the equation leads to a force at  $x = L$  in the right-hand side.

$$EI \frac{d^3 u}{dx^3} = \int F\delta(x - L) dx = F(L) + c_1 = F(L) \quad (2.4)$$

It appears that the left-hand side of the equation is equal to the shear force.  $c_1$  will conflict when it is non-zero. A second integration leads to the bending moment.

$$EI \frac{d^2 u}{dx^2} = F(L)x + c_2 \quad (2.5)$$

And the third integration leads to the bending speed.

$$EI \frac{du}{dx} = \frac{1}{2}F(L)x^2 + c_2x + c_3 \quad (2.6)$$

The fourth integration leads to an equation with the actual deflection.

$$EIu = \frac{1}{6}F(L)x^3 + \frac{1}{2}c_2x^2 + c_3x + c_4 \quad (2.7)$$

The integration constants  $c_2$ ,  $c_3$  and  $c_4$  vary for different boundary settings and can be found using equations 2.5, 2.6 and 2.7. Substituting the integration constants in 2.7 leads to a the right beam model.

Two beam models are derived: a beam with a guided end and a beam with a free end.

### Boundary conditions for a beam with a guided end

A guided beam is fixed at one end and is guided at the other end. A point force is applied at the guided end. Figure 2.11 shows a guided beam with the dimensions.

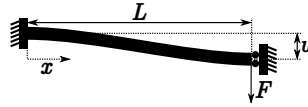


Figure 2.11: Guided beam with dimensions.

The beam is fixed at  $x = 0$ .

$$u|_{x=0} = 0 \rightarrow c_4 = 0 \quad (2.8)$$

$$\left. \frac{du}{dx} \right|_{x=0} = 0 \rightarrow c_3 = 0 \quad (2.9)$$

Half of the total bending moment is at  $x = L$ , this models the guided end of the beam.

$$M = -EI \left. \frac{d^2 u}{dx^2} \right|_{x=L} = \frac{1}{2}F(L)L \rightarrow c_2 = -\frac{1}{2}F(L)L \quad (2.10)$$

Substituting the boundary conditions leads to the following equation.

$$EIu = \frac{1}{6}F(L)x^3 - \frac{1}{4}F(L)Lx^2 \quad (2.11)$$

Rewriting the equation results in a model for a guided beam.

$$u = -\frac{F(L)x^2}{12EI}(3L - 2x) \quad (2.12)$$

The result corresponds with [31]. The deflection at the end of the beam ( $x = L$ ) is:

$$u = -\frac{FL^3}{12EI}. \quad (2.13)$$



Figure 2.12: Beam with free end with the dimensions.

### Boundary conditions for a beam with a free end

A beam with a free end is fixed at one end and is free at the other end. A point force is applied at the free end. Figure 2.12 shows a beam with a free end with the dimensions.

The beam is fixed at  $x = 0$ .

$$u|_{x=0} = 0 \rightarrow c_4 = 0 \quad (2.14)$$

$$\left. \frac{du}{dx} \right|_{x=0} = 0 \rightarrow c_3 = 0 \quad (2.15)$$

The total bending moment is at  $x = 0$ , since this is the only location where it has constraints.

$$M = -EI \left. \frac{d^2u}{dx^2} \right|_{x=0} = F(L)L \rightarrow c_2 = -F(L)L \quad (2.16)$$

Substituting the boundary conditions leads to the following equation.

$$EIu = \frac{1}{6}F(L)x^3 - \frac{1}{2}F(L)Lx^2 \quad (2.17)$$

Rewriting the equation results in a model for a guided beam.

$$u = -\frac{F(L)x^2}{6EI}(3L - x) \quad (2.18)$$

The result corresponds with [31]. The deflection at the end of the beam ( $x = L$ ) is:

$$u = -\frac{FL^3}{3EI}. \quad (2.19)$$

### Stiffness of the suspended core

The chosen edge-supported stage uses v-shaped springs. Ideal springs obey Hooke's law.

$$F = k \cdot u, \quad (2.20)$$

$$T = c \cdot \phi, \quad (2.21)$$

with  $F$  the force,  $u$  the displacement and  $k$  the stiffness,  $T$  the torque,  $c$  the rotational stiffness and  $\phi$  the angle. The system of springs is dimensioned for forces in the first place, therefore, it is necessary to know the stiffness in each direction. The chosen concept uses the point symmetric v-shaped spring system shown in figure 2.13.

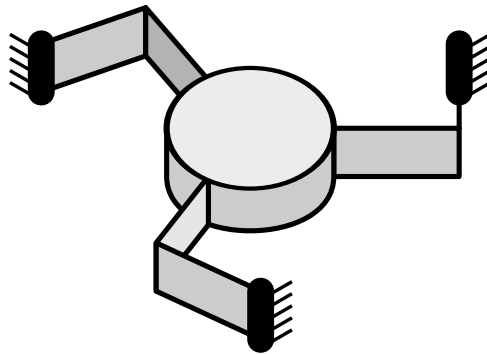


Figure 2.13: A six degrees of freedom stage using folded sheet springs. The combination of three folded sheet springs is called a spring triplet.

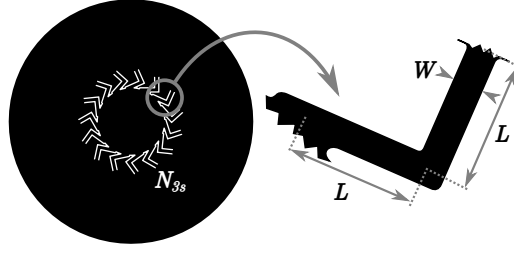


Figure 2.14: Handle layer with the point symmetric v-shaped spring system and the parameters of each spring.

However, the spring system is applied multiple times to achieve higher stiffnesses in all directions. Figure 2.14 shows the dimensions of the suspended core.

The stiffness in normal direction of a guided beam, consisting of two serial beams with length  $L$ , is:

$$k_z = \frac{F}{u_z} = \frac{12EI}{(2L)^3}. \quad (2.22)$$

As long as the suspended core is supported by flexures located in a point symmetrically way around the core, the stiffness of the is equal to  $N$  times  $k_z$ . Since the suspended core is supported by multiples of three flexures,  $N_{3s} = 3N$  is the number of flexure triplets and is substituted in equation 2.23.

$$k_{stage,z} = \frac{F}{u_z} = \frac{36N_{3s}EI}{8L^3} \quad (2.23)$$

The stiffness matrix in both shear directions and the torsional stiffness can be obtained by using the free end beam theory in the way it was done in reference [34].

$$K_{xy\phi} = \begin{bmatrix} \frac{15EI}{2L^3} & -\frac{9EI}{2L^3} & -\frac{9EI}{2L^3} \\ -\frac{9EI}{2L^3} & \frac{15EI}{2L^3} & \frac{3EI}{2L^3} \\ -\frac{9EI}{2L^3} & \frac{3EI}{2L^3} & \frac{7EI}{2L^3} \end{bmatrix} \quad (2.24)$$

To obtain the stiffness in shear direction of the suspended core consisting of folded sheet flexures located point symmetrically, a displacement vector is defined in shear direction.

$$\vec{u} = [1 \quad 0 \quad 0] \quad (2.25)$$

This vector can be rotated  $\phi$  degrees with rotation matrix  $H_{rot}(\phi)$ .

$$H_{rot}(\phi) = \begin{bmatrix} \cos(\phi) & -\sin(\phi) & 0 \\ \sin(\phi) & \cos(\phi) & 0 \\ 0 & 0 & 1 \end{bmatrix} \quad (2.26)$$

If there are three flexures, all  $120^\circ$  rotated with respect to each other, the stiffness in shear direction can be calculated by rotating the shear force vector  $0^\circ$ ,  $120^\circ$  and  $240^\circ$  and multiply each rotated vector with the stiffness matrix. Multiplying with the inverse of each rotated vector and calculating the sum of these result in the stiffness in shear direction. Summarized:

$$k_x = \sum_{i=0}^2 \vec{u} H_{rot} \left( \frac{2}{3}\pi i \right) k \cdot \vec{u}^{-1} = \frac{45EI}{2L^3}. \quad (2.27)$$

This corresponds to reference [34]. As long as the suspended core is supported by a point symmetric spring setup, the stiffness is equal in all shear directions. Equation 2.27 can be extended with supported for multiple flexure triplets  $N_{3s}$ .

$$k_{stage,x} = \frac{45N_{3s}EI}{2L^3} \quad (2.28)$$

The second moments of area are as follows.

$$I_x = \frac{TW^3}{12}, \quad (2.29)$$

$$I_z = \frac{WT^3}{12}, \quad (2.30)$$

with  $T$  the thickness of the beam (equal to the thickness of the handle layer) and  $W$  the width of the beam.

The six degrees of freedom mesa can be tuned for translations with parameters  $L$ ,  $W$  and  $N_{3s}$  by substituting the equations of 2.31 in equations 2.28 and 2.23:

$$k_x \propto \frac{N_{3s}}{L^3} W^3, \quad (2.31)$$

$$k_z \propto \frac{N_{3s}}{L^3} W. \quad (2.32)$$

The stiffness in x-direction compared to z-direction can be optimized by choosing the right value for the flexure width  $W$ , the stiffness in both directions can be tuned by the flexure part length  $L$ . When stiff structures are desired, the flexure part length  $L$  may be very small compared to the flexure width  $W$ . This may jeopardize the validity of mentioned model. Adding multiple spring triplets  $N_{3s}$  allows the flexure part length  $L$  to be larger. This results in an overconstrained construction, but it is not expected that this will introduce problems since the whole structure will be of a monolithic material.

### 2.4.3 Mathematical model of the electrostatics of the sensing structures

The sensor uses capacitive sensing structures. Figure 2.15 shows where the chosen capacitor structures are located.

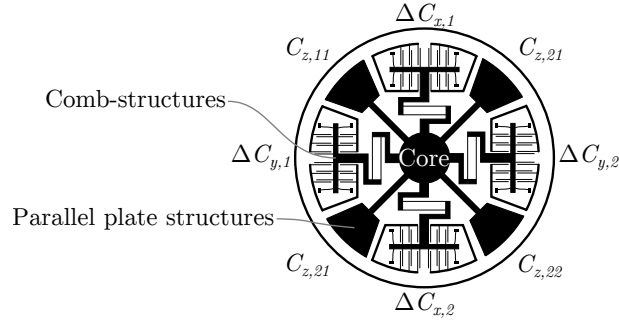


Figure 2.15: Design of the device layer with declaration of all sensing capacitors.

There are large parallel electrode capacitors for normal force and torque measurements and comb-structures for shear force measurements. Both capacitor structures can be modeled as gap closing parallel plate capacitors [14].

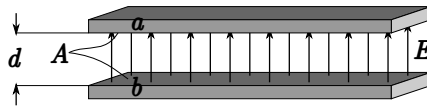


Figure 2.16: A parallel plate capacitor with very large overlapping area compared to the distance between the plates.

The derivation for this capacitor is based on one of the Maxwell's equations, i.e. Gauss' law.

$$\nabla \cdot \vec{E} = \frac{\rho}{\epsilon} \quad (2.33)$$

In integral form and assuming uniform charge, this equation becomes:

$$\oiint_S \vec{E} \cdot d\vec{a} = \frac{q}{\epsilon}. \quad (2.34)$$

For large overlapping plates, the integral can be solved in the following way:

$$\oiint_S \vec{E} \cdot d\vec{a} = EA = \frac{q}{\epsilon} \rightarrow q = \epsilon EA. \quad (2.35)$$

With  $E$  the electric field normal to the surface. The capacitance is defined as:

$$C = \frac{q}{u}. \quad (2.36)$$

And voltage between plate  $a$  and plate  $b$  is defined as:

$$u = \Delta V = \int_a^b \vec{E} \cdot d\vec{l} = Ed \quad (2.37)$$

Substitution of 2.35 and 2.37 in 2.36 results in:

$$C = \varepsilon \frac{A}{d}. \quad (2.38)$$

For multiple parallel plates with equal area, e.g. comb fingers, it may be convenient to add a number of plate pairs  $N_p$  to the equation.

$$C = N_p \varepsilon \frac{A}{d_0 - u}. \quad (2.39)$$

Substituting Hooke's law results in the following equation.

$$C(F) = N_p \varepsilon \frac{kA}{kd_0 - F}. \quad (2.40)$$

Normal forces are measured non-differentially using the parallel plate capacitor structures. For small forces, the closing gap capacitor model can be linearized using the Maclaurin series:

$$C_z(F_z) \approx \sum_{n=0}^1 \frac{C_z^{(n)}(F_z)}{n!} F_z^n = \frac{N_{p,z} \varepsilon A_z}{d_{0,z}^2 k_z} F_z + C_z(0). \quad (2.41)$$

All parameters can be put in factor  $\beta_z$ :

$$C_z(F_z) \approx \beta_z F_z + C_z(0), \quad \text{with} \quad \beta_z = \frac{N_{p,z} \varepsilon A_z}{d_{0,z}^2 k_z}. \quad (2.42)$$

$C(F)$  is an expression for the total capacitance between two plates or two combs. As can be seen in the sensing structures in figure 2.15 and in the operating principles in figure 2.9 and 2.10, shear forces are measured differentially. The differential capacitance  $\Delta C_x$  is defined as:

$$C_{x,\pm} = C_{x,rest} \pm C_x \rightarrow \Delta C_x = \frac{C_{x,+} - C_{x,-}}{2}, \quad (2.43)$$

i.e. the actual difference in capacitance due to displacement of one side, which can be measured by calculating half of the difference of the two measured structures (i.e. two plates or two combs). For small forces, the differential closing gap capacitor model may be linearized using the Maclaurin series:

$$C_x(F_x) \approx \sum_{n=0}^1 \frac{\Delta C_x^{(n)}(F_x)}{n!} F_x^n \quad (2.44)$$

$$= \beta_x F_x, \quad \text{with} \quad \beta_x = \frac{N_{p,x} \varepsilon A_x}{d_{0,x}^2 k_x}. \quad (2.45)$$

The inverted  $\beta$ -factors are elements of calibration matrix  $\mathbf{K}$ , which maps the measured capacitances (corresponding to the defined capacitances in figure 2.15) to forces and torques.

$$\begin{bmatrix} F_x \\ F_y \\ F_z \\ T_x \\ T_y \\ T_z \end{bmatrix} = \mathbf{K} \begin{bmatrix} \Delta C_{x,1} \\ \Delta C_{x,2} \\ \Delta C_{y,1} \\ \Delta C_{y,2} \\ C_{z,11} \\ C_{z,12} \\ C_{z,21} \\ C_{z,22} \end{bmatrix}, \quad \text{with} \quad \mathbf{K} \in \mathbb{R}^{6 \times 8} \quad (2.46)$$

The elements in calibration matrix  $\mathbf{K}$  will be found by measurements and will be reviewed in part 4 'Characterization'.

## 2.5 Design of the suspended core

The details of the design of the suspended core are described in this section.

### 2.5.1 Computer aided design

The suspended core with v-shaped springs is drawn in the CAD software SolidWorks Professional 2012 SP1.0. The circular core has a diameter of 2.5 mm. All v-shaped springs are point symmetrically oriented around the center of the core and consist of two beams with a length of 480  $\mu\text{m}$  and a width of 108  $\mu\text{m}$ .

The structures in the handle layer have rounded corners. This is done for two reasons:

- it reduces the maximum stress because the beams are thicker at places where the deformation would be originally higher;
- the etching process does not allow very sharp corners. By using round corners in the simulations, the simulations become more true to nature.

A 2D-top drawing is exported to the CleWin 5.0.13 Layout Editor. The stage is extended with a hexagon structure around it and two fixation points on both sides. Chapter 3 will go into more detail about this.

All parameters and the calculated stiffnesses are available in table 2.2.

Table 2.2: Dimensions of the suspended core.

Quantity	Symbol	Value
Length of one spring part	$L$	480 $\mu\text{m}$
Width of the spring	$W$	108 $\mu\text{m}$
Thickness of the spring	$T$	400 $\mu\text{m}$
Number of spring triplets	$N_{3s}$	5
Diameter of the core	$D_{core}$	2.5 mm
Diameter of the sensor	$D_{sensor}$	9.24 mm
Stiffness in shear direction	$k_x$	$7.2 \cdot 10^6 \text{ N m}^{-1}$
Stiffness in normal direction	$k_z$	$1.9 \cdot 10^7 \text{ N m}^{-1}$

### 2.5.2 Stiffness and stress simulations

Two types of simulations were done. First, the sensor is simulated as if it is mounted on a very stiff supporting ring. This is done as verification of the mathematical model. Then, the sensor is simulated in a more realistic situation. The latter simulations are done to get an impression how the sensor will perform in the real world.

#### Ideally mounted

The simulations were done for a shear force of 10 N, a normal force of 10 N and a torque around a shear axis of 10 N mm. Table 2.3 shows the simulation results.

Table 2.3: FEM simulation results.

Quantity	Symbol	Value
Stiffness in shear direction	$k_x$	$8.9 \cdot 10^{-6} \text{ N m}^{-1}$
Maximum stress for $F_x = 10 \text{ N}$	$\sigma_{max,x}$	8.5 GPa
Stiffness in normal direction	$k_z$	$1.2 \cdot 10^{-7} \text{ N m}^{-1}$
Maximum stress for $F_z = 10 \text{ N}$	$\sigma_{max,z}$	4.0 GPa
Rotational stiffness around shear axes	$c_x$	41 N m rad $^{-1}$
Maximum stress for $T_x = 10 \text{ N mm}$	$\sigma_{max,\phi}$	0.92 GPa

The found stiffnesses are slightly different than the model predicts. This may be because of the rounded corners. The found stresses for the simulated forces and torques are quite high for silicon; it can be concluded that the sensor's maximum range for force and torque will be in the order of newtons and newton millimeters respectively.

### Realistically mounted

The handle layer of the sensor is supported by a solid ring like is illustrated in figure 2.17. The material was unknown in the simulation phase and can vary between a plastic ( $\sim 4$  GPa) and a ceramic ( $\sim 400$  GPa). Polysilicon (169 GPa) was used in these simulations. The ring has a thickness of  $500\ \mu\text{m}$ , the suspended core has a thickness of  $380\ \mu\text{m}$ . Latter property dates back to when it was assumed that SOI-wafers with a handle layer of  $380\ \mu\text{m}$  were going to be used.

Figure 2.17 shows the boundary conditions of the FEM simulation. The marked boundaries in figure 2.17a are fixed boundaries. The marked boundaries in figure 2.17b are loaded. By applying the loads in opposite shear direction at latter boundaries, a torque can be simulated.

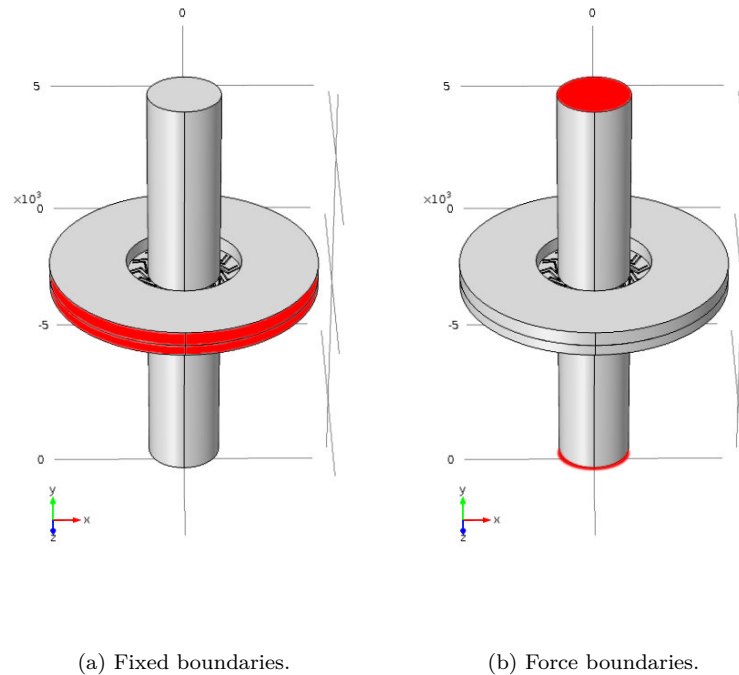


Figure 2.17: The model with boundary conditions.

The stiffness may be influenced by the supporting ring on top of the handle layer. Figure 2.18 shows the deformation of a section of the sensor with scale factor of 1000.

It appears that the support's influence is negligible for shear forces. For normal forces, the compliance is for 0.77% the consequent of the v-shaped springs. For torques, this is 0.81%. It turns out that it is important to support the sensor with a stiff material, a ceramic printed circuit board (PCB) may be used for example.

The v-shaped springs have optimized shapes for stress distribution. The performance of this optimization is analyzed using figure 2.19a for shear forces, figure 2.19b for normal forces and figure 2.19c for torques.

The v-shaped springs build up high stresses in the corners when loaded in the direction the v-shape points (figure 2.19a). In the other direction, the stress is minimal. In normal direction, the stress is especially concentrated at the corners (figure 2.19b), uniformly for all springs. The stress distribution for torques is almost the same as for shear forces (figure 2.19c).

The exact maximum stress before damage is not determined, for this is dependent of the direction. 10 N and 10 N mm are estimated as the maximum force and torque respectively.

### 2.5.3 Alternative designs

Next to the suspended core simulated in subsection 2.5.2, two different spring systems were designed. The three suspended cores are summarized in table 2.4.

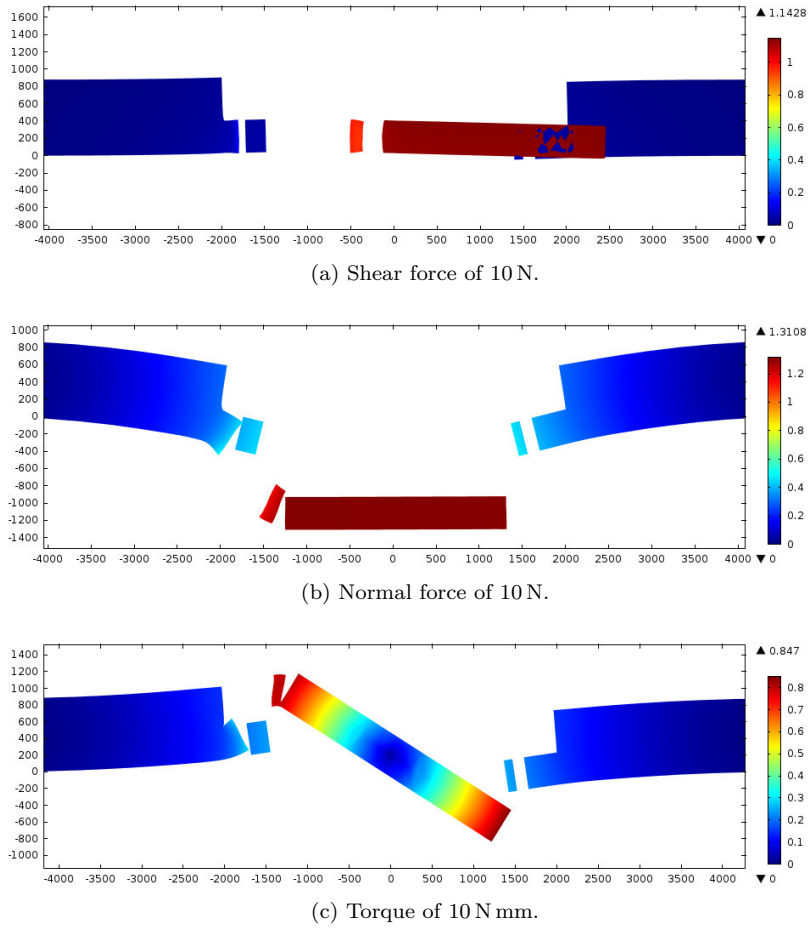


Figure 2.18: Deformation analysis using FEM.

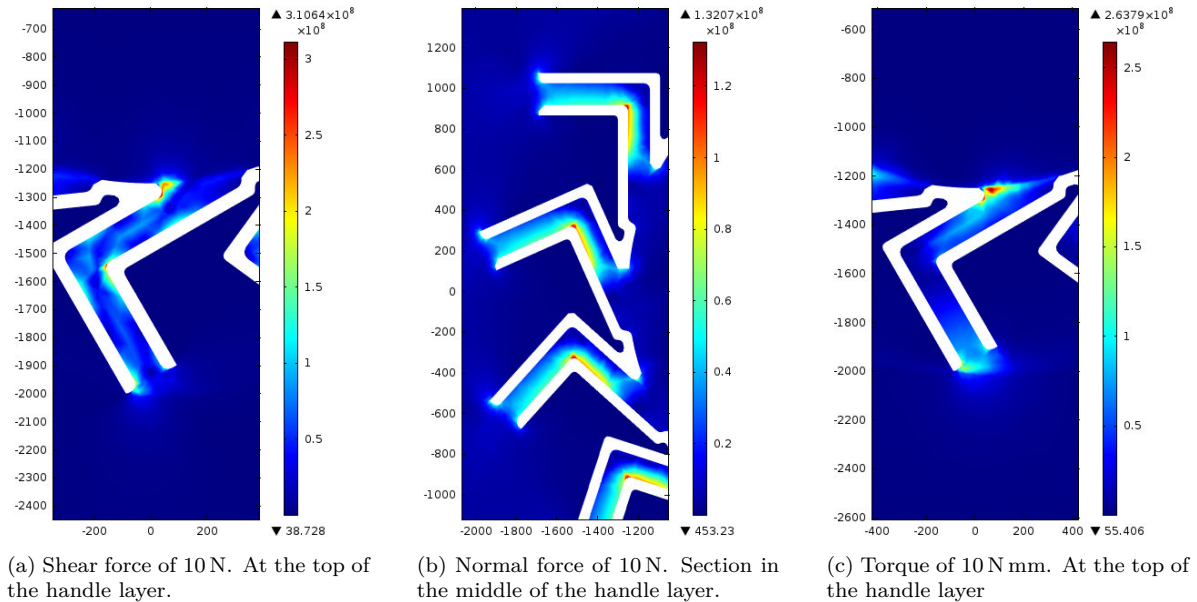


Figure 2.19: Stress analysis using FEM for a shear force of 10 N pointed to the right.

Table 2.4: Three different spring systems for the suspended core.

Number of spring triplets $N_{3s}$	Shear stiffness	Normal stiffness	Spring part length $L$	Spring width $W$
1	$0.83 \text{ N } \mu\text{m}^{-1}$	$1.5 \text{ N } \mu\text{m}^{-1}$	$470 \text{ } \mu\text{m}$	$84 \text{ } \mu\text{m}$
5	$8.3 \text{ N } \mu\text{m}^{-1}$	$7.6 \text{ N } \mu\text{m}^{-1}$	$480 \text{ } \mu\text{m}$	$108 \text{ } \mu\text{m}$
9	$45 \text{ N } \mu\text{m}^{-1}$	N/A	$480 \text{ } \mu\text{m}$	$132 \text{ } \mu\text{m}$

## 2.6 Design of the sensing structures

The details of the design of the sensing structures are described in this section.

### 2.6.1 Computer aided design

The device layer with the sensing structures are drawn using the same software as the handle layer. SolidWorks was used to draw most parts of the device layer, including the comb-structures and the bond pads. The parallel plate structures were scripted and drawn in CleWin.

### 2.6.2 Comb-structures in the device layer

The comb-structures consist of two parts: the transmission from the mesa to the combs (the discriminating spring) and the finger-structures.

#### Discriminating spring and overload protection

The comb-structures consist of combs mounted on a one degree of freedom stage which is supported by eight single flexures. Spring and lever structures are used to separate the different force components of the mesa into comb-structure movements (figure 2.20).

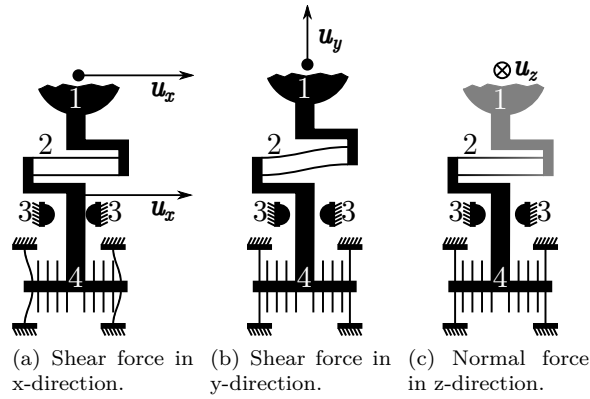


Figure 2.20: Transmission (2) from mesa (1) to comb-structures (4). There are bumps (3) to prevent snapping of the fingers due to overloading.

This spring system was modeled using equations 2.13 in MATLAB R2012b 8.0.0.783 and verified by simplified FEM simulation. The transmission has (for small displacements) very high stiffness in x-direction and therefore transfers the full x-displacement from the mesa to the comb-structures. In z-direction, the stiffness of the transmission springs are more than 80 times lower than the springs of the comb-structures, so less than 2% of the z-displacement of the mesa is transferred to the comb-structures. In y-direction, the stiffness of the transmission springs are negligible compared to the the springs of the comb-structures making the comb-structures almost insensitive for y-displacements. In this way, crosstalk between the different force components is mechanically minimized.

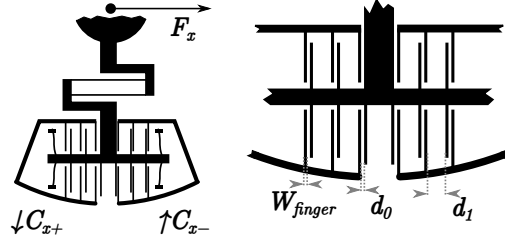
All comb-structures have protection against snapping due to overloading: the stage will hit the bumps in figure 2.20 first before the fingers of the stage will snap to the fingers of the stator, as the distance between the finger pairs is  $7\ \mu\text{m}$  and the distance between the bumps and the stage is  $5\ \mu\text{m}$ .

#### Finger optimization

The shear displacements are measured differentially. The stator consists of two symmetric electrically isolated parts (figure 2.21). Displacement of the stage results in an increasing gap at one half of the comb-structures and a decreasing gap at the other half of the comb-structures.

The asymmetric positioning ( $d_1/d_0$ -ratio in figure 2.24b) of the shuttle-fingers between the stator-fingers is optimized, for a smaller  $d_1/d_0$ -ratio allows more finger structures but increases the parasitic capacitance and a larger  $d_1/d_0$ -ratio decreases the parasitic capacitance but takes more space. The curve in figure 2.22 is derived from equation 2.40, its maximum is where:

$$\frac{\partial}{\partial d_1} \frac{1}{d_0 + d_1 + 2W_{finger}} \left( \frac{1}{d_0} - \frac{1}{d_1} \right) = 0. \quad (2.47)$$



(a) Differential capacitance change when loaded. (b) Close-up of the finger structures with dimensions.

Figure 2.21: Electrical design of the comb-structures.

The fingers have a width  $W_{finger}$  of  $7\ \mu\text{m}$ . The minimum distance between the fingers is  $7\ \mu\text{m}$  which is used for  $d_0$ . Choosing  $\sim 20\ \mu\text{m}$  for  $d_1$  leads to maximum capacitance change. All parameters are summarized in table 2.5.

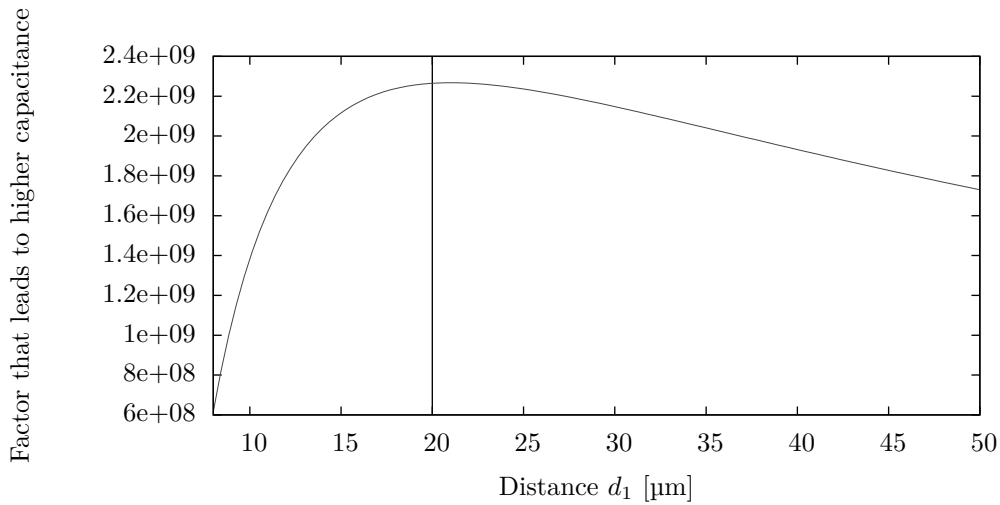


Figure 2.22: Optimization of the finger distances: choosing  $d_0$  the maximum of the function will consequent in the highest capacitance.

Table 2.5: Parameters of the comb-structures.

Quantity	Symbol	Value
Number of finger pairs	$N_{p,x}$	149
Average overlapping area per finger pair	$A_x$	$1.2 \cdot 10^{-8}\ \text{m}^2$
Distance between fingers	$d_0$	$7\ \mu\text{m}$
Distance between finger pairs	$d_1$	$20\ \mu\text{m}$
Width of a finger	$W_{finger}$	$7\ \mu\text{m}$
Average length of a finger	$L_{finger}$	$240\ \mu\text{m}$
Thickness of a finger	$T_{device}$	$50\ \mu\text{m}$

### 2.6.3 Parallel plate structures in the device layer

The parallel plate structures consist of flat plates that form a capacitor with the handle layer. The surface area of the plates is such that the capacitance is in the same order as the capacitance of the comb-structures.

#### Electrical connections

The plate is electrically connected to the bondpad with springs that are compliant in all directions. In figure 2.23, one of the normal sensing structures is shown.

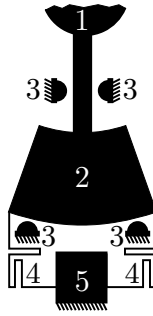


Figure 2.23: Capacitor plate (2) is directly coupled with mesa (1). Wires (4) connect the capacitor plate to the bondpand (5) and have no effect on the mechanics due to there folds. There are bumps (3) to prevent snapping of the plates due to shear overloading.

There are several parallel plate capacitor structures in the sensor for reference measurements. These capacitors are not able to move and can be used to compensate for temperature and humidity effects.

### Grid efficiency

Since floating structures need to have holes for the etching process (that will be described in part 3 'Fabrication'), one of the normal structure plates is a grid of silicon beams. The parallel plate capacitor model will be highly influenced, as the overlapping surface area decreases a lot. However, the fringing effects of the walls inside the grid may compensate. This effects were modelled using FEM.

Two overlapping square plates of  $400\ \mu\text{m}$  of  $400\ \mu\text{m}$  were drawn: one with  $1\ \text{V}$  and one with  $0\ \text{V}$  of potential. A box of air was modelled around the two plates and is much larger than the plates. After simulation, the charge density of one plate was integrated and is, with a voltage of  $1\ \text{V}$ , equal to the capacitance of two flat plates.

Then, one of the plates was substituted by a grid with square holes of  $15\ \mu\text{m}$  by  $15\ \mu\text{m}$  and beams with a width of  $7\ \mu\text{m}$ . The integrated charge density turned out to be approximately  $11\ \%$  lower compared to the parallel plate simulation. It can be concluded that the fringing effects compensate for the holes in the plate. Both situations are sketched in figure 2.24.

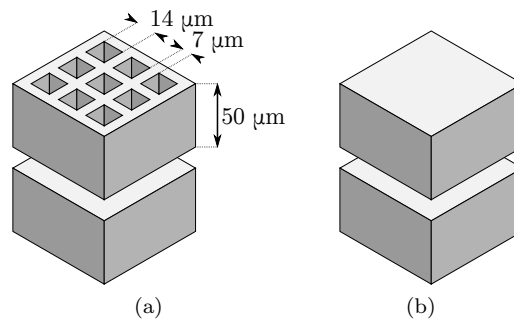


Figure 2.24: Parallel plate structure simulations. The capacitance of the situation with one perforated plate (a) performs  $11\ \%$  lower compared to the situation with two solid parallel plates (b).

### 2.6.4 Prevention of stiction

To achieve high sensitivity, large capacitor structures are needed. But care must be taken when designing such large floating structures, as stiction may occur. All large floating structures (figure 2.21 and figure 2.23) can be modeled as doubly clamped beams since they are always supported at two ends, this is illustrated in figure 2.25.

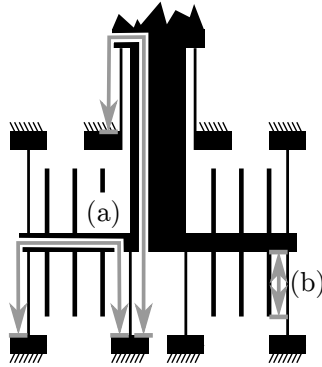


Figure 2.25: Paths in the structures that can be modeled as doubly clamped beams (a) or beams with a free end (b).

Following equation gives the maximum length for these structures [37].

$$L_{critical} = 2.9 \sqrt[4]{\frac{3}{8} \frac{ET^3 g^2}{\gamma_s}} \approx 3000 \mu\text{m}, \quad (2.48)$$

with  $L_{critical}$  the critical length,  $E$  Young's modulus (of silicon),  $T$  the thickness of the beams (i.e. the thickness ( $50 \mu\text{m}$ ) of the device layer),  $g$  the gap between the device layer and the handle layer ( $4 \mu\text{m}$ ) and  $\gamma_s$  the adhesion energy (assumed to be  $100 \text{ mJ m}^{-2}$ ). All doubly clamped structures are less than  $3000 \mu\text{m}$  in length. All structures that have a free end are always shorter than  $1000 \mu\text{m}$ .

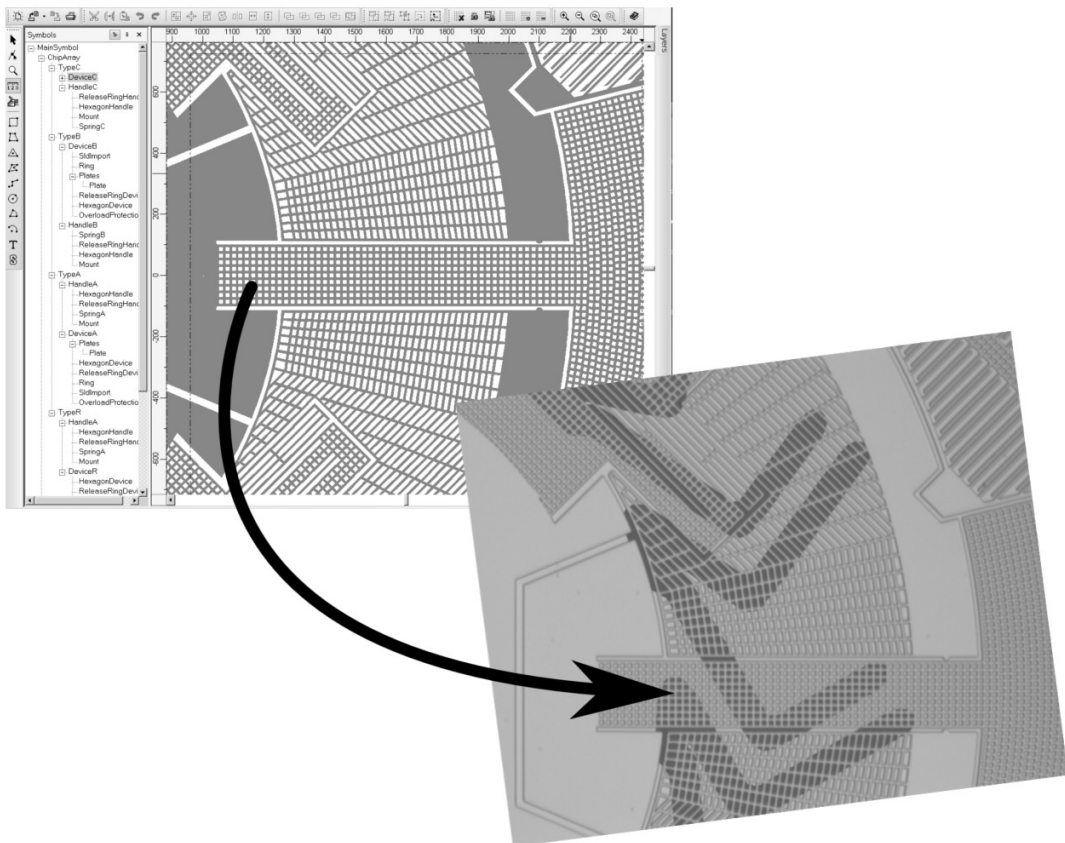
## 2.7 Conclusion

A six degrees of freedom force/torque sensor is designed. Its behavior is described using a mathematical model and the details of the design of the sensing structures are explained. FEM simulations predict that the designed sensor will satisfy the requirements mentioned in the introduction.

- The sensor should be relatively trivial to fabricate using well-known technologies and the technology should be highly reproducible, i.e. the fabrication should take less than two months.
  - ▶ The proposed design can be made in an SOI-wafer which can be treated with conventional silicon fabrication steps.
- The sensor should support measurements in multiple degrees of freedom.
  - ▶ The designed stage itself supports six degrees of freedom. Sensing structures for shear and normal displacements are designed.
- The sensor should have a competing sensitivity, in comparison with with the sensors summarized in the literature study.
  - ▶ Using comb-structures and large parallel plates, this should be possible.
- The sensor should be able to handle human forces, e.g. multiple newtons.
  - ▶ Stress analyses prove that the stage can handle forces up to 10 N and torques up to 10 N mm.
- The sensor should be small, preferable less than 1 cm<sup>2</sup> with a thickness of less than 1 mm.
  - ▶ All models and simulations are based on dimensions that are smaller than the preferable maximum.

The design of the fabrication process and the design rules are not proposed in this part. This is included in the next part 'Fabrication'.

---



---

*Author*  
Dennis Alveringh

*Supervised by*  
dr. ir. Henri Jansen  
ing. Meint de Boer  
dr. ir. Remco Wiegerink  
Robert Brookhuis MSc

## 3.1 Introduction

The design, realization and fabrication of a six degrees of freedom force/torque sensor had to fit in a master graduation assignment of roughly eight months, the fabrication was therefore limited in time and money. Effort has been done to make the fabrication process as cheap, quick and robust possible as possible. How this is done is presented in this part.

This part is roughly divided in two sections. The first section describes the theory and the design of the fabrication process. The design rules will be derived and the used technologies will be explained.

The second section describes the fabrication in practice and reflects on every step in the process. All problems that occurred during the process and their solutions are explained in this section as well.

## 3.2 Design of the fabrication process

This section describes the design of the fabrication process from the theory explained in previous part. First, an overview of the device with the design rules will be discussed, then, the process steps with the associated technology will be explained.

### 3.2.1 Device overview and design rules

The force/torque sensor will be simply made of two layers. A relatively thick layer of  $400\ \mu\text{m}$  will contain large spring structures to form a six degrees of freedom stage that has the same order of stiffness in all directions. A thinner layer of  $50\ \mu\text{m}$  will contain capacitor plates oriented in all three dimensions for capacitive measurements.

Without going deeply into the process, this will be done in subsection 3.2.2, it can already be concluded that:

- a SOI-wafer will be etched on both sides, so this will be a typical bulk micromachining device;
- the spring structures will be relatively large;
- the capacitor structures (fingers) will be relatively small.

Reducing the size of the capacitor structures will lead to a better performance, because smaller structures allow more capacitor fingers and that leads to a higher sensitivity. Nevertheless, this also leads to a higher aspect ratio and therefore more difficult microfabrication. One of the main principles of this project is the high feasibility, for this project is done as master thesis and there is just limited time for the microfabrication process. The fabrication process is therefore tried to make as smoothly as possible with strict design rules and taking possible problems into account in the design stage of the project.

The designs of the two layers are printed in figure 3.1. Because a SOI-wafer is used and the two outer layers of the SOI-wafer are named “device layer” for the thin layer and “handle layer” for the thick layer, the masks bear the same name.

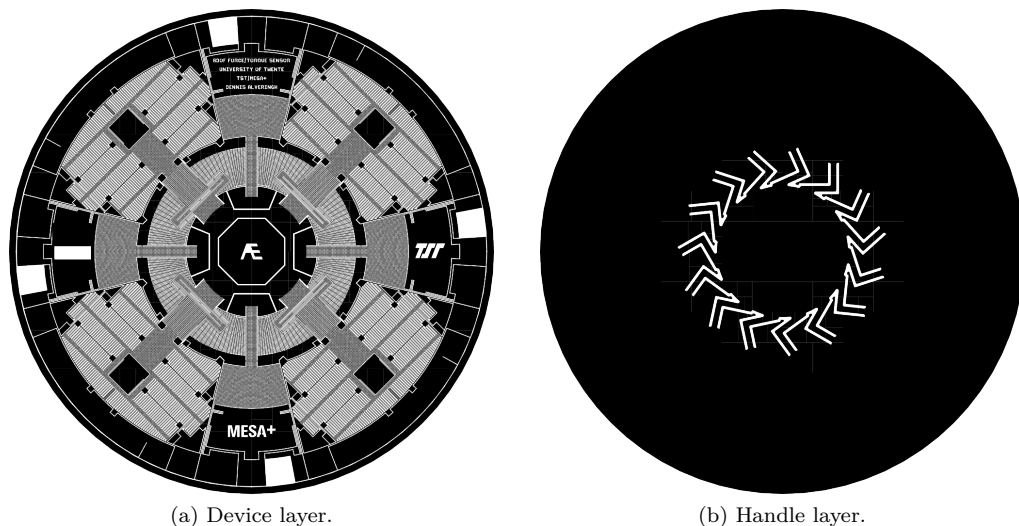


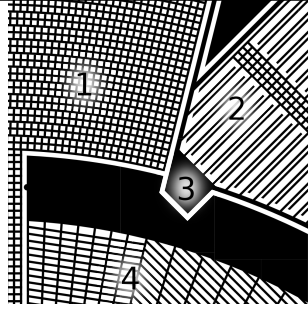
Figure 3.1: Masks of the six degrees of freedom force and torque sensor for a single chip. White parts will be etched.

The mask for the handle layer has relatively large structures. Besides, it did not really matter for the design how large the parts that will be etched are. The rule of thumb of 1:10 [23] for aspect ratio is maintained, giving a minimum size for the trenches of  $40\ \mu\text{m}$ . The trenches are chosen slightly larger with  $50\ \mu\text{m}$ .

The device layer contains more complicated structures. Table 3.1 gives the design rules that are related to the embedded figure with a closeup of the most complicated structures.

The chips will be made in a  $100\text{mm}$  wafer as shown in figure 3.2. Because all chips are circular, hexagon packing is used to optimize the use of the surface area of one wafer. Since the performance of the fabrication process is the best in the center of the wafer, the four types of chips are distributed in an intelligent way to increase the chance of working samples of each type.

Table 3.1: Design rules with a closeup of the device layer.



- 
- 1 Frame with holes of at least  $14\ \mu\text{m}$  and beams of  $7\ \mu\text{m}$  at maximum.
  - 2 Comb fingers with a length of  $300\ \mu\text{m}$  at maximum and with a width of  $7\ \mu\text{m}$ . There is  $7\ \mu\text{m}$  spacing between the fingers, making this the smallest open areas in the mask.
  - 3 All anchors are at least  $100\ \mu\text{m}$  by  $100\ \mu\text{m}$ .
  - 4 All areas that are not in use are either solid or framed, leaving holes of maximum  $40\ \mu\text{m}$  by  $40\ \mu\text{m}$ .
- 

There is a trench around the chip in both the handle layer and the device layer. There are small fixations points on both sides of the chip to fix the chips in the wafer. Releasing of the samples can be simply done by breaking them out. This technique doesn't need a dicing machine or other advanced devices and it allows arbitrary shapes for the chips. The trenches around the chips are the same as the smallest trenches on the chip (i.e.  $7\ \mu\text{m}$  for the device layer and  $50\ \mu\text{m}$  for the handle layer) to prevent damage to the oxide layer and possible leakage while etching.

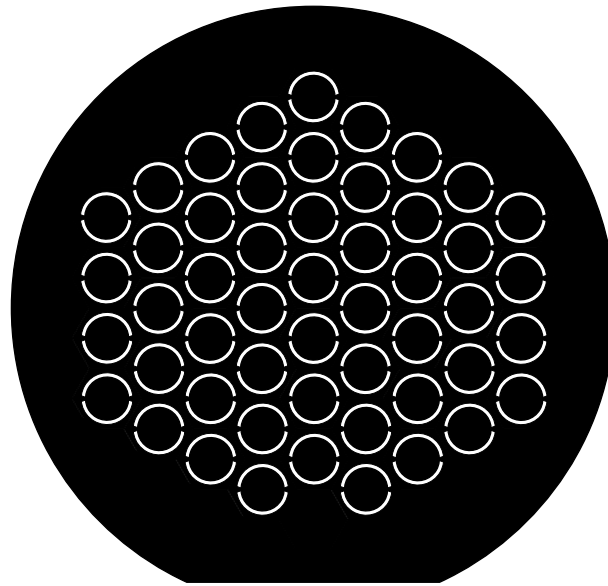


Figure 3.2: Impression of the location of the chips and how they will be broken out of the wafer.

### 3.2.2 Process

As already mentioned before, a SOI-wafer will be anisotropically etched on both sides and a release etch will be performed to release the sensing structures and the chips. To perform this, a process flow is designed.

Patterning the wafer can be done using only photoresist to cover the parts that must not be etched, but to make the process more robust, a hard mask of silicon oxide will be used. There are two reasons to use a hard mask: the selectivity for etching is better and the oxide mask will compensate for the internal stress of the already existing oxide layer in the wafer (see figure 3.3).

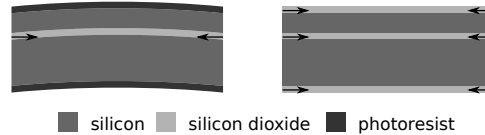


Figure 3.3: Deformation due to stress for a mask with photoresist and a mask with silicon dioxide.

The deposition of oxide is done using thermal oxidation and will be explained in more detail in subsection 3.2.3.

The oxide is patterned using photolithography and deep reactive ion etching. This is done on both sides, it does not really matter which side will be patterned first. After both mask etching steps, the photoresist is removed.

After patterning the mask on the wafer, deep reactive ion etching will be used to etch completely through the layers. The handle layer is done first, because this layer has larger structures and has to lay down on the chuck when the device layer will be etched.

The process ends with the release etch. The deposited silicon oxide on the wafer and free parts of the box layer will be etched. The box layer will be under etched for several micrometers to release the sensing structures in the device layer.

The chip can be broken out of the wafer and mounted with the handle layer to a PCB with a hole. The bondpads on the device layer can be wirebonded to the PCB and a stylus can be glued on the center stage to make it easier to characterize.

Figure 3.4 with table 3.2 explains the process graphically.

Table 3.2: Process with reference to figure 3.4.

a	Substrate: SOI wafer with 400 $\mu\text{m}$ handle layer, 4 $\mu\text{m}$ box layer and 50 $\mu\text{m}$ device layer.
b	Oxidation.
c	Lithography on handle layer.
d	Etching of oxide.
e	Resist stripping.
f	Lithography on device layer.
g	Etching of oxide.
h	Resist stripping.
i	Etching of handle layer.
j	Etching of device layer.
k	Etching of oxide.
l	Mounting on PCB.

### 3.2.3 Used technologies

This subsection describes the theory of the most essential fabrication steps briefly: oxidation, photolithography, deep reactive ion etching and etching with HF.

#### Oxidation

There are roughly two types of oxidation: dry oxidation and wet oxidation. Dry oxidation uses oxygen in a furnace between 800  $^{\circ}\text{C}$  to 1200  $^{\circ}\text{C}$  to oxidize the substrate. Wet oxidation uses water vapor instead of oxygen. Figure 3.5 from reference [11] gives the oxidation speed at several temperatures.

It seems that wet oxidation is faster than dry oxidation. The chemical equation that is relevant for wet oxidation is as follows.

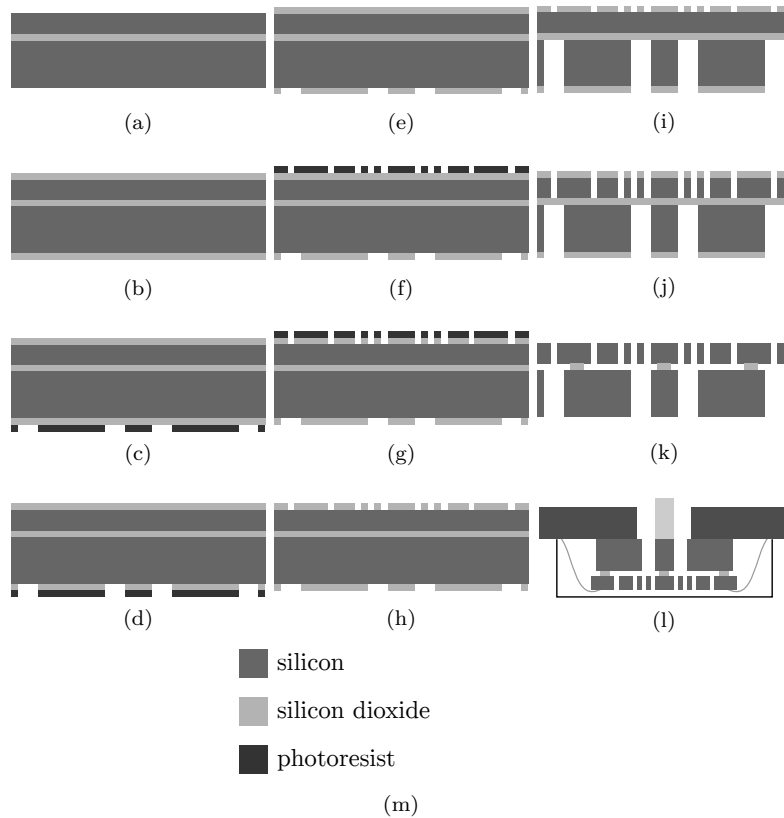


Figure 3.4: Fabrication process with each step explained in table 3.2.

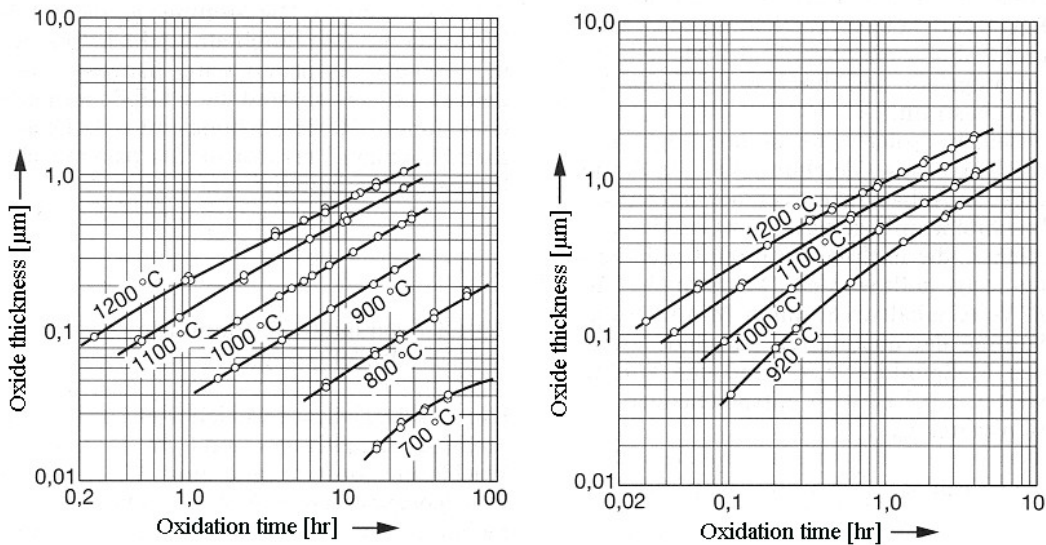


Figure 3.5: Oxide thickness versus the time of oxidation for dry oxidation and wet oxidation respectively. Source: [11].



The silicon will react directly with the water and will form silicon dioxide and hydrogen gas. Extrapolation of the curve in figure 3.5 will give that an oxidation time of 14 h will result in a layer thickness of 2.1  $\mu\text{m}$ . This will do as hard mask.

### Photolithography

The photolithography in this project is quite trivial and the detailed process will be discussed in section 3.3. However, there is aimed for a slightly thicker coating of resist (2  $\mu\text{m}$ ) than the standard available

photoresist OiR 907-017 produces after spinning with 4000 rpm ( $1.7\ \mu\text{m}$ ). Figure 3.6 was taken from the resists' datasheet and shows that spinning the resist on 3000 rpm for 30 s will produce a layer of  $2\ \mu\text{m}$ .

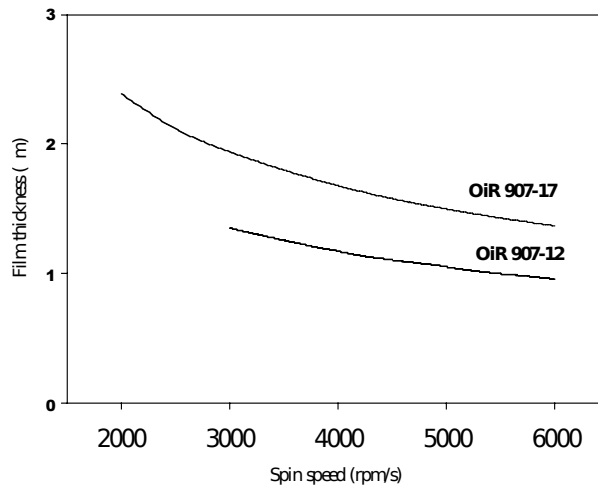


Figure 3.6: Layer thickness versus spin speed of OiR 907 series positive resist. Source: [17].

The exposure time may be influenced by this, but the standard time of 4 s will be tested first with a dummy wafer.

### Deep reactive ion etching

Deep reactive ion etching (DRIE) uses a reactive plasma for etching and consists roughly of two etching principles: physical etching by ion bombardment and chemical reactions that occur with the etchant and the substrate. Characteristic of this etching technology is the deposition pulse of the passivation layer to prevent the sidewalls for etching after each etching pulse. These two pulses iterate several times and makes it possible to etch with high anisotropy and high aspect ratios.

The plasma is created and maintained using a coil (inductive coupled plasma (ICP)) and an electric field (capacitive coupled plasma (CCP)). Physically, the plasma begins with dissociation: the gas splits in separate molecules or atoms. Then ionization occurs: the molecules or atoms become ionized due to the removal of an electron or electrons. The energy of the plasma becomes higher by excitation: electrons in the molecules or atoms are going to a higher energy state. After this, free radicals are generated and are able to etch the sample or deposit a passivation layer. Finally, recombination occurs, making the excited electrons go back to their original energy level and releasing a photon that can be seen as normal light.

A schematic view of a DRIE system can be found in figure 3.7. The most important parameters of the DRIE process are graphically shown in the figure.

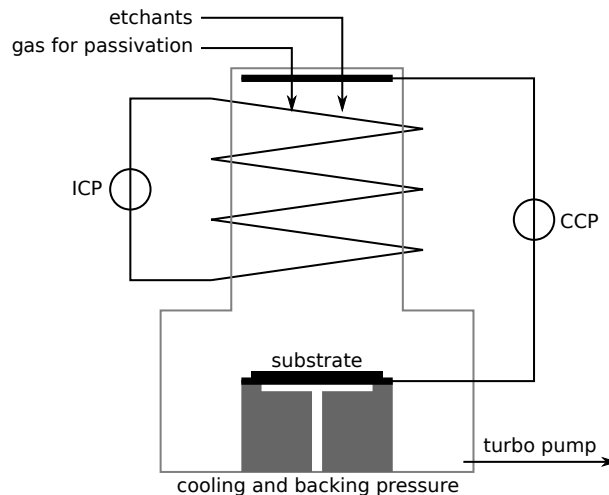


Figure 3.7: Schematic view of a DRIE system with the most important parameters that can be changed to achieve a certain etch rate, selectivity and anisotropy.

High ICP power leads to a denser plasma and to a higher concentration of radicals; a higher etch rate can be achieved, but the selectivity will be lower. A High CCP power leads to higher energy per ion

and a more straight ion direction; the etching will be more anisotropic with a lower selectivity [16] [22]. The process can also be tuned with the ratio between the etching step and the passivation step: etching long (e.g. for 6 s) compared to depositing the passivation layer (e.g. for 0.5 s) will cause rough scallops, but fast etching. Besides, large areas will etch much faster than small areas. The handle layer will be therefore etched in this way (fast and rough), while the much thinner device layer will be etched with less ICP power and long passivation layer deposition time.

A common etchant for silicon is sulfur hexafluoride ( $\text{SF}_6$ ) and is in gas phase at room temperature. Octafluorocyclobutane ( $\text{C}_4\text{F}_8$ ) is a common gas for passivation layers.

A common etchant for silicon dioxide is methane ( $\text{CH}_4$ ) with helium (He). Octafluorocyclobutane is also for oxide etching a common gas for passivation.

### Etching with HF

Hydrofluoric acid, a solution of hydrogen fluoride (HF) in water, is an acid that can be used to etch silicon dioxide ( $\text{SiO}_2$ ), because of its high selectivity: it has an etch rate of  $1 \mu\text{m min}^{-1}$  [15] for  $\text{SiO}_2$  compared to a negligible etch rate for silicon. The reaction of  $\text{SiO}_2$  with HF is as follows.



There will be etched from top and bottom at the same time, the oxide layer of  $4 \mu\text{m}$  will be etched through in approximately two minutes.

The release etch, under etching of approximately  $5 \mu\text{m}$  will be done using HF in the vapor phase, because the capillary force of the HF as liquid pulls the microstructures in the device layer to each other or to the handle layer.

Water vapor (from the air) adsorbs on the surface of the  $\text{SiO}_2$  forming silanol groups  $\text{Si}(\text{OH})_4$ . These groups can be attacked by HF. The reaction equations, including the adsorption of water, are as follows.



Heating up the sample to be etched makes it evaporate more water and this results in a lower etch rate. But even with low temperatures, the etch rate is far lower than the wet etch technique with HF: it is about  $5 \mu\text{m h}^{-1}$  [4].

### 3.3 Fabrication report

This section reports the experimental flow in the cleanroom. All problems and just-in-time changes are described as well.

#### 3.3.1 Dummy wafers

Ten wafers (525  $\mu\text{m}$ , p-type silicon wafers) were used as dummy wafers. At some process steps, like etching, the dummy wafers were used to test the settings.

#### 3.3.2 Oxidation

The wafers should be clean and should be, because a metal-free oven will be used, also metal-free before oxidation. A standard cleaning process was used with 10 minutes  $\text{HNO}_3$  at room temperature with a concentration of 99% and 10 minutes  $\text{HNO}_3$  at 95  $^\circ\text{C}$  with a concentration of 69%. After rinsing and drying, the furnace was prepared for loading.

Wet oxidation was done using a furnace (Tempress) at 1150  $^\circ\text{C}$ .  $\text{H}_2\text{O}$  with  $\text{N}_2$  gas flew with 2  $\text{L min}^{-1}$  in the furnace. The wafers were 14 hours in the furnace. Thickness measurement was done using a Plasmos SD2002 Ellipsometer. The wafer is measured at 25 points with an average thickness of 1963 nm with a standard deviation of 3.86 nm.

#### 3.3.3 Lithography

One SOI-wafer and five dummy wafers were coated with positive photoresist (Fujifilm OiR 907-17). After 90 s baking at 95  $^\circ\text{C}$ , exposure of the resist has been done using an EVG EV620 mask aligner with an Hg-lamp of 12  $\text{mW cm}^{-2}$  for 4 s. The wafer with the resist went on the hotplate for an after exposure bake at 120  $^\circ\text{C}$  for one minute.

Development has been done using OPD4262 from Fujifilm for one minute. After rinsing and drying, a hard bake was performed. This caused non-uniformity of the resist as can be seen in figure 3.8. The lithography has been done again without hard bake to reduce this problem.

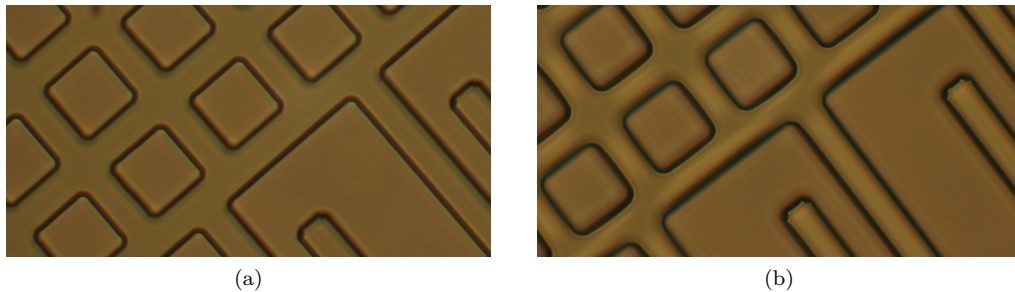


Figure 3.8: Resist without (a) and with (b) hard bake. Photos are taken from a dummy wafer without hard bake and a SOI-wafer with hard bake.

#### 3.3.4 Etching of oxide

A dummy was used to test the etching process. A recipe using  $\text{CH}_4$  at 15 sccm (standard cubic centimeters per minute) and He at 150 sccm was used to create the etching plasma in an Adixen AMS100.  $\text{C}_4\text{F}_8$  was used for passivation and flows with 15 sccm into the chamber. The electrode with wafer was cooled down to  $-10^\circ\text{C}$  and the pressure in the chamber was  $8.5 \cdot 10^{-3}$  mbar. The ICP power was set at the system's maximum of 2500 W and the CCP power was effectively 350 W (pulsed: 70 ms at 500 W and 30 ms off).

This should result in an etch rate of approximately  $0.5 \mu\text{m min}^{-1}$  for the silicon oxide and  $0.05 \mu\text{m min}^{-1}$  for the resist. This makes an etch time of 4.5 min enough. After inspection with an optical microscope it was seen on the color that there was still oxide left, compared with the chart in [20]. After etching for six minutes, all oxide was gone.

#### 3.3.5 Resist stripping

Resist stripping was done in  $\text{O}_2$ -plasma using a Tepla 300E for ten minutes on 500 W with an oxygen flow of 200 sccm. To make sure all resist was removed, the wafer is put into  $\text{HNO}_3$  for twenty minutes.

Lithography, etching of oxide and resist striping is done for both sides of the wafer with the same configurations.

### 3.3.6 Etching of handle layer and device layer

An Adixen AMS100 is used for etching the handle layer and device layer. It uses obviously a different gas ( $\text{SF}_6$ ) than for oxide etching. The handle layer is etched first and is etched with a faster, but rougher, configuration than the one for the device layer etch. The etching process is first tried out with dummy wafers.

The handle layer is etched at maximum ICP power of 2500 W with a CCP power of effectively 50 W (pulsed). The etchant  $\text{SF}_6$  flew with 500 sccm into the reaction chamber for 4 s; the passivation step is done for 0.5 s with 175 sccm ( $\text{C}_4\text{F}_8$ ). The wafer is cooled down at the backside to  $-40^\circ\text{C}$ . The wafer underwent the process for 35 min.

The device layer is etched at less ICP power than than the handle layer, 1500 W, and a CCP power of 100 W. The etchant flow is slightly higher (550 sccm) and the time is a little higher (6 s) to increase the etching speed. The passivation step is much longer than for the handle layer etch: 2 s with 200 sccm. The backside is cooled down to  $-10^\circ\text{C}$ . The device layer etch took 16 min.

The pictures in figure 3.9 give an impression of the etching performance.

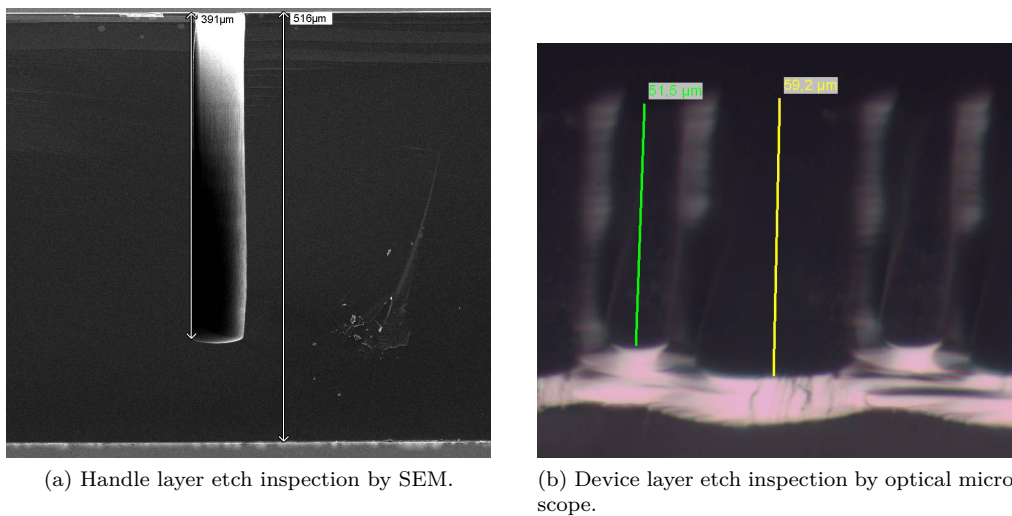


Figure 3.9: Inspection of etching performance.

It is clear that the etching speed was despite of the low ICP power and long passivation steps not uniform for the device layer etch, but there is a good etch stop (oxide) in the SOL-wafer to overcome this. To make shure that the small trenches are also etched completely through, the etching time is increased by 1 min.

The etching time for the handle layer is also increased, by 2 min.

### 3.3.7 Octafluorocyclobutane removal

After the etching process, there is still a passivation layer at the walls of the structures. The octafluorocyclobutane should be removed, as it can suit between the structures and influence the performance of the sensor. Because octafluorocyclobutane is an organic substance, it can be cleaned using a piranha solution. A piranha solution consists of sulfuric acid ( $\text{H}_2\text{SO}_4$ ) and hydrogen peroxide ( $\text{H}_2\text{O}_2$ ).

The photo in figure 3.10 was taken after piranha cleaning.

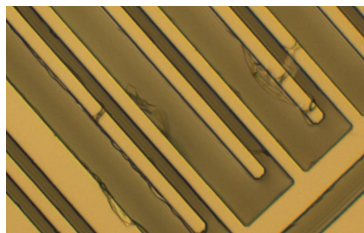


Figure 3.10: Octafluorocyclobutane contamination after DRIE and piranha cleaning.

The contamination is removed from the walls, but still between the structures. O<sub>2</sub> plasma cleaning is used to remove the contamination completely.

### 3.3.8 Releasing and ultrasonic cleaning

The samples can be broken out after both etching steps, as there is only the small fixation on the edges and the thin silicon dioxide membrane left to hold them in the wafer. Breaking was done by pushing with tweezers at one of the fixations at a sensor while the wafer was fixed at the edges. Unfortunately, the fixations were too strong causing the need for a large force to remove the chips from the wafer. Some chips broke because of this and the intact chips were contaminated by particles.

The contaminated chips were put in an ultrasonic bath for ten minutes in acetone and ten minutes in isopropanol. The ultrasonic bath has piezo elements that cause vibrations in the liquid and the chips. These vibrations remove the particles, but damaged finger structures on some chips. Most particles were removed in this way.

### 3.3.9 Release etch

One of the chips of the wafer was pushed out of the wafer to test the etching process. This chip was put in 50% HF for two minutes. The device layer was pulled off using tape and inspected with an optical microscope (figure 3.11).

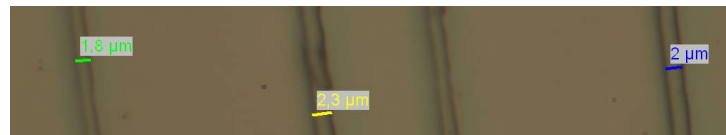


Figure 3.11: Oxide left after wet etching for the 7 μm wide finger structures.

The etching was faster than expected, the structures were already underetched for about 2.5 μm. Nevertheless, all structures were still fixed to the handle layer.

A few chips were put out and underwent the wet etching. Then, the chips were electrostatically mounted on the chuck in the vapor HF setup for half an hour to be sure that there was no oxide left. The same trick with the tape was used and the anchors were inspected. These were several micrometers underetched, which is enough to release the structures and not too much to release the anchors.

Figure 3.12 shows scanning electron microscope (SEM) photos of the device after the release etch.

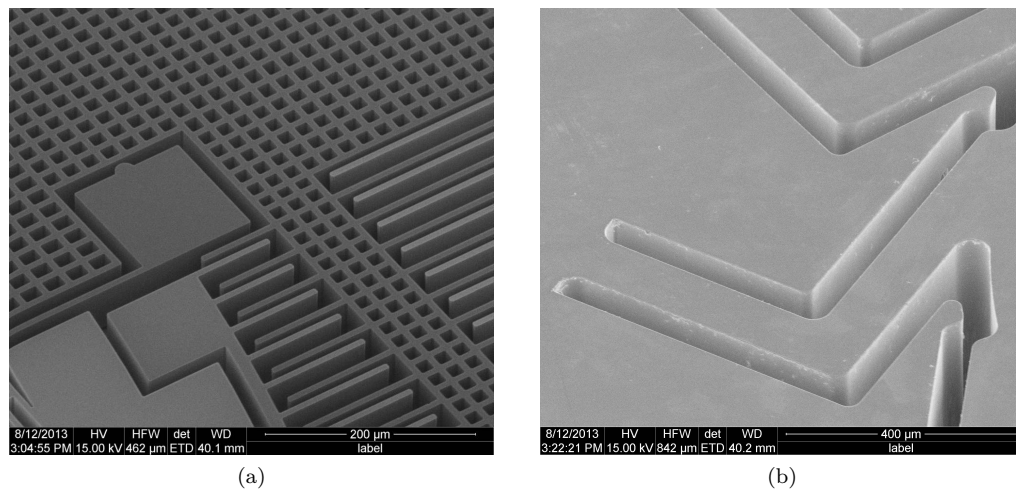


Figure 3.12: SEM closeups of the device.

### 3.3.10 Mounting on PCB

A hole is drilled in a PCB. The sensor is mounted with handle layer on the PCB using UV glue that cures when exposed to UV light. The sensor is wirebonded and a stylus is mounted on the center stage through the hole in the PCB (figure 3.13).

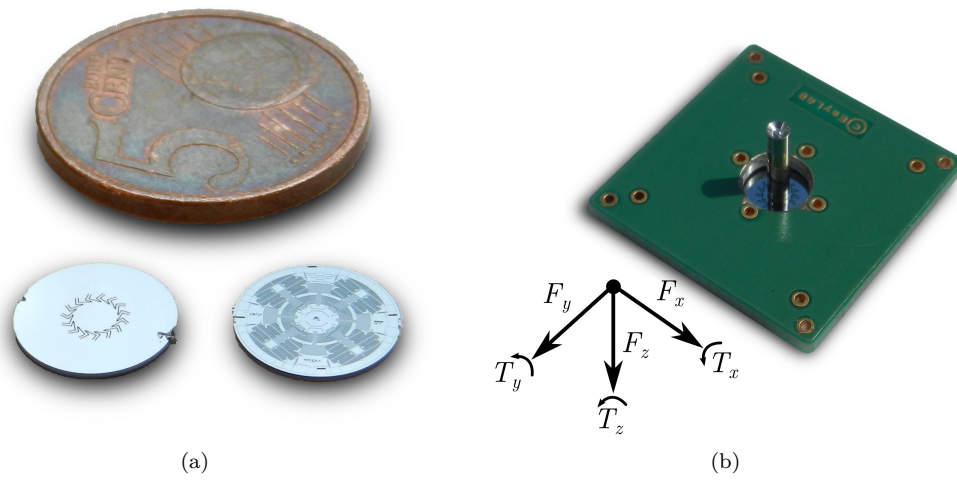


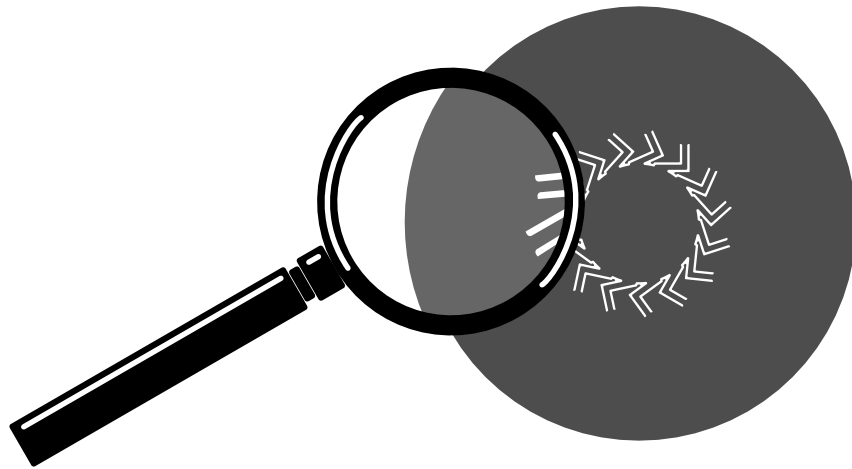
Figure 3.13: The sensor (a) and the sensor being mounted on the PCB (b).

### 3.4 Discussion and conclusion

This part described the design of a fabrication process, the theory behind the fabrication steps and the fabrication itself of a force/torque sensor made in one silicon-on-insulator wafer. The process and the mask design was designed as robust as possible to reduce the chance of problems during fabrication.

The wafer was oxidized and the oxide layer was patterned using photolithography and deep reactive ion etching (DRIE). The wafer was etched on both sides using DRIE. A release etch was performed to release the structures on the device layer from the handle layer. Some minor problems occurred: there were octafluorocyclobutane contaminants after the DRIE process and there were silicon contaminants after pushing the chips out of the wafer. Both contaminant problems were solvable by respectively piranha and  $O_2$  plasma cleaning and ultrasonic cleaning. Nevertheless, the latter problem can be solved by making the fixation points of the chips weaker in the mask.

---



---

*Author*  
Dennis Alveringh

*Supervised by*  
dr. ir. Remco Wiegerink  
Robert Brookhuis MSc

## 4.1 Introduction

This part describes the characterization of the sensor in three sections. First, the stage is mechanically characterized using white light interferometry. Then, the whole sensor is characterized for forces in shear and normal directions and torques around shear axes. This part ends with an overview of the measurement results and a comparison with the mathematical model. A calibration matrix is derived from the measurements and characterizes the linear behavior and crosstalk components of the sensor.

## 4.2 Characterization of the suspended core

This section describes the mechanical behavior of the suspended core. The obtained results may be used to correct the mathematical model.

### 4.2.1 Stiffness measurements

The stiffness of the suspended core in normal direction and the rotational stiffness around shear axes were measured.

#### Measurement setup

Stiffness measurements were done using a Polytec MSA 400 microsystem analyzer. It can measure out-of-plane movements with nanometer resolution using white light interferometry. White light interferometry is based on the interference of a beam that will be reflected via a mirror that is located specific distance and a beam that will be reflected at the sample. The parts of the sample that has the same distance as the distance to mirror will cause interference of the two beams. A camera records this and software interprets the interference pattern. The distance to the sample can be varied, this makes it possible to measure height differences of the sample. Figure 4.1 illustrates the working principle of white light interferometry.

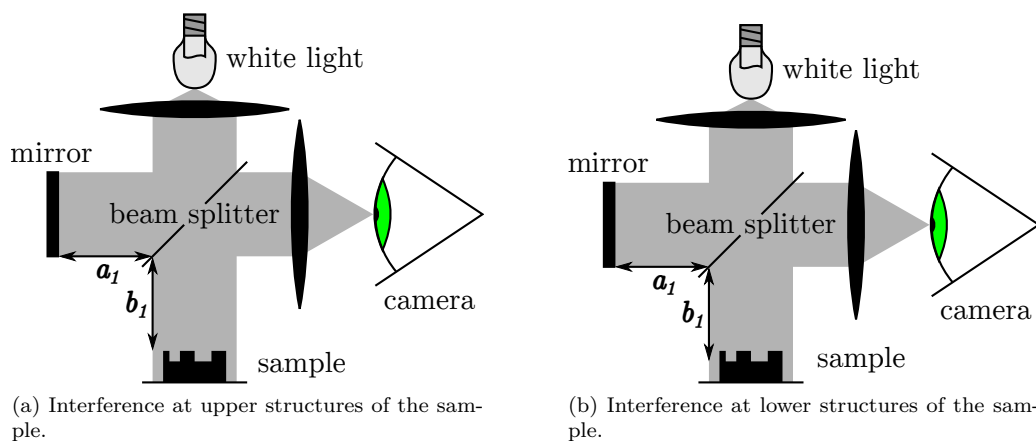


Figure 4.1: White light interferometry. Interferometry occurs when the distance to the sample  $b_1$  or  $b_2$  is equal to the distance to the mirror  $a_1$  or  $a_2$ . Software varies the distance to the sample and interprets the interference pattern.

Loads can be applied at the bottom of the sensor to measure the stiffness in normal direction. Using a pulley and a lever (the stylus), torques can be applied. Figure 4.2 shows the mechanical setup.

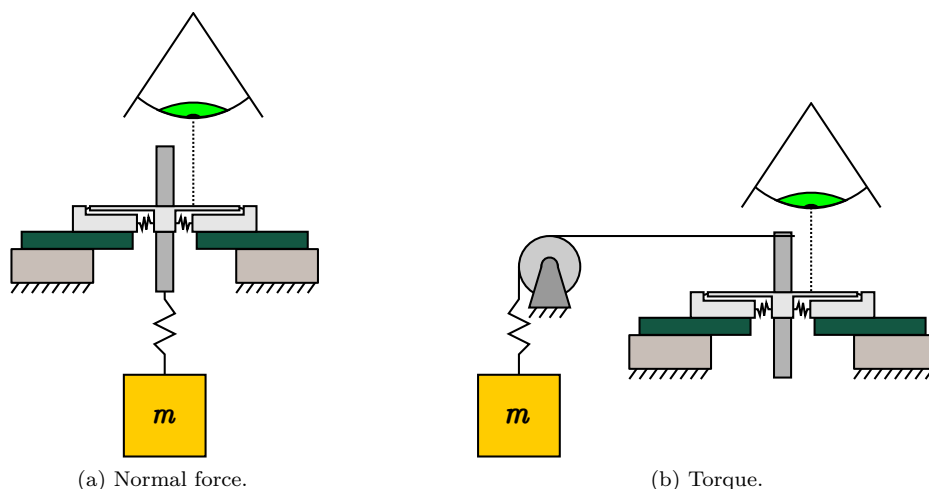


Figure 4.2: Measurement setup using white light interferometry for measuring the stiffness in normal direction and the rotational stiffness around shear direction.

## Measurement results

The stiffness in normal direction can be calculated from the measurement results in figure 4.3. This is approximately  $1.89 \cdot 10^6 \text{ N m}^{-1}$ .

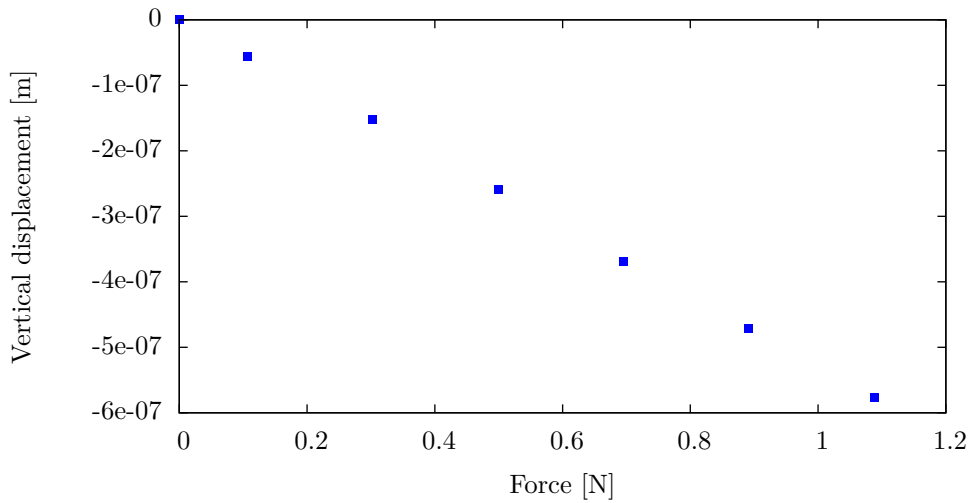


Figure 4.3: Measured displacement of the suspended core in normal direction with varying force.

The rotational stiffness was also measured. This value can be derived from figure 4.4 and is approximately  $1.6 \text{ N m rad}^{-1}$ .

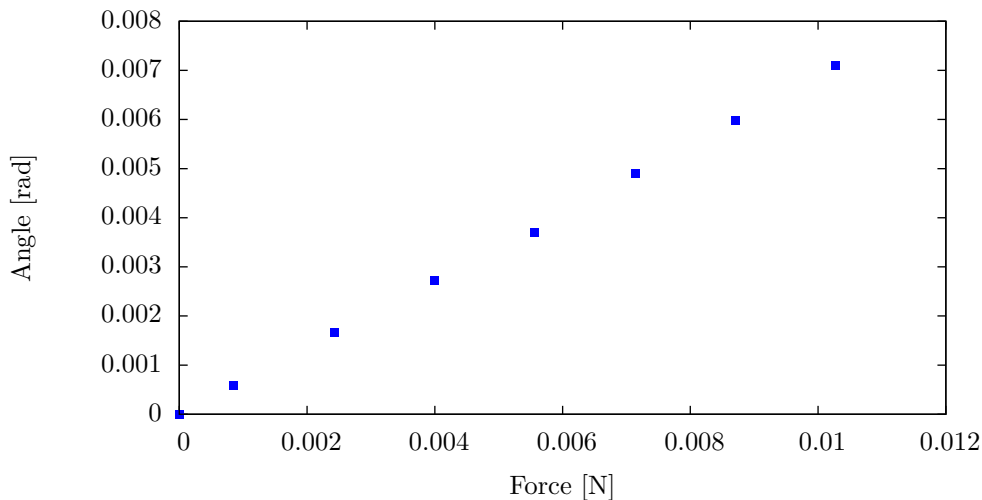


Figure 4.4: Measured angle of the suspended core with varying torque.

The suspended core seems very compliant ( $1.89 \cdot 10^6 \text{ N m}^{-1}$ ) in normal direction in comparison with the simulations ( $1.2 \cdot 10^7 \text{ N m}^{-1}$ ) and the mathematical model ( $1.9 \cdot 10^7 \text{ N m}^{-1}$ ). The suspended core seems also very compliant for rotations:  $1.6 \text{ N m rad}^{-1}$  was measured and  $41 \text{ N m rad}^{-1}$  was simulated. It can be concluded that something went wrong with the measurements, e.g.:

- a wrongly configured setting in the software multiplies the measurements with a factor;
- the reference point is not set correctly.

It can be recommended that reference measurements are done first to check the measurement setup.

### 4.2.2 Robustness test

A mechanical robustness test was done to obtain an impression how much load the sensor can handle. A normal load was applied directly on the mesa of the sensor. The load was increased with steps of 200 g. The sensor broke with 17 N of normal force.

### 4.3 Characterization of the sensor

The full sensor is characterized, the method and the results are reported in this section. First, the measurement setup will be described. Then, the measurement results will be given. Finally, the results and the method will be discussed.

#### 4.3.1 Measurement setup

The sensor's force behavior is characterized by applying loads in shear and normal direction. An extra stylus is mounted on the back of the chip to make sure pure shear forces were applied. Torques were measured by applying a load on the stylus at a defined distance from the sensor. The mechanical measurement setup for the three measurements are shown in figure 4.5.

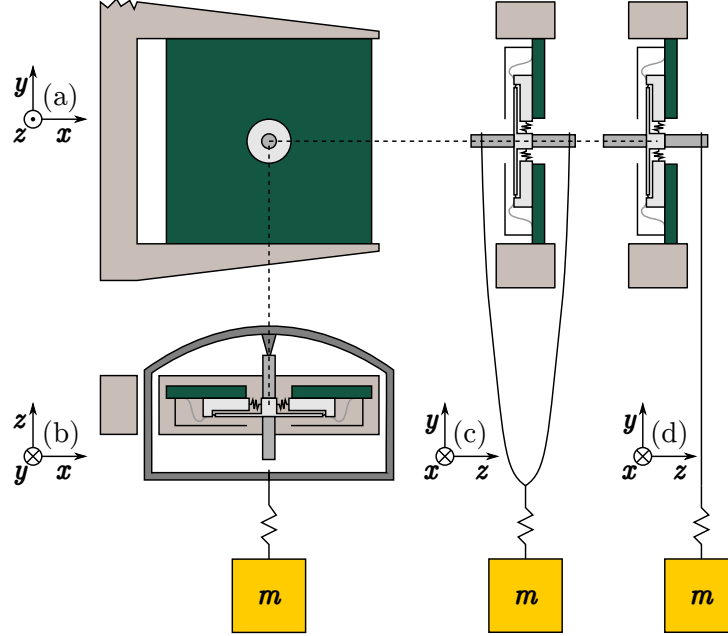


Figure 4.5: Measurement setup: (a) clamped assembled sensor, (b) measuring normal force, (c) measuring shear force, (d) measuring torque.

Measuring the (differential) change in capacitance is done using a custom built charge amplifier with a capacitor of 10 pF in the feedback loop. This makes the output of the charge amplifier as follows.

$$u_{out} = \frac{2\Delta C}{C_{fb}} u_{in} \quad (4.1)$$

With  $u_{out}$  the output voltage of the charge amplifier,  $u_{in}$  the input voltage,  $\Delta C$  the differential change in capacitance and  $C_{fb}$  the feedback capacitance of the charge amplifier. Two function generators (Agilent 33220A) with sine waves of 50 kHz with 180° phase shift are used for the input signals. The output of the charge amplifier is connected to a lock-in amplifier (Stanford Research Systems SR830) which was directly synchronized with one of the function generators. The measurement electronics are schematically drawn in figure 4.6.

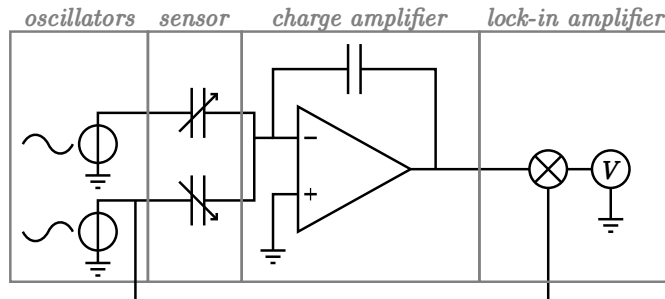


Figure 4.6: Electronic setup for differential measurements including two oscillators, a charge amplifier and a lock-in amplifier. Non-differential measurements are done using only one oscillator.

### 4.3.2 Measurement results

Shear force measurements (figure 4.7) show a very linear ( $>99\%$ ) differential change in capacitance with a sensitivity of  $38 \text{ fF N}^{-1}$ . The values are corrected for offset. The linear model is corrected for positive and negative shear forces with a factor of 0.88 and 0.78 respectively.

Normal force measurements (figure 4.8) show a high sensitivity of  $550 \text{ fF N}^{-1}$  in the linear region. The values are corrected for offset. A corrected model using the fourth order Maclaurin expansion from the design section is fit through the measured values. The model is corrected for the distance between the parallel plates, the overlapping area of the plates and the stiffness with factors 0.45, 0.46 and 0.45 respectively.

The mentioned correction factors are necessary for the compensation of non-ideal effects in the mechanics, electrostatics or fabrication process. The distance between the capacitor structures may be smaller or larger than expected due to the etching process for example.

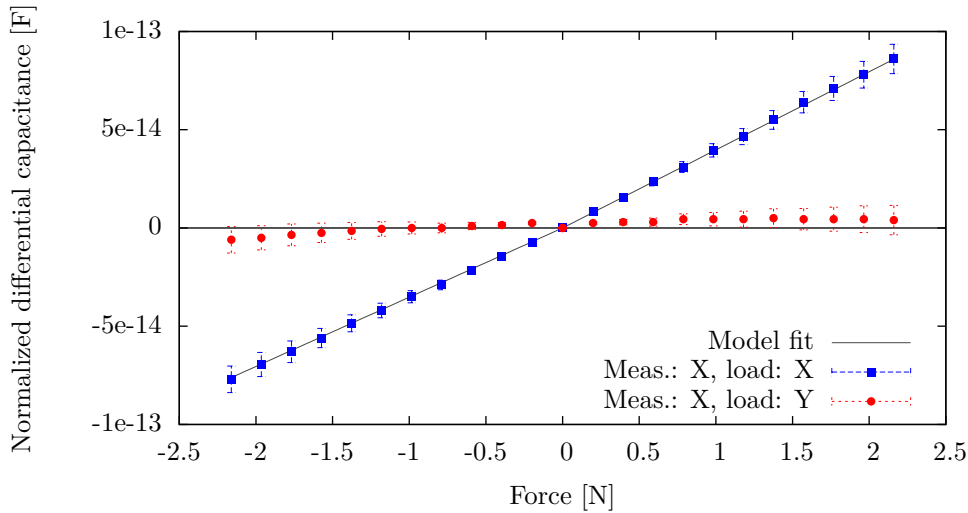


Figure 4.7: Shear measurements.

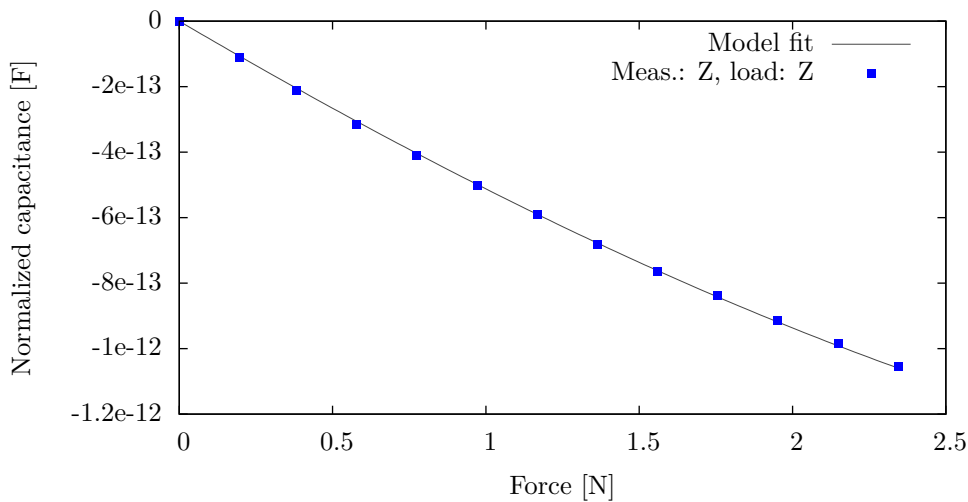


Figure 4.8: Normal measurements.

In figure 4.9 torque measurements around a shear axis are shown. The fitted model is based on a differential version of the normal force model.

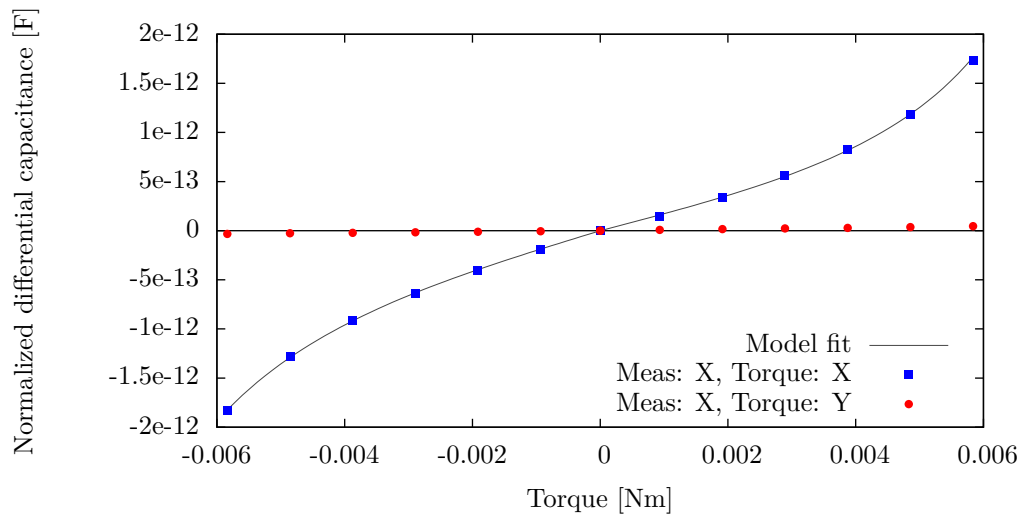


Figure 4.9: Torque measurements.

## 4.4 Discussion and conclusion

This section describes the problems that occurred during fabrication and measurements. The calibration matrix is derived from the measurement results and describes the linear behavior and crosstalk components of the sensor. This section ends with a summary of the performance.

### 4.4.1 Stiffness measurements

Due to an unknown error, the stiffness measurements were useless. New measurements should be done and care has to be taken with the measurement setup and the configuration of the software.

### 4.4.2 Crosstalk between shear force measurements

A slight crosstalk is observed when a shear force in orthogonal direction with respect to the measured direction is applied, caused by misalignment in the measurement setup (figure 4.7). The error bars in figure 4.7 represent misalignments from  $-5^\circ$  until  $5^\circ$ .

### 4.4.3 Crosstalk between torque and shear force measurements

Crosstalk occurs in the shear structures when a torque is applied around x-axis or y-axis. The rotation of the mesa leads to a translation of the shear structures as is illustrated in figure 4.10.

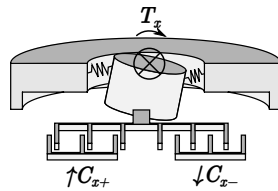


Figure 4.10: Crosstalk in the shear structures as consequence of an applied torque around x-axis or y-axis.

The crosstalk component is measured and its results are plotted in figure 4.11. It can be concluded that the crosstalk measurements for forces applied at a distance of 1 cm of the sensor is in the same order of magnitude as for shear forces.

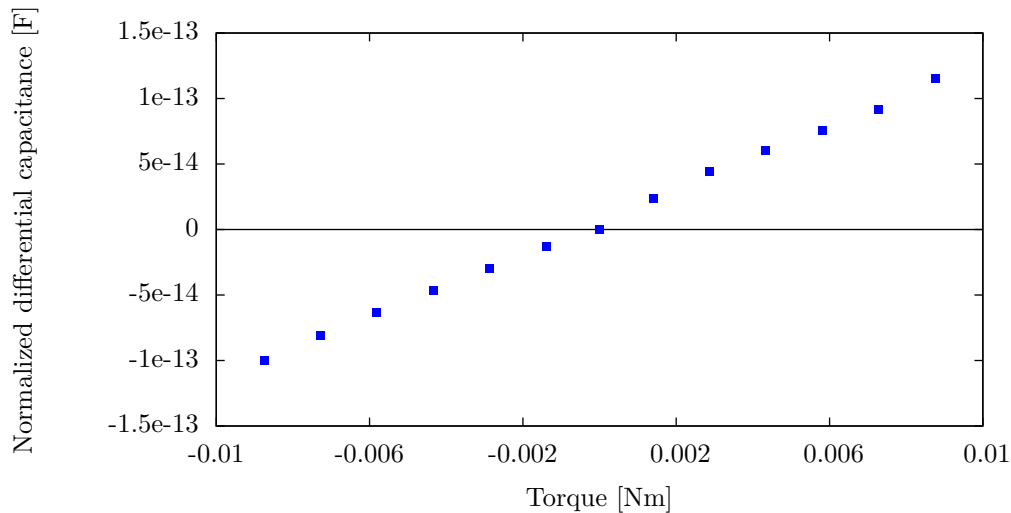


Figure 4.11: Differential capacitance measurements of the shear structures when a torque around x-axis is applied.

### 4.4.4 Measuring the sixth degree of freedom

The rotation around the normal axis was not characterized due to the time restrictions in building a measurement setup. The sensor has support for measuring this direction, so this direction may be characterized in the future.

#### 4.4.5 Calibration

There can be compensated for the crosstalk component using torque measurements with the parallel plate structures. Calibration matrix  $\mathbf{K}$  is a six by eight matrix consisting of the inverted elements  $\beta^{-1}$  and mentioned crosstalk components  $\alpha^{-1}$ . Calibration matrix  $\mathbf{K}$  is only valid for small forces and torques in the linear region. Expressions for the elements  $\beta_x^{-1}$  and  $\beta_z^{-1}$  were already given in equations 2.44 and 2.42.

$$\mathbf{K} = \begin{bmatrix} \beta_x^{-1} & \beta_x^{-1} & 0 & 0 & -\alpha_x^{-1} & \alpha_x^{-1} & -\alpha_x^{-1} & \alpha_x^{-1} \\ 0 & 0 & \beta_y^{-1} & \beta_y^{-1} & -\alpha_y^{-1} & \alpha_y^{-1} & -\alpha_y^{-1} & \alpha_y^{-1} \\ 0 & 0 & 0 & 0 & \beta_z^{-1} & \beta_z^{-1} & \beta_z^{-1} & \beta_z^{-1} \\ 0 & 0 & 0 & 0 & \beta_\phi^{-1} & \beta_\phi^{-1} & -\beta_\phi^{-1} & -\beta_\phi^{-1} \\ 0 & 0 & 0 & 0 & \beta_\theta^{-1} & -\beta_\theta^{-1} & \beta_\theta^{-1} & -\beta_\theta^{-1} \\ \text{N/A} & \text{N/A} \end{bmatrix} \quad (4.2)$$

Characterization has been done and the crosstalk components are defined. The elements of calibration matrix  $\mathbf{K}$  can be calculated from the measurement results and are enumerated in figure 4.1.

Table 4.1: Calibration matrix elements.

Element	Value	Element	Value
$\beta_x^{-1}$	$2.6 \cdot 10^{13}$	$\alpha_x^{-1}$	$1.7 \cdot 10^{12}$
$\beta_y^{-1}$	$2.6 \cdot 10^{13}$	$\alpha_y^{-1}$	$1.7 \cdot 10^{12}$
$\beta_z^{-1}$	$2.2 \cdot 10^{12}$	$\alpha_z^{-1}$	0
$\beta_\phi^{-1}$	$5.3 \cdot 10^9$	$\alpha_\phi^{-1}$	0
$\beta_\theta^{-1}$	$5.3 \cdot 10^9$	$\alpha_\theta^{-1}$	0

#### 4.4.6 Performance

Table 4.2 shows the measured performance of the sensor.

Table 4.2: Summary of the sensor performance.

Quantity	Range	Sensitivity of linear region
$F_x$	2.16 N	38 fF N <sup>-1</sup>
$F_y$	2.16 N	38 fF N <sup>-1</sup>
$F_z$	2.34 N	550 fF N <sup>-1</sup>
$T_x$	5.84 N mm	23 nF N <sup>-1</sup> m <sup>-1</sup>
$T_y$	5.84 N mm	23 nF N <sup>-1</sup> m <sup>-1</sup>
$T_z$	N/A	N/A

## Conclusion

A large range five degrees of freedom force/torque sensor is designed, realized and characterized. It has a minimum force range of 2 N in shear and normal direction and a torque range of more than 6 N mm. The sensor shows in shear and normal direction competing sensitivities of 38 fF N<sup>-1</sup> and 550 fF N<sup>-1</sup> respectively. The proposed sensor is therefore suitable for biomechanical and robotic applications. The fabrication takes only two masks, making it a cheap and relatively fast process. The fabrication is also reproducible, making it an interesting process for mass production. The rotation around the normal axis can be measured by the sensor, but is not yet characterized. Future work will focus on further characterization of this sixth degree of freedom, mechanical compensation for the crosstalk component and increasing the range and sensitivity.

All detailed conclusions are available in the individual parts of this documentation.

## References

- [1] D. Alveringh, R.A. Brookhuis, R.J. Wiegerink, G.J.M. Krijnen, M.J. de Boer, and P.E. Veltink. A large range multi-axis capacitive force/torque sensor realized in a single soi wafer.
- [2] Lucia Beccai, Stefano Roccella, Alberto Arena, Francesco Valvo, Pietro Valdastri, Arianna Menciassi, Maria Chiara Carrozza, and Paolo Dario. Design and fabrication of a hybrid silicon three-axial force sensor for biomechanical applications. *Sensors and Actuators A: Physical*, 120(2):370–382, 2005.
- [3] D. J. Bell, T. J. Lu, N. A. Fleck, and S. M. Spearing. MEMS actuators and sensors: observations on their performance and selection for purpose. *Journal of Micromechanics and Microengineering*, 15(7):S153, 2005.
- [4] Berkeley Microfabrication Laboratory. Lab manual of Hfvapor (Idonus HF VPE-100 / 150). url-<http://nanolab.berkeley.edu/labmanual/chap7/7.4hfvapor.pdf>.
- [5] F. Beyeler, S. Muntwyler, and B. . Nelson. A six-axis MEMS force–torque sensor with micro-Newton and nano-Newtonmeter resolution. *Journal of Microelectromechanical Systems*, 18(2):433–441, 2009.
- [6] R. A. Brookhuis, T. S. J. Lammerink, R. J. Wiegerink, M. J. de Boer, and M. C. Elwenspoek. 3D Force sensor for Biomechanical applications. *Sensors and Actuators A: Physical*, 2012.
- [7] RA Brookhuis, RJ Wiegerink, TSJ Lammerink, MJ de Boer, K Ma, and MC Elwenspoek. Scalable six-axis force-torque sensor with a large range for biomechanical applications. In *Micro Electro Mechanical Systems (MEMS), 2012 IEEE 25th International Conference on*, pages 595–598. IEEE, 2012.
- [8] Jörg Butterfaß, Markus Grebenstein, Hong Liu, and Gerd Hirzinger. Dlr-hand ii: Next generation of a dextrous robot hand. In *Robotics and Automation, 2001. Proceedings 2001 ICRA. IEEE International Conference on*, volume 1, pages 109–114. IEEE, 2001.
- [9] T. A. Chase and R. C. Luo. A Flexible Capacitive Normal/Shear Tactile Force Sensor. In *Proceedings of the 25th European Solid State Device Research Conference*, pages 351–355. IEEE, 1995.
- [10] H. K. Chu, J. K. Mills, and W. L. Cleghorn. Design of a high sensitivity capacitive force sensor. In *7th IEEE Conference on Nanotechnology*, pages 29–33. IEEE, 2007.
- [11] Bruce E Deal and AS Grove. General relationship for the thermal oxidation of silicon. *Journal of Applied Physics*, 36(12):3770–3778, 1965.
- [12] A Del Campo and C Greiner. Su-8: a photoresist for high-aspect-ratio and 3d submicron lithography. *Journal of Micromechanics and Microengineering*, 17(6):R81, 2007.
- [13] J. A. Dobrzynska and M. A. M. Gijs. Capacitive flexible force sensor. *Procedia Engineering*, 5: 404–407, 2010.
- [14] Richard Phillips Feynman, Robert B Leighton, and Matthew Sands. *The Feynman lectures on physics, vol. 2: Mainly electromagnetism and matter*. Addison-Wesley, 1979.
- [15] MESA+ Institute for nanotechnology. Equipment Database. <http://www.mesacrl.utwente.nl/MICMEC/tts/viewdatabase/findequipment.php>.

- [16] Sami Franssila. *Introduction to Microfabrication*. John Wiley & Sons, Ltd, second edition, 2010.
- [17] Fujifilm. OiR 907 Series Technical Product Information. <http://www.mesacrl.utwente.nl/mis/generalinfo/downloads/usermanuals/170/OiR907%20serie.pdf>.
- [18] R. C. Hibbeler. *Mechanics of Materials*. Prentice Hall, 6th edition, 2005.
- [19] Kazuo Hirai, Masato Hirose, Yuji Haikawa, and Toru Takenaka. The development of honda humanoid robot. In *Robotics and Automation, 1998. Proceedings. 1998 IEEE International Conference on*, volume 2, pages 1321–1326. IEEE, 1998.
- [20] HTE Labs. SiO<sub>2</sub> Color Chart for thermally grown silicon dioxide). url-[http://www.htelabs.com/apnotes/sio2\\_color\\_chart\\_thermal\\_silicon\\_dioxide.htm](http://www.htelabs.com/apnotes/sio2_color_chart_thermal_silicon_dioxide.htm).
- [21] E. S. Hwang, J. Seo, and Y. J. Kim. A polymer-based flexible tactile sensor for both normal and shear load detections and its application for robotics. *Journal of Microelectromechanical Systems*, 16(3):556–563, 2007.
- [22] HV Jansen, NR Tas, and JW Berenschot. *Encyclopedia of Nanoscience and Nanotechnology: MEMS-Based Nanotechnology*, volume 5. 2004.
- [23] HV Jansen, MJ De Boer, S Unnikrishnan, MC Louwense, and MC Elwenspoek. Black silicon method X: a review on high speed and selective plasma etching of silicon with profile control: an in-depth comparison between Bosch and cryostat DRIE processes as a roadmap to next generation equipment. *Journal of micromechanics and microengineering*, 19(3):033001, 2009.
- [24] H. K. Lee, J. Chung, S. I. Chang, and E. Yoon. Normal and shear force measurement using a flexible polymer tactile sensor with embedded multiple capacitors. *Journal of Microelectromechanical Systems*, 17(4):934–942, 2008.
- [25] Marcia W Legro, Gayle Reiber, Michael del Aguila, Megan J Ajax, David A Boone, Jerrie A Larsen, Douglas G Smith, and Bruce Sangeorzan. Issues of importance reported by persons with lower limb amputations and prostheses. *Journal of rehabilitation research and development*, 36(3), 1999.
- [26] Y. C. Liu, C. M. Sun, L. Y. Lin, M. H. Tsai, and W. Fang. Development of a CMOS-Based Capacitive Tactile Sensor With Adjustable Sensing Range and Sensitivity Using Polymer Fill-In. *Journal of Microelectromechanical Systems*, 20(1):119–127, 2011.
- [27] J. C. Lötters, W. Olthuis, P. H. Veltink, and P. Bergveld. The mechanical properties of the rubber elastic polymer polydimethylsiloxane for sensor applications. *Journal of Micromechanics and Microengineering*, 7(3):145, 1999.
- [28] Arthur FT Mak, Ming Zhang, and David A Boone. State-of-the-art research in lower-limb prosthetic biomechanics-socket interface. *Journal of rehabilitation research and development*, 38(2):161–173, 2001.
- [29] HB Muhammad, CM Oddo, L Beccai, C Recchiuto, CJ Anthony, MJ Adams, MC Carrozza, DWL Hukins, and MCL Ward. Development of a bioinspired MEMS based capacitive tactile sensor for a robotic finger. *Sensors and Actuators A: Physical*, 165(2):221–229, 2011.
- [30] K. Noda, K. Hoshino, K. Matsumoto, and I. Shimoyama. A shear stress sensor for tactile sensing with the piezoresistive cantilever standing in elastic material. *Sensors and Actuators A: Physical*, 127(2):295–301, 2006.
- [31] Erik Oberg, Franklin D. Jones, Holbrook L. Horton, and Henry H. Ryffel. *Machinery's Handbook*. Industrial Press, 27th edition, 2004.
- [32] CT Pan, H Yang, SC Shen, MC Chou, and HP Chou. A low-temperature wafer bonding technique using patternable materials. *Journal of Micromechanics and Microengineering*, 12(5):611, 2002.
- [33] Robert Puers. Capacitive sensors: when and how to use them. *Sensors and Actuators A: Physical*, 37:93–105, 1993.
- [34] Herman Soemers. *Design principles for precision mechanisms*. 2010.
- [35] Yu Sun, Bradley J Nelson, David P Potasek, and Eniko Enikov. A bulk microfabricated multi-axis capacitive cellular force sensor using transverse comb drives. *Journal of Micromechanics and Microengineering*, 12(6):832, 2002.

- 
- [36] Y. Takei, K. Noda, T. Kawai, T. Tachimura, Y. Toyama, T. Ohmori, K. Matsumoto, and I. Shimoyama. Triaxial force sensor for lingual motion sensing. In *IEEE 25th International Conference on Micro Electro Mechanical Systems (MEMS)*, pages 128–131. IEEE, 2012.
- [37] Niels Tas, Tonny Sonnenberg, Henri Jansen, Rob Legtenberg, and Miko Elwenspoek. Stiction in surface micromachining. *Journal of Micromechanics and Microengineering*, 6(4):385, 1996.
- [38] A. Tibrewala, A. Phataralaoha, and S. Büttgenbach. Simulation, fabrication and characterization of a 3D piezoresistive force sensor. *Sensors and Actuators A: Physical*, 147(2):430–435, 2008.
- [39] Peter H Veltink, Henk Kortier, and H Martin Schepers. Sensing power transfer between the human body and the environment. *Biomedical Engineering, IEEE Transactions on*, 56(6):1711–1718, 2009.
- [40] W. Wang, Y. Zhao, and Q. Lin. An integrated MEMS tactile tri-axial micro-force probe sensor for Minimally Invasive Surgery. In *IEEE International Conference on Nano/Molecular Medicine and Engineering*, pages 71–76. IEEE, 2009.
- [41] Zhixin Wang. *Polydimethylsiloxane Mechanical Properties Measured by Macroscopic Compression and Nanoindentation Techniques*. PhD thesis, University of South Florida, 2011.
- [42] R. Wiegerink, R. Zwijze, G. Krijnen, T. Lammerink, and M. Elwenspoek. Quasi-monolithic silicon load cell for loads up to 1000 kg with insensitivity to non-homogeneous load distributions. *Sensors and Actuators A: Physical*, 80(2):189–196, 2000.
- [43] A. Wisitsoraat, V. Patthanasetakul, T. Lomas, and A. Tuantranont. Low cost thin film based piezoresistive MEMS tactile sensor. *Sensors and Actuators A: Physical*, 139(1):17–22, 2007.

## List of Figures

1	Power measurements of the human hand using force sensors, accelerometers and gyroscopes. The power $P$ in one element is equal to $\vec{F} \cdot \vec{v} + \vec{T} \cdot \vec{\omega}$ . . . . .	2
1.1	Common operating principle of MEMS force sensors. . . . .	5
1.2	MEMS actuators and sensors: observations on their performance and selection for purpose from Bell et al. . . . .	5
1.3	The quasi-monolithic silicon load cell for loads up to 1000 kg with insensitivity to non-homogeneous load distributions from Wiegerink et al. . . . .	7
1.4	The 3D force sensor for biomechanical applications from Brookhuis et al. . . . .	7
1.5	A six-axis MEMS force-torque sensor with micro-Newton and nano-Newtonmeter resolution from Beyeler et al. . . . .	9
1.6	Design of a high sensitivity capacitive force sensor from Chu et al. . . . .	11
1.7	Development of a bioinspired MEMS based capacitive tactile sensor for a robotic finger from Muhammad et al. . . . .	11
1.8	The mechanical properties of the rubber elastic polymer polydimethylsiloxane for sensor applications from Lötters et al. . . . .	13
1.9	Polydimethylsiloxane Mechanical Properties Measured by Macroscopic Compression and Nanoindentation Techniques from Wang . . . . .	13
1.10	A low-temperature wafer bonding technique using patternable materials from Pan et al. . . . .	15
1.11	A normal and shear force measurement using a flexible polymer tactile sensor with embedded multiple capacitors from Lee et al. . . . .	15
1.12	Capacitive flexible force sensor from Dobrzynska and Gijs. . . . .	17
1.13	Development of a CMOS-Based Capacitive Tactile Sensor With Adjustable Sensing Range and Sensitivity Using Polymer Fill-In from Liu et al. . . . .	17
1.14	Design and fabrication of a hybrid silicon three-axial force sensor for biomechanical applications from Beccai et al. . . . .	19
1.15	A Low cost thin film based piezoresistive MEMS tactile sensor from Wisitsoraat et al. . . . .	19
1.16	Simulation, fabrication and characterization of a 3D piezoresistive force sensor from Tibrewala et al. . . . .	21
1.17	An integrated MEMS tactile tri-axial micro-force probe sensor for Minimally Invasive Surgery from Wang et al. . . . .	21
1.18	A polymer-based flexible tactile sensor for both normal and shear load detections and its application for robotics from Hwang et al. . . . .	23
1.19	A triaxial force sensor for lingual motion sensing from Takei et al. . . . .	23
2.1	FEM simulation of the bottom supported springs of SU-8 concept. The colors represent the von Mises stress in Pa. . . . .	27
2.2	SU-8 pillars in holes: (a) a silicon wafer, (b) etching holes in the wafer with small bumps at both sides of the chip, (c) bond the wafer on top of another silicon wafer, (d) fill the structure with SU-8, (e) expose SU-8 through the holes of the top wafer, (f) develop and rinse, (g) saw or etch the wafer in chips. . . . .	28
2.3	FEM simulation of the bottom supported springs of PDMS concept. The colors represent the von Mises stress in Pa. . . . .	29

2.4	PDMS sensor fabrication: (a) a silicon wafer (b) application of one solid layer of PDMS (c) bonding or growing another layer of silicon . . . . .	29
2.5	FEM simulation of the edge supported springs of silicon concept. The colors represent the von Mises stress in Pa. . . . .	29
2.6	Edge supported sensor fabrication: (a) a silicon-on-insulator wafer (b) etch of the springs in the upper layer (c) etch of the sensing structures in the device layer . . . . .	30
2.7	Sensing structures for shear forces and torques around the normal axis. . . . .	31
2.8	Sensing structures for normal forces and the torques around the shear axes. . . . .	31
2.9	Principle of operation for shear forces. . . . .	32
2.10	Principle of operation for normal forces and torques. . . . .	32
2.11	Guided beam with dimensions. . . . .	33
2.12	Beam with free end with the dimensions. . . . .	34
2.13	A six degrees of freedom stage using folded sheet springs. The combination of three folded sheet springs is called a spring triplet. . . . .	34
2.14	Handle layer with the point symmetric v-shaped spring system and the parameters of each spring. . . . .	35
2.15	Design of the device layer with declaration of all sensing capacitors. . . . .	36
2.16	A parallel plate capacitor with very large overlapping area compared to the distance between the plates. . . . .	36
2.17	The model with boundary conditions. . . . .	39
2.18	Deformation analysis using FEM. . . . .	40
2.19	Stress analysis using FEM for a shear force of 10 N pointed to the right. . . . .	40
2.20	Transmission (2) from mesa (1) to comb-structures (4). There are bumps (3) to prevent snapping of the fingers due to overloading. . . . .	41
2.21	Electrical design of the comb-structures. . . . .	42
2.22	Optimization of the finger distances: choosing $d_0$ the maximum of the function will consequent in the highest capacitance. . . . .	42
2.23	Capacitor plate (2) is directly coupled with mesa (1). Wires (4) connect the capacitor plate to the bondpand (5) and have no effect on the mechanics due to there folds. There are bumps (3) to prevent snapping of the plates due to shear overloading. . . . .	43
2.24	Parallel plate structure simulations. The capacitance of the situation with one perforated plate (a) performs 11 % lower compared to the situation with two solid parallel plates (b). . . . .	43
2.25	Paths in the structures that can be modeled as doubly clamped beams (a) or beams with a free end (b). . . . .	44
3.1	Masks of the six degrees of freedom force and torque sensor for a single chip. White parts will be etched. . . . .	49
3.2	Impression of the location of the chips and how they will be borken out of the wafer. . . . .	50
3.3	Deformation due to stress for a mask with photoresist and a mask with silicon dioxide. . . . .	51
3.4	Fabrication process with each step explained in table 3.2. . . . .	52
3.5	Oxide thickness versus the time of oxidation for dry oxidation and wet oxidation respectively. Source: [11]. . . . .	52
3.6	Layer thickness versus spin speed of OiR 907 series positive resist. Source: [17]. . . . .	53
3.7	Schematic view of a DRIE system with the most important parameters that can be changed to achieve a certain etch rate, selectivity and anisotropy. . . . .	53
3.8	Resist without (a) and with (b) hard bake. Photos are taken from a dummy wafer without hard bake and a SOI-wafer with hard bake. . . . .	55
3.9	Inspection of etching performance. . . . .	56
3.10	Octafluorocyclobutane contamination after DRIE and piranha cleaning. . . . .	56
3.11	Oxide left after wet etching for the 7 $\mu\text{m}$ wide finger structures. . . . .	57
3.12	SEM closeups of the device. . . . .	57
3.13	The sensor (a) and the sensor being mounted on the PCB (b). . . . .	58
4.1	White light interferometry. Inteferometry occurs when the distance to the sample $b_1$ or $b_2$ is equal to the distance to the mirror $a_1$ or $a_2$ . Software varyies the distance to the samle and interprets the interference pattern. . . . .	63
4.2	Measurement setup using white light interferometry for measuring the stiffness in normal direction and the rotational stiffness around shear direction. . . . .	63
4.3	Measured displacement of the suspended core in normal direction with varying force. . . . .	64
4.4	Measured angle of the suspended core with varying torque. . . . .	64

---

4.5	Measurement setup: (a) clamped assembled sensor, (b) measuring normal force, (c) measuring shear force, (d) measuring torque. . . . .	65
4.6	Electronic setup for differential measurements including two oscillators, a charge amplifier and a lock-in amplifier. Non-differential measurements are done using only one oscillator. . . . .	65
4.7	Shear measurements. . . . .	66
4.8	Normal measurements. . . . .	66
4.9	Torque measurements. . . . .	67
4.10	Crosstalk in the shear structures as consequence of an applied torque around x-axis or y-axis. . . . .	68
4.11	Differential capacitance measurements of the shear structures when a torque around x-axis is applied. . . . .	68



## Symbols, quantities and constants

Symbols for quantities and units are quite internationally standardized, but there are still countries that use different systems. Besides, there are symbols that represent different quantities. These pages should make clear all quantities and their corresponding symbols and units used in this documentation.

The choice for the symbols and units in this documentation is based on three considerations, not necessarily in the following order:

- the International System of Units;
- the symbols used in the Netherlands;
- attempt to avoid duplicate quantities per symbol.

The quantities with its symbols and units in table A.1 are used in this documentation. Alternative cases will be made clear in the text.

Table A.1: Quantities with its symbols and units used in this documentation

Quantity	Symbol	Unit	SI base units
Time	$f$	s	s
Frequency	$f$	Hz	$s^{-1}$
Energy	$E$	J	$\text{kg m}^2 \text{s}^{-2}$
Power	$P$	W	$\text{kg m}^2 \text{s}^{-3}$
Velocity	$v$	$\text{m s}^{-1}$	$\text{m s}^{-1}$
Force	$F$	N	$\text{kg m s}^{-2}$
Distributed force	$q$	$\text{N m}^{-1}$	$\text{kg s}^{-2}$
Angular velocity	$\omega$	$\text{rad s}^{-1}$	$\text{rad s}^{-1}$
Stress	$\sigma$	Pa	$\text{kg s}^{-2} \text{m}^{-1}$
Strain	$\varepsilon$	1	1
Mass	$m$	kg	kg
Stiffness	$k$	$\text{N m}^{-1}$	$\text{kg s}^{-2}$
Rotational stiffness	$c$	$\text{N m rad}^{-1}$	$\text{kg m}^2 \text{s}^{-2} \text{rad}^{-1}$
Mechanical damping	$\zeta$	$\text{kg s}^{-1}$	$\text{kg s}^{-1}$
Electric voltage	$u$	V	$\text{kg m}^2 \text{A}^{-1} \text{s}^{-3}$
Electric potential	$V$	V	$\text{kg m}^2 \text{A}^{-1} \text{s}^{-3}$
Electric current	$i$	A	A
Electric current density	$J$	$\text{A m}^{-2}$	$\text{A m}^{-2}$
Electric resistance	$R$	$\Omega$	$\text{kg m}^2 \text{A}^{-1} \text{s}^{-3} \text{A}^{-1}$
Electric conductance	$G$	S	$\text{A s}^3 \text{A kg}^{-1} \text{m}^{-2}$
Electric impedance	$Z$	$\Omega$	$\text{kg m}^2 \text{A}^{-1} \text{s}^{-3} \text{A}^{-1}$
Electric admittance	$Y$	S	$\text{A s}^3 \text{A kg}^{-1} \text{m}^{-2}$
Electric capacitance	$C$	F	$\text{s}^4 \text{A}^2 \text{kg}^{-1} \text{m}^{-2}$
Electric inductance	$L$	H	$\text{kg m}^2 \text{s}^{-2} \text{A}^{-2}$
Magnetic field	$B$	T	$\text{kg m s}^{-3} \text{A}^{-1}$
Electric field	$E$	$\text{V m}^{-1}$	$\text{rad s}^{-1}$
Absolute magnetic permeability	$\mu$	rad	$\text{kg m s}^{-2} \text{A}^{-2}$
Absolute electric permittivity	$\varepsilon$	$\text{F m}^{-1}$	$\text{s}^4 \text{A}^2 \text{kg}^{-1} \text{m}^{-3}$
Charge	$q$	C	A s
Fluid velocity	$U$	$\text{m s}^{-1}$	$\text{m s}^{-1}$
Dynamic viscosity	$\mu$	Pa s	$\text{kg s}^{-1} \text{m}^{-1}$
Reynolds number	$Re$	1	1
Density	$\rho$	$\text{kg m}^{-3}$	$\text{kg m}^{-3}$
x-coordinate	$x$	m	m
y-coordinate	$y$	m	m
z-coordinate	$z$	m	m
Distance	$d$	m	m
Length	$L$	m	m
Width	$W$	m	m
Thickness	$T$	m	m
Radius	$r$	m	m
Diameter	$D$	m	m
Area (running variable)	$a$	$\text{m}^2$	$\text{m}^2$
Area (fixed)	$A$	$\text{m}^2$	$\text{m}^2$
Angle	$\Theta$	rad	rad

The constants in table A.2 are used in this documentation. Note the use of  $j$  as imaginary unit for complex numbers, commonly used in electrical engineering, control engineering and signal processing.

Table A.2: Constants in nature

Constant	Symbol	Value
Imaginary unit	$j$	$\sqrt{-1}$
Magnetic constant	$\mu_0$	$1.256\,637\,061\,4 \cdot 10^{-6} \text{ H m}^{-1}$
Relative magnetic permeability of vacuum	$\mu_r$	$1 \text{ H m}^{-1}$
Dielectric constant	$\varepsilon_0$	$8.854\,187\,817\,620 \cdot 10^{-12} \text{ F m}^{-1}$
Relative electric permittivity of vacuum	$\varepsilon_r$	$1 \text{ F m}^{-1}$
Standard gravity	$g$	$9.81 \text{ m s}^{-2}$
Gravitational constant	$G$	$6.673\,84 \cdot 10^{-11} \text{ N m}^2 \text{ kg}^{-2}$
Electrical resistivity of copper	$\rho_{Cu}$	$1.68 \cdot 10^{-8} \Omega \text{ m}$
$e$	$e$	2.718 281 828
$\pi$	$\pi$	3.141 592 653

Because the operators in table A.3 are sometimes interpreted in different ways in mathematics and physics, table A.3 should make clear how these operators are used in this documentation.

Table A.3: Non-obvious operators

Operator name	Definition
Imaginary unit	$j = \sqrt{-1}$
Natural logarithm	$\ln(x)$
Logarithm to base $b$	$\log_b(x) = \frac{\ln(x)}{\ln(b)}$
Logarithm to base 10	$\log(x) = \log_{10}(x)$
Vector	$\vec{E} = \begin{bmatrix} E_x \\ E_y \\ E_z \end{bmatrix}$
Absolute value of vector	$E =  \vec{E} $

*B*

**Paper for publication**

This appendix contains the original paper for publication in a journal.

# A Large Range Multi-Axis Capacitive Force/Torque Sensor Realized in a Single SOI Wafer

*D. Alveringh, R.A. Brookhuis, R.J. Wiegerink, G.J.M. Krijnen, M.J. de Boer and P.E. Veltink*

Transducer Science and Technology Group, MESA+ Institute for Nanotechnology, University of Twente,  
P.O. Box 217, 7500 AE Enschede, The Netherlands

**Abstract**—A MEMS-based silicon capacitive force/torque sensor is designed and realized to be used for biomechanical applications and robotics. The sensor is able to measure the forces in three directions and two torques using four parallel capacitor plates and four comb-structures. Novel spring and lever structures are designed to separate the different force components and minimize crosstalk. The fabrication process is based on deep reactive ion etching on both sides of a single silicon-on-insulator wafer and uses only two masks making it very suitable for mass production. The sensor has a force range of 2 N in shear and normal direction and a torque range of more than 6 Nmm. It has a high sensitivity of  $38 \text{ fF N}^{-1}$  and  $550 \text{ fF N}^{-1}$  in shear and normal direction respectively. A calibration matrix is derived from the sensor's measured characteristics.

## I. INTRODUCTION

MINIATURIZED multi-axis force/torque sensors are widely used in medical applications, tactile sensing and robotics. Many prostheses, for example, require safe and comfortable interaction with people who underwent amputation of a part of a limb. Bad fitting between the socket of the prosthesis and the residual limb may cause pain and even damage to the underlying blood vessels [1], [2]. Measuring the shear forces and normal forces between the socket and the residual limb is possible with multiple small force sensors. The prosthesis can use this information to adjust the shape of the socket, making the load distribution as comfortable and healthy as possible.

Other applications are in the field of characterization of the human body. For example, power measurements of the human hand are important for rehabilitation purposes or the optimization of the endurance of athletes [3]. These power measurements can be done with force/torque sensors, accelerometers and gyroscopes at each joint integrated in a glove (figure 1).

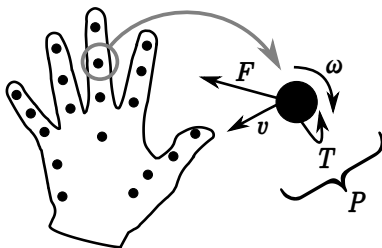


Fig. 1. Power measurements of the human hand using force sensors, accelerometers and gyroscopes. The power  $P$  in one element is equal to  $\vec{F} \cdot \vec{v} + \vec{T} \cdot \vec{\omega}$ .

Force sensors are also very interesting for robotics. Humanoid robots [4] or robotic hands [5] have to interact with the environment. Force sensors on top of the fingers and toes help the robot to measure load distributions on the hands and feet. Even the difference between rough and flat surfaces may be sensed by the robot.

For the three mentioned applications, a few specific requirements are applicable:

- the sensor should measure multiple (preferably six) degrees of freedom;
- the sensor is small, preferably less than  $1 \text{ cm}^2$  with a thickness of less than 1 mm;
- the sensor should be able to handle human forces, i.e. at least a few newtons.

Commercially available non-MEMS load cells support high force ranges, but are often too large to integrate in the applications mentioned above. There are MEMS-based force and torque sensors available in literature, but many lack the support for measuring torques [6], [7] or forces [8]. Besides, many sensors only support forces in the milli newton or micro newton range [9], [10], [11]. The fabrication process of most MEMS-based sensors is still in an experimental stage [6], [7], [11], [12], [13], they use non-trivial polymer technologies or crucial wafer bonding steps in the process. This makes the existing force sensors even less attractive, since above specified applications need tens of these expensive sensors per device.

However, a few force/torque sensors with piezoresistive readout satisfy most of the requirements. But sensors with capacitive readout have a better temperature performance, lower drift and higher sensitivity [14]. We present a miniature easy to fabricate multi-axis capacitive force/torque sensor with a large range. The sensor is initially developed for quantitative measurement of the interaction forces and torques between human fingers and the environment as a cheaper alternative for the sensor of Brookhuis et al. [13] But given its large force range and small dimensions, the sensor can also be used for other biomechanical applications or robotics.

## II. DESIGN

The sensor consists of a suspended core which is fabricated in the handle layer of an SOI wafer. The core is supported by v-shaped silicon springs. An applied load to the suspended core will result in a displacement. In-plane displacement caused by a shear force is measured by comb-structures

present in the device layer and results in a differential change in gap between the comb-fingers (figure 2).

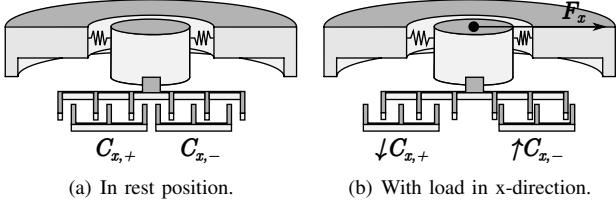


Fig. 2. Principle of operation for shear forces.

A normal force results in an out-of-plane displacement, which is measured by parallel plate electrodes (figure 3(b)). By differential measurement of two opposite electrodes (figure 3(c)), the applied torque is determined.

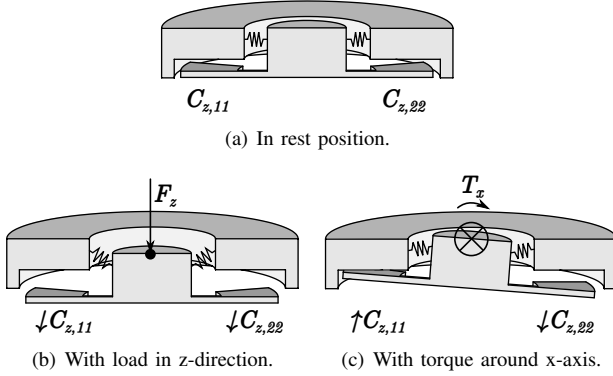


Fig. 3. Principle of operation for normal forces and torques.

#### A. Mechanics of the suspended core

Capacitive force/torque sensors are based on measuring a displacement. A system of springs convert the force to a displacement. Ideal springs obey Hooke's law.

$$F = k \cdot u, \quad (1)$$

$$T = c \cdot \phi, \quad (2)$$

with  $F$  the force,  $k$  the stiffness and  $u$  the displacement,  $T$  the torque,  $c$  the rotational stiffness and  $\phi$  the angle. The system of springs is dimensioned for forces in the first place, therefore, it is necessary to know the stiffness in each direction.

The proposed force/torque sensor uses the point symmetric v-shaped spring system shown in figure 4.

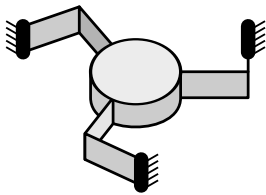


Fig. 4. A six degrees of freedom stage using folded sheet springs. The combination of three folded sheet springs is called a spring triplet.

The stiffness of the stage is equal for all shear directions [15]. The stage is initially only compliant for in-plane translations. By reducing the thickness of the sheets, the stage can be made compliant for normal direction and torques too. To increase stiffness in all directions, multiple spring triplets are added as is illustrated in figure 5.

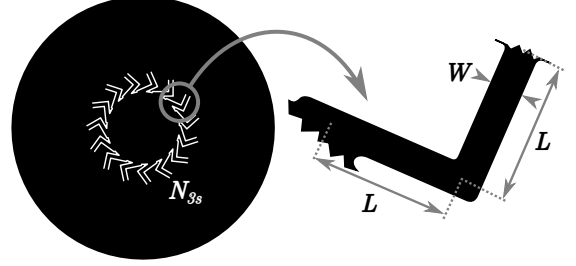


Fig. 5. The point symmetric v-shaped spring system and the parameters of each spring realized in the handle layer with thickness  $T$ .

The stiffness in shear directions is equal to:

$$k_x = \frac{45N_{3s}EI_x}{2L^3}, \quad (3)$$

with  $k_x$  the stiffness in x-direction,  $N_{3s}$  the number of spring triplets,  $E$  Young's modulus,  $I_x$  the second moment of area in x-direction and  $L$  the length of one spring part. The stiffness in normal direction is derived from the guided beam theory from [16]:

$$k_z = \frac{12(3N_{3s})EI_z}{(2L)^3}, \quad (4)$$

with  $k_z$  the stiffness in z-direction and  $I_z$  the second moment of area in z-direction. The second moments of area are as follows.

$$I_x = \frac{TW^3}{12}, \quad (5)$$

$$I_z = \frac{WT^3}{12}, \quad (6)$$

with  $T$  the thickness of the beam (equal to the thickness of the handle layer) and  $W$  the width of the beam.

The six degrees of freedom stage can be tuned for translations with parameters  $L$ ,  $W$  and  $N_{3s}$  by substituting the equations of 5 in equations 3 and 4:

$$k_x \propto \frac{N_{3s}}{L^3} W^3, \quad (7)$$

$$k_z \propto \frac{N_{3s}}{L^3} W. \quad (8)$$

The stiffness in x-direction compared to z-direction can be optimized by choosing the right value for the flexure width  $W$ , the stiffness in both directions can be tuned by the flexure part length  $L$ . When stiff structures are desired, the flexure part length  $L$  may be very small compared to the flexure width  $W$ . This decreases the validity of mentioned model. Adding multiple spring triplets  $N_{3s}$  allows the flexure part

length  $L$  to be larger. Table I shows the chosen dimensions for the proposed force/torque sensor.

TABLE I  
DIMENSIONS OF THE SUSPENDED CORE.

Quantity	Symbol	Value
Length of one spring part	$L$	480 $\mu\text{m}$
Width of the spring	$W$	108 $\mu\text{m}$
Thickness of the spring	$T$	400 $\mu\text{m}$
Number of spring triplets	$N_{3s}$	5
Diameter of the core	$D_{core}$	2.5 mm
Diameter of the sensor	$D_{sensor}$	9.24 mm
Stiffness in shear direction	$k_x$	$7.2 \cdot 10^6 \text{ N m}^{-1}$
Stiffness in normal direction	$k_z$	$1.9 \cdot 10^7 \text{ N m}^{-1}$

### B. Simulations of the suspended core

To verify the mathematical model and obtain an impression of the stress in the device, finite element method (FEM) simulations were done using COMSOL Multiphysics 4.3.0.151. The suspended core was drawn using computer aided design (CAD) software with the dimensions of table I. All structures have rounded corners (see figure 5) for two reasons:

- it reduces the maximum stress because the beams are thicker at places where the deformation would be originally higher;
- the etching process does not allow very sharp corners. By using round corners in the simulations, the simulations become more true to nature.

The simulations were done for a shear force of 10 N, a normal force of 10 N and a torque around a shear axis of 10 N mm. Table II shows the simulation results.

TABLE II  
FEM SIMULATION RESULTS.

Quantity	Symbol	Value
Stiffness in shear direction	$k_x$	$8.9 \cdot 10^6 \text{ N m}^{-1}$
Maximum stress for $F_x = 10 \text{ N}$	$\sigma_{max,x}$	8.5 GPa
Stiffness in normal direction	$k_z$	$1.2 \cdot 10^7 \text{ N m}^{-1}$
Maximum stress for $F_z = 10 \text{ N}$	$\sigma_{max,z}$	4.0 GPa
Rotational stiffness around shear axes	$c_x$	41 N m rad $^{-1}$
Maximum stress for $T_x = 10 \text{ N mm}$	$\sigma_{max,\phi}$	0.92 GPa

The found stiffnesses are slightly different than the model predicts. This may be because of the rounded corners. The found stresses for the simulated forces and torques are quite high for silicon; it can be concluded that the sensor's maximum range for force and torque will be in the order of newtons and newton millimeters respectively.

### C. Capacitive measurement

The sensor uses capacitive sensing structures. Figure 6 shows where the capacitors are located. There are large parallel electrode capacitors for normal force and torque measurements and comb-structures for shear force measurements. Both capacitor structures can be modeled as gap closing parallel plate capacitors [17]:

$$C(u) = N_p \epsilon \frac{A}{d_0 - u} \rightarrow C(F) = N_p \epsilon \frac{kA}{kd_0 - F}. \quad (9)$$

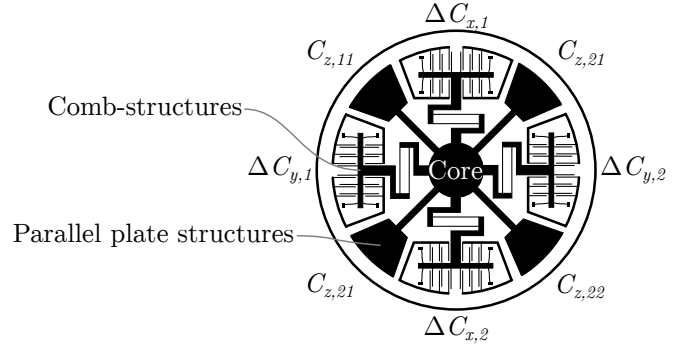


Fig. 6. Design of the device layer with declaration of all sensing capacitors.

With  $C$  the capacitance,  $N_p$  the number of parallel plates or finger pairs,  $\epsilon$  the absolute permittivity (in this case equal to the dielectric constant  $\epsilon_0$ ),  $A$  the overlapping area of one plate or finger pair,  $d_0$  the distance between the plates or fingers in rest,  $u$  the displacement in the same direction as  $d_0$ ,  $k$  the stiffness in the same direction as  $d_0$  and  $F$  the force in the same direction as  $d_0$ .

Normal forces are measured non-differentially using the parallel plate capacitor structures. For small forces, the closing gap capacitor model can be linearized using the Maclaurin series:

$$C_z(F_z) \approx \sum_{n=0}^1 \frac{C_z^{(n)}(F_z)}{n!} F_z^n = \frac{N_{p,z} \epsilon A_z}{d_{0,z}^2 k_z} F_z + C_z(0). \quad (10)$$

All parameters can be put in factor  $\beta_z$ :

$$C_z(F_z) \approx \beta_z F_z + C_z(0), \quad \text{with} \quad \beta_z = \frac{N_{p,z} \epsilon A_z}{d_{0,z}^2 k_z}. \quad (11)$$

$C(F)$  is an expression for the total capacitance between two plates or two combs. As can be seen in the sensing structures in figure 6 and in the operating principles in figure 2, shear forces are measured differentially. The differential capacitance  $\Delta C_x$  is defined as:

$$C_{x,\pm} = C_{x,rest} \pm C_x \rightarrow \Delta C_x = \frac{C_{x,+} - C_{x,-}}{2}, \quad (12)$$

i.e. the actual difference in capacitance due to displacement of one side, which can be measured by calculating half of the difference of the two measured structures (i.e. two plates or two combs). For small forces, the differential closing gap capacitor model may be linearized using the Maclaurin series:

$$C_x(F_x) \approx \sum_{n=0}^1 \frac{\Delta C_x^{(n)}(F_x)}{n!} F_x^n \quad (13)$$

$$= \beta_x F_x, \quad \text{with} \quad \beta_x = \frac{N_{p,x} \epsilon A_x}{d_{0,x}^2 k_x}. \quad (14)$$

The inverted  $\beta$ -factors are elements of calibration matrix  $\mathbf{K}$ , which maps the measured capacitances (corresponding to the defined capacitances in figure 6) to forces and torques.

$$\begin{bmatrix} F_x \\ F_y \\ F_z \\ T_x \\ T_y \\ T_z \end{bmatrix} = \mathbf{K} \begin{bmatrix} \Delta C_{x,1} \\ \Delta C_{x,2} \\ \Delta C_{y,1} \\ \Delta C_{y,2} \\ C_{z,11} \\ C_{z,12} \\ C_{z,21} \\ C_{z,22} \end{bmatrix}, \quad \text{with } \mathbf{K} \in \mathbb{R}^{6 \times 8} \quad (15)$$

The elements in calibration matrix  $\mathbf{K}$  will be found by measurements and will be reviewed in the discussion.

#### D. Comb-structures in the device layer

The comb-structures consist of combs mounted on a one degree of freedom stage which is supported by eight single flexures. Spring and lever structures are used to separate the different force components of the suspended core into comb-structure movements (figure 7). This transmission has (for small displacements) very high stiffness in x-direction and therefore transfers the full x-displacement from the core to the comb-structures. In z-direction, the stiffness of the transmission springs are more than 80 times lower than the springs of the comb-structures, so less than 2% of the z-displacement of the core is transferred to the comb-structures. In y-direction, the stiffness of the transmission springs are negligible compared to the the springs of the comb-structures making the comb-structures almost insensitive for y-displacements. In this way, crosstalk between the different force components is mechanically minimized.

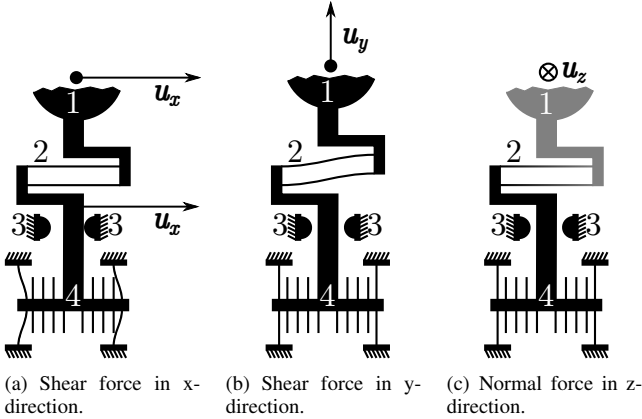


Fig. 7. Transmission (2) from core (1) to comb-structures (4). There are bumps (3) to prevent snapping of the fingers due to overloading.

All comb-structures have protection against snapping due to overloading: the stage will hit the bumps in figure 7 first before the fingers of the stage will snap to the fingers of the stator, as the distance between the finger pairs is  $7 \mu\text{m}$  and the distance between the bumps and the stage is  $5 \mu\text{m}$ .

The shear displacements are measured differentially. The stator consists of two symmetric electrically isolated parts (figure 8). Displacement of the stage results in an increasing gap at one half of the comb-structures and a decreasing gap at the other half of the comb-structures.

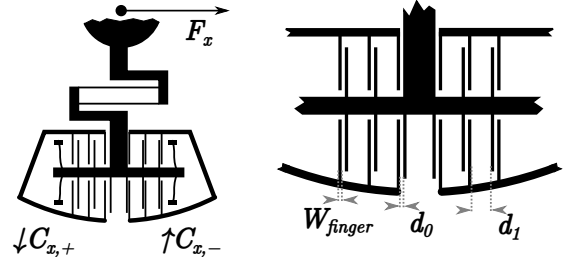


Fig. 8. Electrical design of the comb-structures.

The asymmetric positioning ( $d_1/d_0$ -ratio in figure 11(b)) of the shuttle-fingers between the stator-fingers is optimized, for a smaller  $d_1/d_0$ -ratio allows more finger structures but increases the parasitic capacitance and a larger  $d_1/d_0$ -ratio decreases the parasitic capacitance but takes more space. The curve in figure 9 is derived from equation 9, its maximum is where:

$$\frac{\partial}{\partial d_1} \frac{1}{d_0 + d_1 + 2W_{finger}} \left( \frac{1}{d_0} - \frac{1}{d_1} \right) = 0. \quad (16)$$

The fingers have a width  $W_{finger}$  of  $7 \mu\text{m}$ . The minimum distance between the fingers is  $7 \mu\text{m}$  which is used for  $d_0$ . Choosing  $\sim 20 \mu\text{m}$  for  $d_1$  leads to maximum capacitance change. All parameters are summarized in table III.

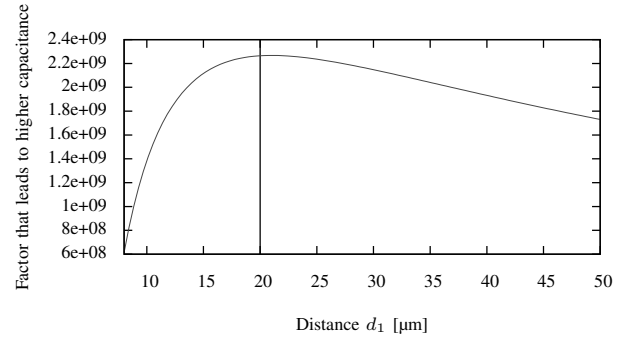


Fig. 9. Optimization of the finger distances: choosing  $d_0$  the maximum of the function will consequent in the highest capacitance.

TABLE III  
PARAMETERS OF THE COMB-STRUCTURES.

Quantity	Symbol	Value
Number of finger pairs	$N_{p,x}$	149
Average overlapping area per finger pair	$A_x$	$1.2 \cdot 10^{-8} \text{ m}^2$
Distance between fingers	$d_0$	$7 \mu\text{m}$
Distance between finger pairs	$d_1$	$20 \mu\text{m}$
Width of a finger	$W_{finger}$	$7 \mu\text{m}$
Average length of a finger	$L_{finger}$	$240 \mu\text{m}$
Thickness of a finger	$T_{device}$	$50 \mu\text{m}$

#### E. Parallel plate structures in the device layer

The parallel plate structures consist of flat plates that form a capacitor with the handle layer. The surface area of the plates is such that the capacitance is in the same order as the

capacitance of the comb-structures. The plate is electrically connected to the bond pad with springs that are compliant in all directions. In figure 10, one of the normal sensing structures is shown.

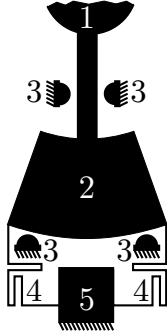


Fig. 10. Capacitor plate (2) is directly coupled with the core (1). Wires (4) connect the capacitor plate to the bond pad (5) and have no effect on the mechanics due to their folds. There are bumps (3) to prevent snapping of the plates due to shear overloading.

All floating structures need to have perforations for the release etch, this will be described in the fabrication process. Therefore, one of the normal structure plates is a grid of silicon beams as is illustrated in figure 11. This influences the capacitor model from equation 9, since the overlapping surface area decreases. These effects are simulated using FEM. The capacitance of a grid with the dimensions of figure 11 and a solid plate turned out to be approximately 11% lower compared to the capacitance of two parallel plates. The fringing effects compensate for the holes in the plate.

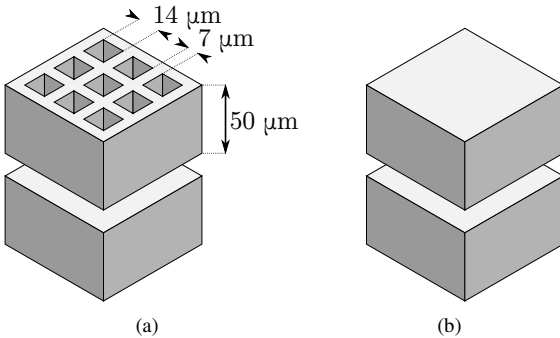


Fig. 11. Parallel plate structure simulations. The capacitance of the situation with one perforated plate (a) performs 11% lower compared to the situation with two solid parallel plates (b).

All parameters of the parallel plate structures are summarized in table IV.

TABLE IV  
PARAMETERS OF THE PARALLEL PLATE STRUCTURES.

Quantity	Symbol	Value
Area of one plate	$A_z$	$9.4 \cdot 10^{-7} \text{ m}^2$
Perforation width and length	$W_{hole}$	14 $\mu\text{m}$
Grid beam width	$W_{grid}$	7 $\mu\text{m}$

Besides the parallel plate structures for measurements, there are several static parallel plate capacitor structures in the

sensor for reference measurements. These capacitors are not able to move and can be used to compensate for temperature and humidity effects.

#### F. Prevention of stiction

To achieve high sensitivity, large capacitor structures are needed. But care must be taken when designing such large floating structures, as stiction may occur. All large floating structures (figure 8 and figure 10) can be modeled as doubly clamped beams since they are always supported at two ends, this is illustrated in figure 12.

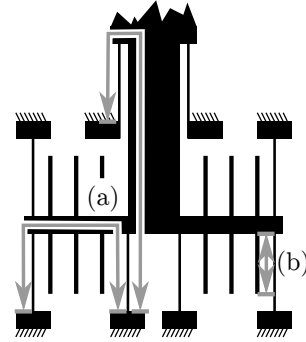


Fig. 12. Paths in the structures that can be modeled as doubly clamped beams (a) or beams with a free end (b).

Following equation gives the maximum length for these structures [18].

$$L_{critical} = 2.9 \sqrt[4]{\frac{3 ET_{device}^3 g^2}{8 \gamma_s}} \approx 3000 \mu\text{m}, \quad (17)$$

with  $L_{critical}$  the critical length,  $E$  Young's modulus (of silicon),  $T$  the thickness of the beams (i.e. the thickness (50  $\mu\text{m}$ ) of the device layer),  $g$  the gap between the device layer and the handle layer (4  $\mu\text{m}$ ) and  $\gamma_s$  the adhesion energy (assumed to be 100  $\text{mJ m}^{-2}$ ). As a result of above equation, all doubly clamped structures are less than 3000  $\mu\text{m}$  in length. For structures with a free end,  $L_{critical}$  should be 2.9 times lower, hence, all structures that have a free end are always shorter than 1000  $\mu\text{m}$ .

### III. FABRICATION

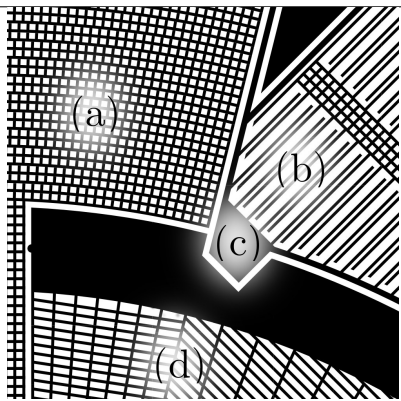
A 100 mm p-type SOI wafer with a handle layer of 400  $\mu\text{m}$ , a device layer of 50  $\mu\text{m}$  and a box layer of 4  $\mu\text{m}$  is used for the device.

The fabrication process needs two masks: the mask for etching the handle layer and the mask for etching the device layer. The mask for the handle layer has relatively large structures. The rule of thumb of 1:10 [19] for aspect ratio is maintained, giving a minimum size for the trenches of 40  $\mu\text{m}$ . The trenches are chosen slightly larger with 50  $\mu\text{m}$ .

The device layer contains more complicated structures. Table V gives the design rules that are related to the embedded figure with a closeup of the most complicated structures.

Because all chips are circular, hexagon packing is used to optimize the use of the surface area of one wafer (figure 13).

TABLE V  
DESIGN RULES WITH A CLOSEUP OF THE DEVICE LAYER.



(a)	Frame with holes of at least $14\ \mu\text{m}$ and beams of $7\ \mu\text{m}$ at maximum.
(b)	Comb fingers with a length of $300\ \mu\text{m}$ at maximum and with a width of $7\ \mu\text{m}$ . There is $7\ \mu\text{m}$ spacing between the fingers, making this the smallest open areas in the mask.
(c)	All anchors are at least $100\ \mu\text{m}$ by $100\ \mu\text{m}$ .
(d)	All areas that are not in use are either solid or framed, leaving holes of maximum $40\ \mu\text{m}$ by $40\ \mu\text{m}$ .

There is a trench around the chip in both the handle layer and the device layer. There are small mounting points on both sides of the chip to fix the chips in the wafer. Releasing of the samples can be simply done by breaking them out. This technique does not need a dicing machine or other advanced methods and it allows arbitrary shapes for the chips. The trenches around the chips are the same as the smallest trenches on the chip (i.e.  $7\ \mu\text{m}$  for the device layer and  $50\ \mu\text{m}$  for the handle layer) to prevent damage to the oxide layer and possible leakage while etching.

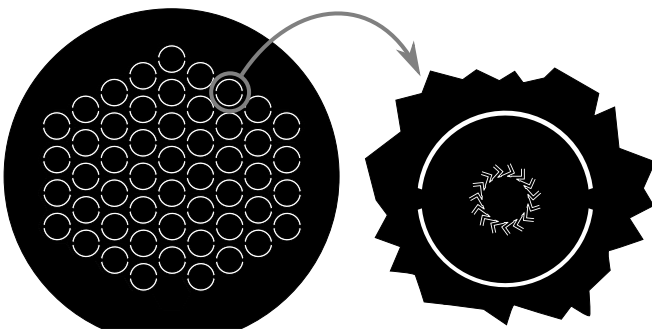


Fig. 13. Impression of the location of the chips and how they can be broken out of the wafer.

#### A. Wet oxidation and lithography

Wet oxidation (figure 14(b)) was done at  $1150\ ^\circ\text{C}$ . After 14 hours, the wafers had an oxide layer of  $1963\ \text{nm}$ . The SOI wafers were coated with positive photoresist (Fujifilm OiR 907-17).

#### B. Oxide etching and resist stripping

Etching of oxide was done using reactive ion etching (RIE) with an Adixen AMS100. A standard Bosch process was

used with a recipe based on an argon (Ar) and fluoroform ( $\text{CHF}_3$ ) chemistry. Both sides of the wafer were etched for 6 min (figures 14(d) and 14(g)). Resist stripping was done in  $\text{O}_2$ -plasma using a Tepla 300E and nitric acid ( $\text{HNO}_3$ ) (figures 14(e) and 14(h)).

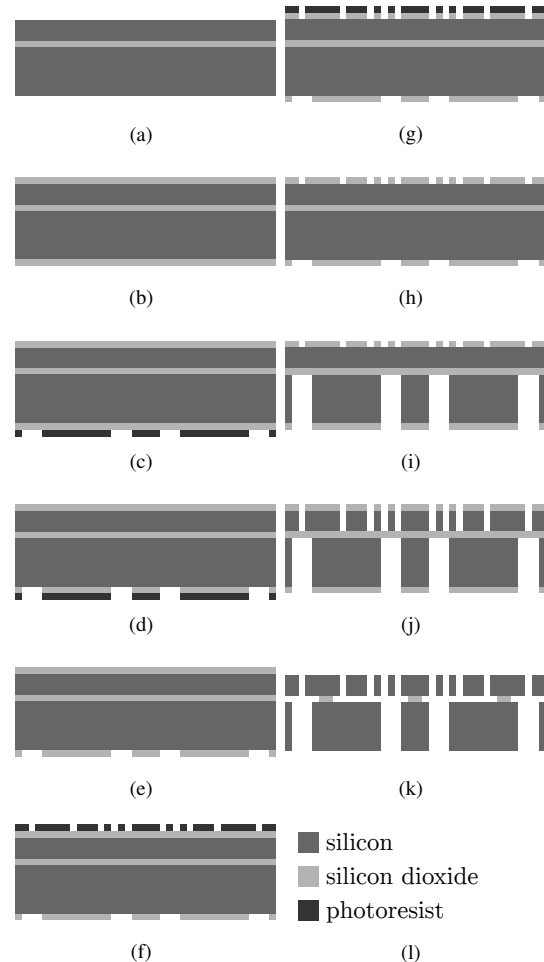


Fig. 14. Fabrication process: (a) SOI wafer, (b) oxidation, (c) lithography on handle layer, (d) etching of oxide on handle layer, (e) resist stripping, (f) lithography on device layer (g) etching of oxide on device layer, (h) resist stripping, (i) etching of handle layer, (j) etching of device layer, (k) release etch, (l) materials.

#### C. Handle layer and device layer etching

The handle layer was etched using DRIE with an Adixen AMS100. Sulfur hexafluoride ( $\text{SF}_6$ ) was used as etchant and fluoro carbon ( $\text{C}_4\text{F}_8$ ) was used for the deposition of passivation layers. The handle layer etch underwent the process for 37 min (figure 14(i)). The device layer etch took 17 min (figure 14(j)). The fluorocarbon residues were removed using piranha cleaning and  $\text{O}_2$ -plasma.

#### D. Release etch

The chips were pushed out of the wafer. Particles arose from the broken mounting points and contaminated the chips. The pushed out chips underwent therefore ultrasonic cleaning. A wet etch with 50% HF for 2 min is performed and etched

through the box layer of the SOI wafer. To prevent capillary forces making the structures snap to each other, the final release etch was done using vapor HF and took 30 min (figure 14(k)).

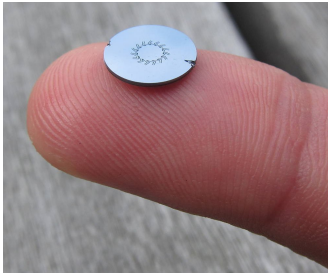
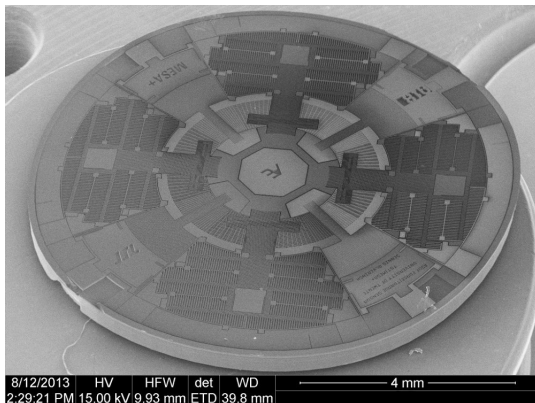


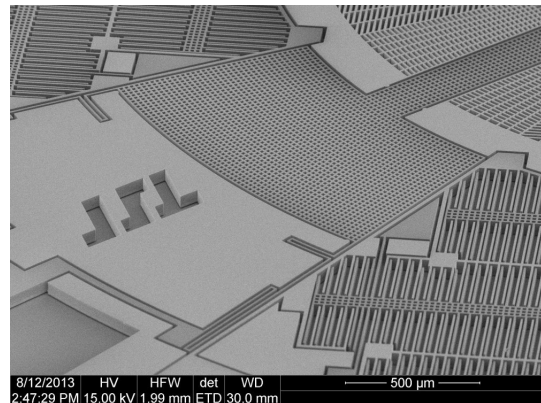
Fig. 16. Photo of a fabricated force/torque sensor. The sensor has a diameter of 9.24 mm and a thickness of 0.45 mm.

### E. Fabrication results

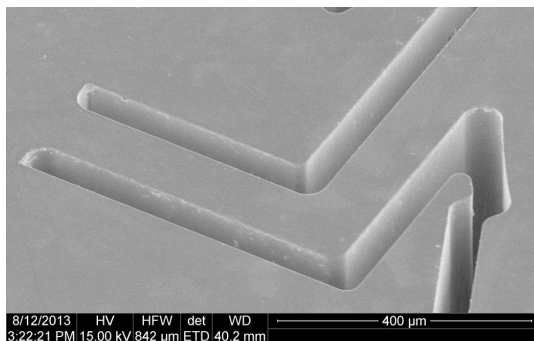
The under etching was checked by removing several anchors of the device layer with a piece of tape. The anchors were between  $5\mu\text{m}$  and  $10\mu\text{m}$  under etched, which is enough to release the structures and not too much to release the anchors, since all floating structures are at maximum  $10\mu\text{m}$  by  $10\mu\text{m}$  and all anchors are at least  $100\mu\text{m}$  by  $100\mu\text{m}$ . By breaking the chip, potential tapering was inspected with scanning electron microscopy (SEM). But this appeared to be negligible. figure 15 contains SEM images of the result.



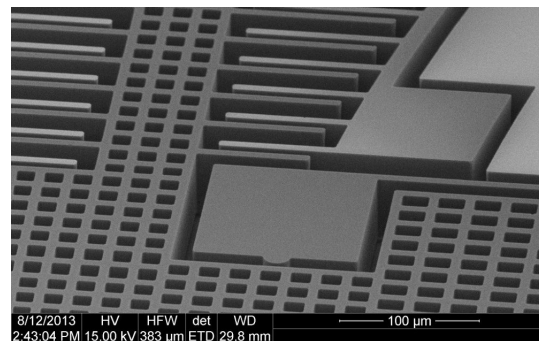
(a) Overview of the device layer.



(b) Close-up of the parallel plate structures.



(c) Close-up of the v-shaped springs.

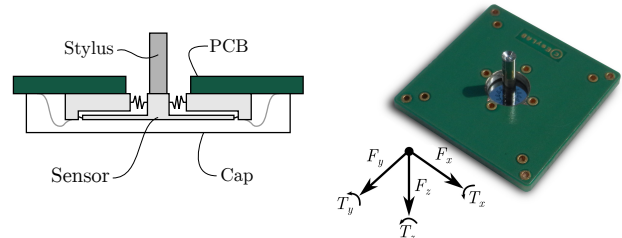


(d) Close-up of the comb-structures.

Fig. 15. SEM images

### F. Final assembly

A hole is drilled in a printed circuit board (PCB). The sensor is mounted with the handle layer on the PCB using glue that cures when exposed to UV light. The sensor is wire bonded and a stylus is mounted using epoxy glue on the top of the suspended core through the hole in the PCB (figure 17).



(a) Sensor is mounted on a PCB and wire bonded. The stylus is attached to the mesa and a cap protects the sensor structures. (b) A photo of an assembled sensor.

Fig. 17. Final assembly.

## IV. CHARACTERIZATION

The force/torque sensor is characterized for five degrees of freedom, since there was no measurement setup realized for torques around normal axes ( $T_z$ ).

### A. Method

The sensor's force behavior is characterized by applying loads in shear and normal direction. An extra stylus is mounted on the back of the chip to make sure pure shear forces were applied. Torques around shear axes were measured by applying a load on the stylus at a defined distance from the sensor. The mechanical measurement setups for the three measurements are shown in figure 18.

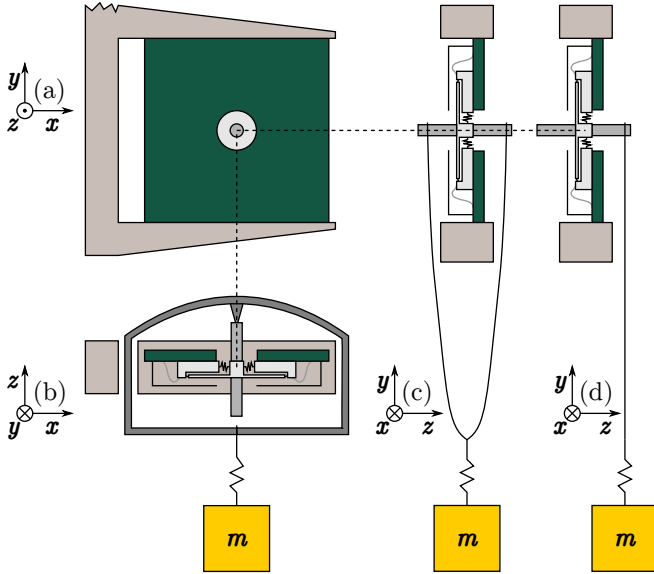


Fig. 18. Measurement setups for applying loads to the sensor: (a) clamped assembled sensor, (b) measuring normal force, (c) measuring shear force and (d) measuring torque.

The measurement electronics are schematically drawn in figure 19.

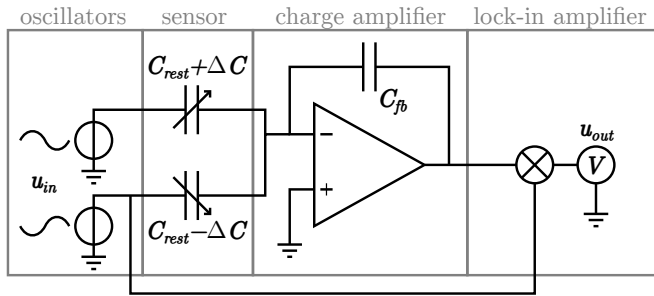


Fig. 19. Electronic setup for differential measurements including two oscillators, a charge amplifier and a lock-in amplifier. Non-differential measurements are done using only one oscillator.

Measuring the (differential) change in capacitance is done using a custom built charge amplifier with a capacitor of 10 pF in the feedback loop. This makes the output of the charge amplifier as follows.

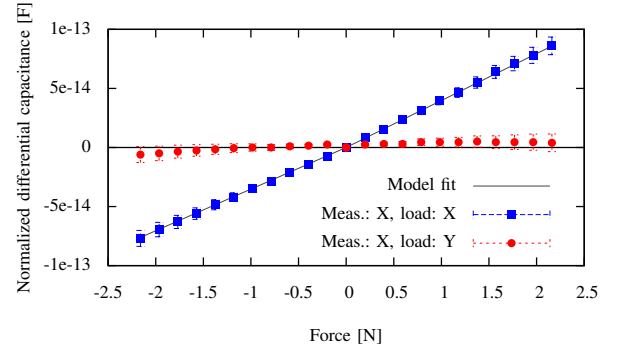
$$u_{out} = \frac{2\Delta C}{C_{fb}} u_{in} \quad (18)$$

With  $u_{out}$  the output voltage of the charge amplifier,  $u_{in}$  the input voltage,  $\Delta C$  the differential change in capacitance and  $C_{fb}$  the feedback capacitance of the charge amplifier.

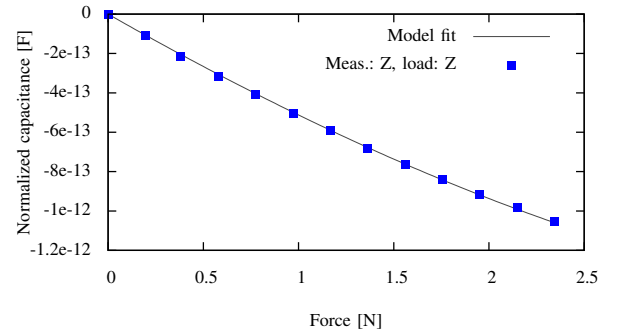
Two function generators (Agilent 33220A) with sine waves of 50 kHz with 180° phase shift are used for the input signals. The output of the charge amplifier is connected to a lock-in amplifier (Stanford Research Systems SR830) which was directly synchronized with one of the function generators.

### B. Results

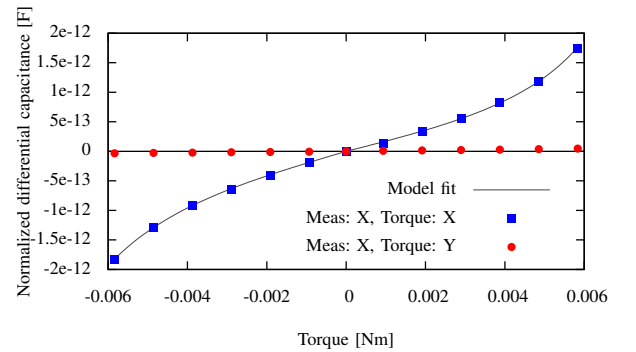
Figure 20 shows the results for applied shear forces, normal forces and torques. Shear force measurements (figure 20(a)) show a very linear (>99%) differential change in capacitance with a sensitivity of 38 fF N<sup>-1</sup>. The values are corrected for offset. The linear model is corrected for positive and negative shear forces with a factor of 0.88 and 0.78 respectively.



(a) Differential capacitance measurements of the comb-structures with varying shear forces.



(b) Capacitance measurements of the parallel plate structures with varying normal forces.



(c) Differential capacitance measurements of the parallel plate capacitors with varying torque.

Fig. 20. Measurement results.

Normal force measurements (figure 20(b)) show a high sensitivity of 550 fF N<sup>-1</sup> in the linear region. The values are

corrected for offset. A corrected model using the fourth order Maclaurin expansion from the design section is fit through the measured values. The model is corrected for the distance between the parallel plates, the overlapping area of the plates and the stiffness with factors 0.45, 0.46 and 0.45 respectively.

The mentioned correction factors are necessary for the compensation of non-ideal effects in the mechanics, electrostatics or fabrication process. The distance between the capacitor structures may be smaller or larger than expected due to the etching process for example.

In figure 20(c) torque measurements around a shear axis are shown. The fitted model is based on a differential version of the normal force model.

The mounted styli on top and bottom of the sensor were the first parts that broke in the measurement setup. Mechanical robustness tests without styli show that the sensor can be safely overloaded in normal direction with more than 15 N without causing damage to the sensor.

## V. DISCUSSION

The fabrication process and calibration will be discussed.

### A. Fabrication

The mounting points that have to break for releasing the chips are too strong. This causes the need for a large force to remove the chips from the wafer. Besides, the very thin etched ring in the device layer (7  $\mu\text{m}$ ) caused the chips to get stuck after breaking the mounting points.

Some chips broke because of this and became instantaneously useless, others were contaminated by particles and had to be cleaned in an ultrasonic bath. Most particles were removed in this way. Nevertheless, it is recommended to reduce the strength of the mounting points and increase the width of the etched rings around the chips.

### B. Calibration

A slight crosstalk is observed when a shear force in orthogonal direction with respect to the measured direction is applied, caused by misalignment in the measurement setup (figure 20(a)). For this crosstalk is expected to be a consequent of the measurement setup, it is not included in the calibration matrix  $\mathbf{K}$ . The error bars in figure 20(a) represent misalignments from  $-5^\circ$  until  $5^\circ$ .

Actual crosstalk occurs in the comb-structures when a torque is applied around shear axes. The rotation of the suspended core leads to a translation of the comb-structures as is illustrated in figure 21.

The crosstalk component is measured and its results are plotted in figure 22.

It can be concluded that the crosstalk measurements for forces applied at a distance of 1 cm of the sensor is in the same order of magnitude as for shear forces. However, there can be compensated for the crosstalk component using torque measurements with the parallel plate structures. Calibration matrix  $\mathbf{K}$  is a six by eight matrix consisting of the inverted

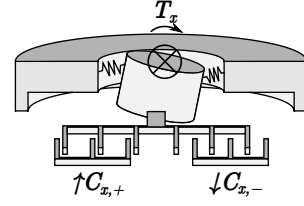


Fig. 21. Crosstalk in the comb-structures as consequence of an applied torque around a shear axis.

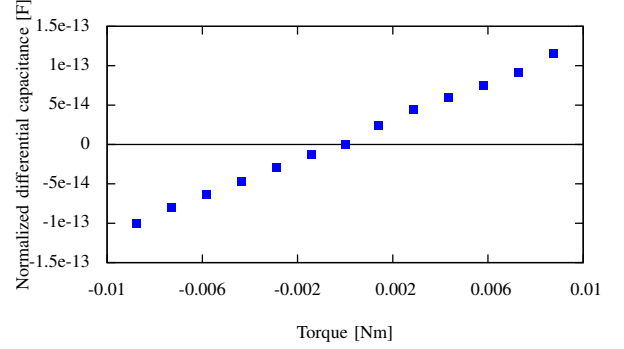


Fig. 22. Differential capacitance measurements of the comb-structures with varying torques.

elements  $\beta^{-1}$  and mentioned crosstalk components  $\alpha^{-1}$ . Calibration matrix  $\mathbf{K}$  is only valid for small forces and torques in the linear region. Expressions for the elements  $\beta_x^{-1}$  and  $\beta_z^{-1}$  were already given in equations 13 and 11.

$$\mathbf{K} = \begin{bmatrix} \beta_x^{-1} & \beta_x^{-1} & 0 & 0 & -\alpha_x^{-1} & \alpha_x^{-1} & -\alpha_x^{-1} & \alpha_x^{-1} \\ 0 & 0 & \beta_y^{-1} & \beta_y^{-1} & -\alpha_y^{-1} & \alpha_y^{-1} & -\alpha_y^{-1} & \alpha_y^{-1} \\ 0 & 0 & 0 & 0 & \beta_z^{-1} & \beta_z^{-1} & \beta_z^{-1} & \beta_z^{-1} \\ 0 & 0 & 0 & 0 & \beta_\phi^{-1} & \beta_\phi^{-1} & -\beta_\phi^{-1} & -\beta_\phi^{-1} \\ 0 & 0 & 0 & 0 & \beta_\theta^{-1} & -\beta_\theta^{-1} & \beta_\theta^{-1} & -\beta_\theta^{-1} \\ \text{N/A} & \text{N/A} \end{bmatrix} \quad (19)$$

Characterization has been done and the crosstalk components are defined. The elements of calibration matrix  $\mathbf{K}$  can be calculated from the measurement results and are enumerated in figure VI.

TABLE VI  
CALIBRATION MATRIX ELEMENTS.

Element	Value	Element	Value
$\beta_x^{-1}$	$2.6 \cdot 10^{13}$	$\alpha_x^{-1}$	$1.7 \cdot 10^{12}$
$\beta_y^{-1}$	$2.6 \cdot 10^{13}$	$\alpha_y^{-1}$	$1.7 \cdot 10^{12}$
$\beta_z^{-1}$	$2.2 \cdot 10^{12}$	$\alpha_z^{-1}$	0
$\beta_\phi^{-1}$	$5.3 \cdot 10^9$	$\alpha_\phi^{-1}$	0
$\beta_\theta^{-1}$	$5.3 \cdot 10^9$	$\alpha_\theta^{-1}$	0

TABLE VII  
SUMMARY OF THE SENSOR PERFORMANCE.

Quantity	Range	Sensitivity of linear region
$F_x$	2.16 N	38 fF N <sup>-1</sup>
$F_y$	2.16 N	38 fF N <sup>-1</sup>
$F_z$	2.34 N	550 fF N <sup>-1</sup>
$T_x$	5.84 N mm	23 nF N <sup>-1</sup> m <sup>-1</sup>
$T_y$	5.84 N mm	23 nF N <sup>-1</sup> m <sup>-1</sup>
$T_z$	N/A	N/A

## VI. CONCLUSION

A miniature large range five degrees of freedom force/torque sensor is designed, realized and characterized. The first measurements were presented. It has a minimum force range of 2 N in shear and normal direction and a torque range of more than 6 N mm. The sensor shows in shear and normal direction competing sensitivities of  $38 \text{ fFN}^{-1}$  and  $550 \text{ fFN}^{-1}$  respectively. The proposed sensor is therefore suitable for biomechanical and robotic applications. The fabrication takes only two masks, making it a cheap and relatively fast process. The fabrication is also expected to be very reproducible, making it an interesting process for mass production. The rotation around the normal axis can be measured by the sensor, but is not yet characterized. Future work will focus on further characterization of this sixth degree of freedom, mechanical compensation for the crosstalk component and increasing the range and sensitivity.

## REFERENCES

- [1] A. F. Mak, M. Zhang, and D. A. Boone, "State-of-the-art research in lower-limb prosthetic biomechanics-socket interface," *Journal of rehabilitation research and development*, vol. 38, no. 2, pp. 161–173, 2001.
- [2] M. W. Legro, G. Reiber, M. del Aguila, M. J. Ajax, D. A. Boone, J. A. Larsen, D. G. Smith, and B. Sangeorzan, "Issues of importance reported by persons with lower limb amputations and prostheses," *Journal of rehabilitation research and development*, vol. 36, no. 3, 1999.
- [3] P. H. Veltink, H. Kortier, and H. M. Schepers, "Sensing power transfer between the human body and the environment," *Biomedical Engineering, IEEE Transactions on*, vol. 56, no. 6, pp. 1711–1718, 2009.
- [4] K. Hirai, M. Hirose, Y. Haikawa, and T. Takenaka, "The development of honda humanoid robot," in *Robotics and Automation, 1998. Proceedings. 1998 IEEE International Conference on*, vol. 2. IEEE, 1998, pp. 1321–1326.
- [5] J. Butterfaß, M. Grebenstein, H. Liu, and G. Hirzinger, "Dlr-hand ii: Next generation of a dextrous robot hand," in *Robotics and Automation, 2001. Proceedings 2001 ICRA. IEEE International Conference on*, vol. 1. IEEE, 2001, pp. 109–114.
- [6] J. A. Dobrzynska and M. A. M. Gijs, "Capacitive flexible force sensor," *Procedia Engineering*, vol. 5, pp. 404–407, 2010.
- [7] E. S. Hwang, J. Seo, and Y. J. Kim, "A polymer-based flexible tactile sensor for both normal and shear load detections and its application for robotics," *Journal of Microelectromechanical Systems*, vol. 16, no. 3, pp. 556–563, 2007.
- [8] L. Beccai, S. Roccella, A. Arena, F. Valvo, P. Valdastri, A. Menciassi, M. C. Carrozza, and P. Dario, "Design and fabrication of a hybrid silicon three-axial force sensor for biomechanical applications," *Sensors and Actuators A: Physical*, vol. 120, no. 2, pp. 370–382, 2005.
- [9] H. K. Chu, J. K. Mills, and W. L. Cleghorn, "Design of a high sensitivity capacitive force sensor," in *7th IEEE Conference on Nanotechnology*. IEEE, 2007, pp. 29–33.
- [10] H. Muhammad, C. Oddo, L. Beccai, C. Recchiuto, C. Anthony, M. Adams, M. Carrozza, D. Hukins, and M. Ward, "Development of a bioinspired MEMS based capacitive tactile sensor for a robotic finger," *Sensors and Actuators A: Physical*, vol. 165, no. 2, pp. 221–229, 2011.
- [11] H. K. Lee, J. Chung, S. I. Chang, and E. Yoon, "Normal and shear force measurement using a flexible polymer tactile sensor with embedded multiple capacitors," *Journal of Microelectromechanical Systems*, vol. 17, no. 4, pp. 934–942, 2008.
- [12] Y. Takei, K. Noda, T. Kawai, T. Tachimura, Y. Toyama, T. Ohmori, K. Matsumoto, and I. Shimoyama, "Triaxial force sensor for lingual motion sensing," in *IEEE 25th International Conference on Micro Electro Mechanical Systems (MEMS)*. IEEE, 2012, pp. 128–131.
- [13] R. A. Brookhuis, T. S. J. Lammerink, R. J. Wiegerink, M. J. de Boer, and M. C. Elwenspoek, "3D Force sensor for Biomechanical applications," *Sensors and Actuators A: Physical*, 2012.
- [14] R. Puers, "Capacitive sensors: when and how to use them," *Sensors and Actuators A: Physical*, vol. 37, pp. 93–105, 1993.
- [15] H. Soemers, *Design principles for precision mechanisms*, 2010.
- [16] E. Oberg, F. D. Jones, H. L. Horton, and H. H. Ryffel, *Machinery's Handbook*, 27th ed. Industrial Press, 2004.
- [17] R. P. Feynman, R. B. Leighton, and M. Sands, *The Feynman lectures on physics, vol. 2: Mainly electromagnetism and matter*. Addison-Wesley, 1979.
- [18] N. Tas, T. Sonnenberg, H. Jansen, R. Legtenberg, and M. Elwenspoek, "Stiction in surface micromachining," *Journal of Micromechanics and Microengineering*, vol. 6, no. 4, p. 385, 1996.
- [19] H. Jansen, M. De Boer, S. Unnikrishnan, M. Louwerse, and M. Elwenspoek, "Black silicon method X: a review on high speed and selective plasma etching of silicon with profile control: an in-depth comparison between Bosch and cryostat DRIE processes as a roadmap to next generation equipment," *Journal of micromechanics and microengineering*, vol. 19, no. 3, p. 033001, 2009.



**Conference abstract**

This appendix contains the original abstract for the MEMS 2014 conference in San Francisco.

## A LARGE RANGE MULTI-AXIS CAPACITIVE FORCE/TORQUE SENSOR USING A SINGLE SOI WAFER

D. Alveringh, R.A. Brookhuis, R.J. Wiegerink and G.J.M. Krijnen

MESA+ Institute for Nanotechnology, University of Twente, Enschede, THE NETHERLANDS

### Novelty

A miniature silicon capacitive force/torque sensor is designed and realized to be used for biomechanical applications. The sensor is capable of measuring 5 degrees of freedom with a force range of 2 N in shear and normal direction and a torque range of more than 6 N mm. The sensor has a high sensitivity of  $38 \text{ fF N}^{-1}$  in shear direction with high linearity (>99%) and  $450 \text{ fF N}^{-1}$  in normal direction. To minimize crosstalk, a novel mechanical spring system is used. The fabrication of the sensor requires only two masks for deep reactive ion etching, making it easy to fabricate. This is the first 5 degrees of freedom force/torque sensor in this force range made in a single SOI wafer.

### Motivation

Miniaturized multi-axis force and torque sensors are widely used in robotics, tactile sensing and medical applications [1]. E.g. for many prosthetic applications, which require safe interaction with people, small force sensors are needed to adjust the shape of the prosthesis and make it fit well [2]. Existing force sensors with high force ranges are often big, can measure just one axis or have a complicated fabrication process [4]. We present an easy to fabricate multi-axis force sensor with a large range, having a thickness of less than 0.5 mm and a diameter of 9.24 mm. The sensor will be used for quantitative measurement of the interaction forces and torques between human fingers and the environment. Given its large force range and small dimensions, the sensor can also be used for other biomechanical applications or robotics.

### Design

The sensor consists of a mesa which is fabricated in the handle layer of an SOI wafer. The mesa is supported by v-shaped silicon springs. An applied load to the mesa will result in a displacement. In-plane displacement caused by a shear force is measured by comb-structures present in the device layer and results in a differential change in gap between the comb-fingers (figure 1(d)). Spring and lever structures are used to separate the different force components into comb-structure movements (figure 1(e)). A normal force results in an out-of-plane displacement, which is measured by parallel plate electrodes (figure 1(b)). By differential measurement of two opposite electrodes (figure 1(c)), the applied torque is determined.

### Fabrication

The sensor is fabricated using deep reactive ion etching in both layers of an SOI-wafer. Vapor-HF is used to release the comb-structures from the buried oxide layer. After fabrication, the sensor is pushed out of the wafer, eliminating the need for dicing and allowing a circular shaped chip (figure 3(a)). The sensor is mounted with the handle layer side on a PCB which supports the sensor when a load is applied (figure 4(a)). A stainless steel stylus is mounted using adhesive bonding on top of the mesa to apply forces and moments to the sensor.

### Results

Figure 5 shows the results for applied shear forces, normal forces and torques. Shear force measurements (figure 5(a)) show a very linear (>99%) differential change in capacitance with a sensitivity of  $38 \text{ fF N}^{-1}$ . A slight crosstalk is observed when a shear force in orthogonal direction is applied, caused by misalignment in the measurement setup. In figure 5(b) torque measurements around x-axis and y-axis are shown and are in good agreement with the model. Normal force measurements (figure 5(c)) show a high sensitivity of  $450 \text{ fF N}^{-1}$ . Mechanical robustness tests show that the sensor can be safely overloaded in normal direction with more than 15 N without causing damage to the sensor.

**Word count: 586**

**Submitting author:** D. Alveringh, MESA+ Institute for Nanotechnology, University of Twente, P.O. Box 217, 7500 AE, Enschede, THE NETHERLANDS, E-mail: dennis@alveringh.eu, Tel: +31-6-3301-3029.

### References

- [1] P.H. Veltink, et al., IEEE Transactions on Biomedical Engineering, vol. 56, p. 1711–1718, 2009
- [2] L. Beccai, et al., Sensors and Actuators A: Physical, vol. 120, no. 2, p. 370–382, 2005
- [3] R.A. Brookhuis, et al., Sensors and Actuators A: Physical, vol. 182, p. 28–33, 2012
- [4] J.A. Dobrzynska, et al., Sensors and Actuators A: Physical, vol. 173, p. 127–135, 2012

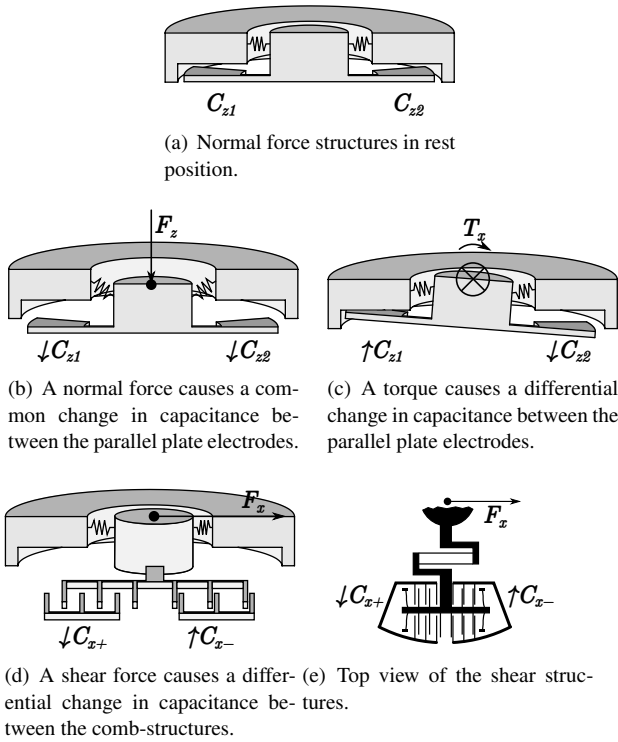


Figure 1: Operating principle.

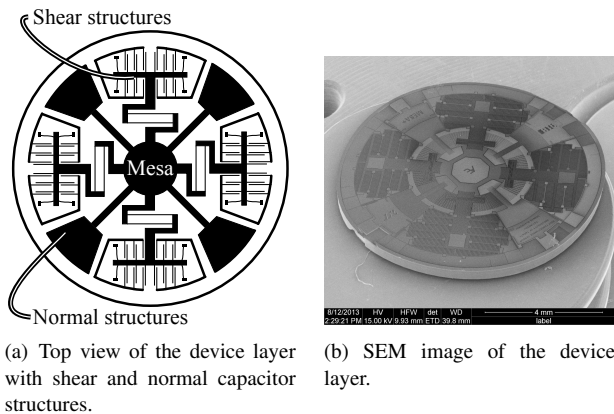


Figure 2: Overview of sensing structures.

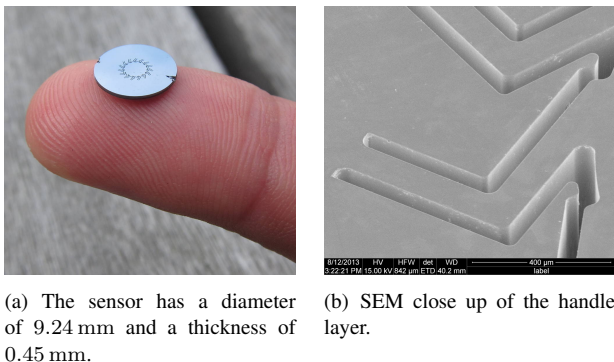


Figure 3: Spring structures.

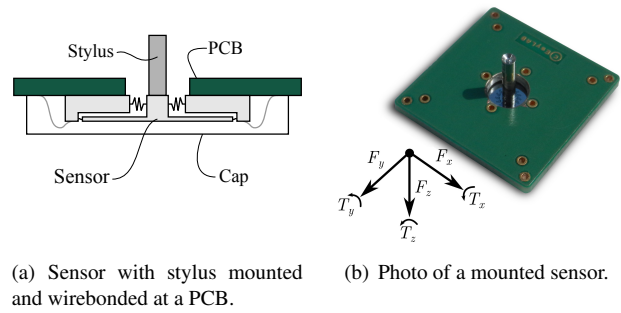
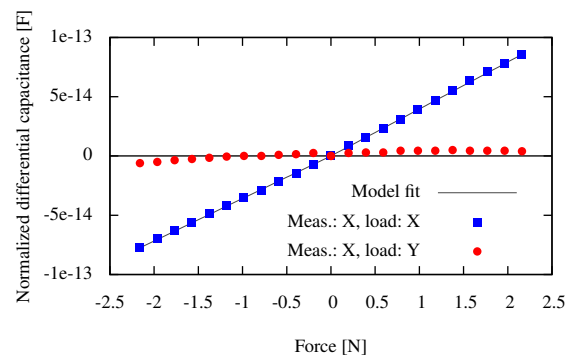
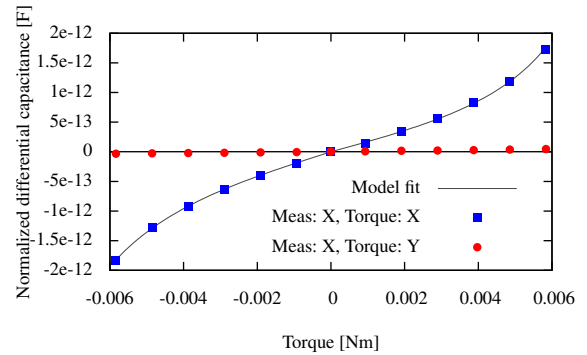


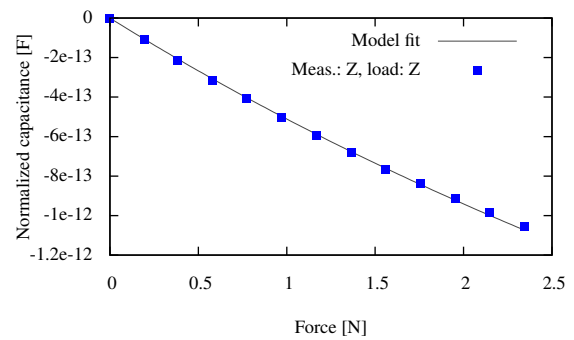
Figure 4: Photos of the sensor.



(a) Differential capacitance measurements of the shear structures with varying shear forces.



(b) Differential capacitance measurements of the normal capacitors with varying torque.



(c) Capacitance measurements of the normal structures with varying normal forces.

Figure 5: Measurements.



## **Technical fabrication process document**

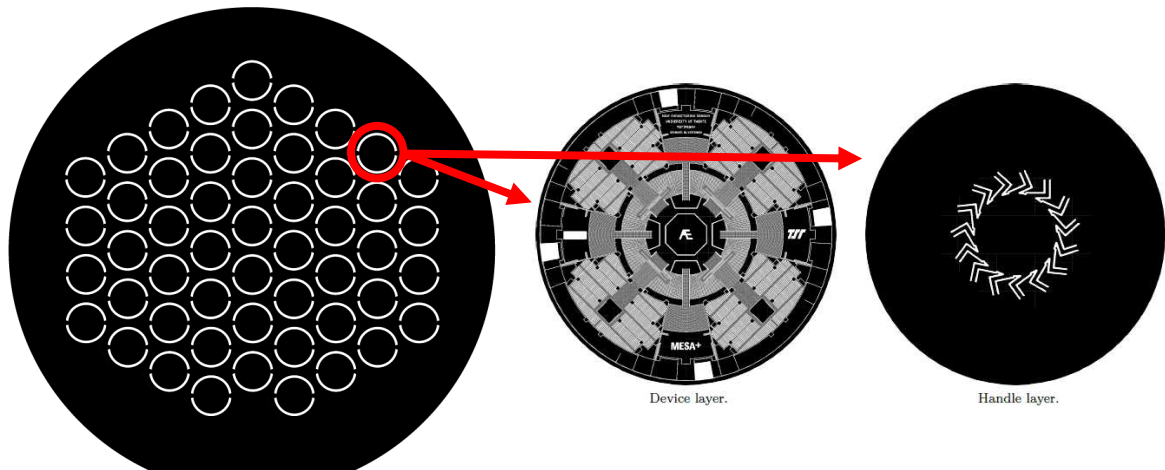
This appendix contains the original technical fabrication process document.

**Design description**

The device that will be fabricated using this process document is a six degrees of freedom force and torque sensor made in one silicon-on-insulator (SOI) wafer. The force/torque sensor will be simply made of two layers. The handle layer of 400  $\mu\text{m}$  will contain large spring structures to form a six degrees of freedom stage that has the same order of stiffness in all directions. The device layer of 50  $\mu\text{m}$  will contain capacitor plates oriented in all three dimensions for capacitive measurements.

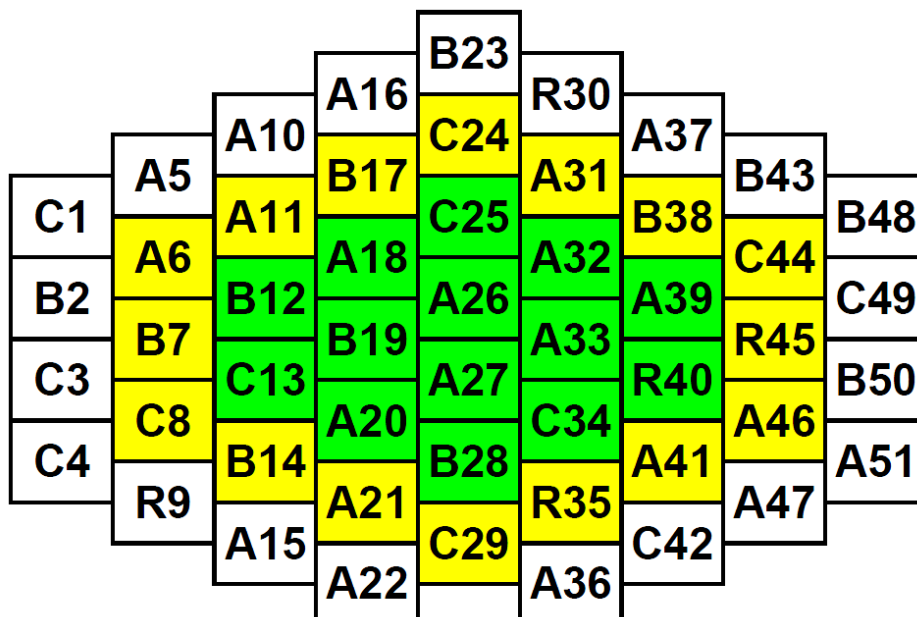
**Masks**

The process uses two masks, one for etching the handle layer and one for etching the device layer.

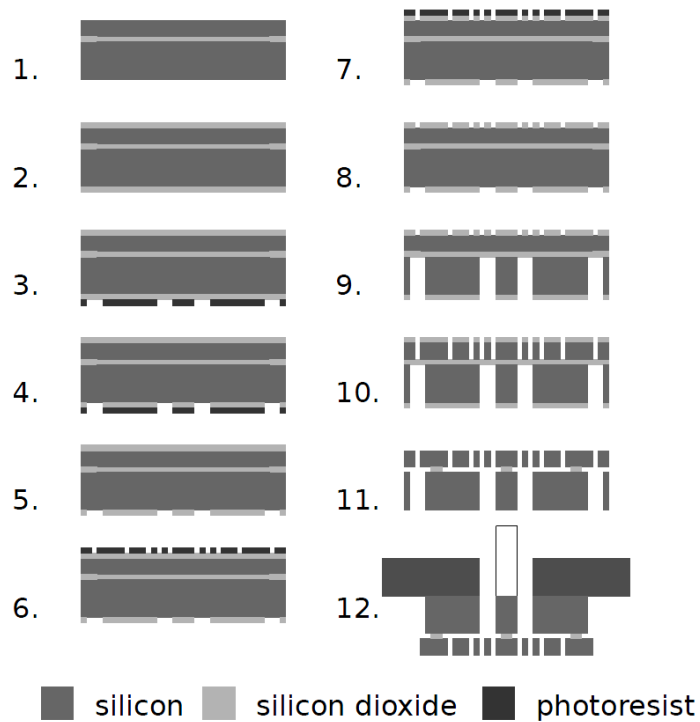


Masks			
1	6DOF FORCE/TORQUE SENSOR DENNIS ALVERINGH HANDLE v5.144	Non-Inverted/Inside Black	Mirrored
2	6DOF FORCE/TORQUE SENSOR DENNIS ALVERINGH DEVICE v5.144	Non-Inverted/Inside Black	Non-Mirrored

Chips location (handle layer up)



**Process outline**



Process	
1	SOI wafer
2	Oxidation
3	Lithography of handle layer
4	Etching of oxide of the handle layer
5	Resist stripping
6	Lithography of device layer
7	Etching of oxide of device layer
8	Resist stripping
9	Etching of handle layer
10	Etching of device layer
11	Release etch
12	Final assembly

Wafers		
2x	<b>SOI wafer</b>	Device layer: 50 $\mu\text{m}$ Box layer: 4 $\mu\text{m}$ Handle layer: 400 $\mu\text{m}$ Size: 100 mm Doping: P-type
10x	<b>Dummy wafers</b>	Size: 100 mm Doping: P-type Polished: OSP Orientation: <100>

**Process flow**

Pre-furnace cleaning		
<b>1</b>	<b>Clean HNO3-1</b> (#clean102)	NL-CLR-WB14 <ul style="list-style-type: none"> <li>• beaker 1: HNO<sub>3</sub> (99%) 5min</li> </ul>
<b>2</b>	<b>Clean HNO3-2</b> (#clean138)	NL-CLR-WB14 <ul style="list-style-type: none"> <li>• beaker 2 : HNO<sub>3</sub> (99%) 5min</li> </ul>
<b>3</b>	<b>Quick Dump Rinse (QDR)</b> (#clean119)	NL-CLR-Wet benches Recipe 1 QDR: 2 cycles of steps 1 till 3, 1- fill bath 5 sec 2- spray dump 15 sec 3- spray-fill 90 sec 4- end fill 200 sec Recipe 2 cascade rinsing: continuous flow Rinse till the DI resistivity is > 10 ΩM
<b>4</b>	<b>Clean HNO3-3a/b</b> (#clean 118)	NL-CR-WB14 beaker 3a/b: HNO <sub>3</sub> (69%), <ul style="list-style-type: none"> <li>• temp 95°C,</li> <li>• time &gt; 10min</li> </ul>
<b>5</b>	<b>Quick Dump Rinse (QDR)</b> (#clean119)	NL-CLR-Wet benches Recipe 1 QDR: 2 cycles of steps 1 till 3, 1- fill bath 5 sec 2- spray dump 15 sec 3- spray-fill 90 sec 4- end fill 200 sec Recipe 2 cascade rinsing: continuous flow Rinse till the DI resistivity is > 10 ΩM
<b>6</b>	<b>Substrate drying</b> (#clean120)	NL-CLR-WB Single wafer dryer <ul style="list-style-type: none"> <li>• speed: 2500 rpm, 60 sec with 30 sec N<sub>2</sub> flow</li> </ul>
Oxidation		
<b>7</b>	<b>Wet Oxidation of Silicon</b> @ 1150°C (#film114)	NL-CLR- Furnace B2 Standby temperature: 800°C Check water level of bubbler Check water temp. 85 °C Program: WET1150B <ul style="list-style-type: none"> <li>• Temp.: 1150°C</li> <li>• Gas: H<sub>2</sub>O + N<sub>2</sub> (Bubbler)</li> <li>• N2 Flow: 2 liter/min</li> <li>• Ramp: 10 °C/min</li> <li>• Cooldown: 7.5 °C/min</li> </ul>
		Time: 14 hour. Aimed thickness: 2100 nm.

Lithography of handle layer			
<b>8</b>	<b>Dehydration bake</b> (#lith102)	NL-CLR-WB21/22 dehydration bake at hotplate <ul style="list-style-type: none"> <li>temp. 120°C</li> <li>time: 5min</li> </ul>	Continue immedialy with priming the step! Handle layer.
<b>9</b>	<b>Priming (liquid)</b> (#lith101)	NL-CLR-WB21/22 Primer: HexaMethylDiSilazane (HMDS) use spincoater: <ul style="list-style-type: none"> <li>program: 4000 (4000rpm, 30sec)</li> </ul>	
<b>10</b>	<b>Coating Olin Oir 907-17</b> (#lith105)	NL-CLR-WB21 Coating: Primus spinner <ul style="list-style-type: none"> <li>olin oir 907-17</li> <li>spin Program: 4000 (4000rpm, 30sec)</li> </ul> Prebake: hotplate <ul style="list-style-type: none"> <li>time 90 sec</li> <li>temp 95 °C</li> </ul>	Speed: 3000 rpm. Aimed thickness: 2000 nm.
<b>11</b>	<b>Alignment &amp; Exposure Olin OiR 907-17</b> (#lith121)	NL-CLR- EV620 Electronic Vision Group EV620 Mask Aligner <ul style="list-style-type: none"> <li>Hg-lamp: 12 mW/cm<sup>2</sup></li> <li>Exposure Time: 4sec</li> </ul>	
<b>12</b>	<b>Development Olin OiR resist</b> (#lith111)	NL-CLR-WB21 After exposureBake : hotplate <ul style="list-style-type: none"> <li>time 60sec</li> <li>temp 120°C</li> </ul> development: developer: OPD4262 <ul style="list-style-type: none"> <li>time: 30sec in beaker 1</li> <li>time: 15-30sec in beaker 2</li> </ul>	
<b>13</b>	<b>Quick Dump Rinse (QDR)</b> (#clean119)	NL-CLR-Wet benches Recipe 1 QDR: 2 cycles of steps 1 till 3, 1- fill bath 5 sec 2- spray dump 15 sec 3- spray-fill 90 sec 4- end fill 200 sec Recipe 2 cascade rinsing: continuous flow Rinse till the DI resistivity is > 10 ΩM	
<b>14</b>	<b>Substrate drying</b> (#clean120)	NL-CLR-WB Single wafer dryer <ul style="list-style-type: none"> <li>speed: 2500 rpm, 60 sec with 30 sec N<sub>2</sub> flow</li> </ul>	
<b>15</b>	<b>Inspection by optical microscope</b> (#metro101)	NL-CLR- Nikon Microscope <ul style="list-style-type: none"> <li>dedicated microscope for lithography inspection</li> </ul>	No hard bake!

Etching of oxide of the handle layer

**16 DRIE of multilayers** NL-CLR-Adixen SE Thickness:  
(#etch174) Application: directional etch of SiRN or SiO2 2000 nm.  
Nickname: "Roberts" process Time: 6 min.

Parameters	Value
Argon (sccm)	100
CHF3 (sccm)	100
APC %	100
ICP (Watt)	1200
CCP (Watt) Rf	150 (Vde=580V)
SH (mm)	200
Electrode temp.	-100 +20 °C
He (bar)	10
Etch rate Oir resist	160 nm/min
Etch rate SiO2	250 nm/min
Etch rate silicon	70-80 nm/min

**17 Stripping of resist in oxygen plasma** NL-CLR- Tepla 300E  
(#lith117) • Barrel Etcher (2.45 GHz)  
• Multipurpose sytem  
• O<sub>2</sub> flow: 200sccm (50%)  
• Power: 500W  
• Pressure: 1.2 mbar  
Values for olin oir resist:  
• Time: 10 min for 1-3 wafers, 400 nm/min  
• Time: 20 min for 4-10 wafers  
• End point detection by visual inspection of the plasma color.  
• Blue color means still photoresist on the wafer, purple means clean.

Lithography of device layer			
<b>18</b>	<b>Dehydration bake</b> (#lith102)	NL-CLR-WB21/22 dehydration bake at hotplate <ul style="list-style-type: none"> <li>temp. 120°C</li> <li>time: 5min</li> </ul>	Continue immedialy with priming the step! Device layer.
<b>19</b>	<b>Priming (liquid)</b> (#lith101)	NL-CLR-WB21/22 Primer: HexaMethylDiSilazane (HMDS) use spincoater: <ul style="list-style-type: none"> <li>program: 4000 (4000rpm, 30sec)</li> </ul>	
<b>20</b>	<b>Coating Olin Oir 907-17</b> (#lith105)	NL-CLR-WB21 Coating: Primus spinner <ul style="list-style-type: none"> <li>olinoir 907-17</li> <li>spin Program: 4000 (4000rpm, 30sec)</li> </ul> Prebake: hotplate <ul style="list-style-type: none"> <li>time 90 sec</li> <li>temp 95 °C</li> </ul>	Speed: 3000 rpm. Aimed thickness: 2000 nm
<b>21</b>	<b>Alignment &amp; Exposure Olin OiR 907-17</b> (#lith121)	NL-CLR- EV620 Electronic Vision Group EV620 Mask Aligner <ul style="list-style-type: none"> <li>Hg-lamp: 12 mW/cm<sup>2</sup></li> <li>Exposure Time: 4sec</li> </ul>	
<b>22</b>	<b>Development Olin OiR resist</b> (#lith111)	NL-CLR-WB21 After exposurebBake : hotplate <ul style="list-style-type: none"> <li>time 60sec</li> <li>temp 120°C</li> </ul> development: developer: OPD4262 <ul style="list-style-type: none"> <li>time: 30sec in beaker 1</li> <li>time: 15-30sec in beaker 2</li> </ul>	
<b>23</b>	<b>Quick Dump Rinse (QDR)</b> (#clean119)	NL-CLR-Wet benches Recipe 1 QDR: 2 cycles of steps 1 till 3, 1- fill bath 5 sec 2- spray dump 15 sec 3- spray-fill 90 sec 4- end fill 200 sec Recipe 2 cascade rinsing: continuous flow Rinse till the DI resistivity is > 10 ΩM	
<b>24</b>	<b>Substrate drying</b> (#clean120)	NL-CLR-WB Single wafer dryer <ul style="list-style-type: none"> <li>speed: 2500 rpm, 60 sec with 30 sec N<sub>2</sub> flow</li> </ul>	
<b>25</b>	<b>Inspection by optical microscope</b> (#metro101)	NL-CLR- Nikon Microscope <ul style="list-style-type: none"> <li>dedicated microscope for lithography inspection</li> </ul>	No hard bake!

Etching of oxide of the device layer

**26 DRIE of multilayers** NL-CLR-Adixen SE Thickness: 2000 nm.  
 (#etch174) Application: directional etch of SiRN or SiO2  
 Nickname: "Roberts" process

Parameters	Value
Argon (sccm)	100
CHF3 (sccm)	100
APC %	100
ICP (Watt)	1200
CCP (Watt) Rf	150 (Vde=580V)
SH (mm)	200
Electrode temp.	-100 +20 °C
He (bar)	10
Etch rate Oir resist	160 nm/min
Etch rate SiO2	250 nm/min
Etch rate silicon	70-80 nm/min

**27 Stripping of resist in oxygen plasma** NL-CLR- Tepla 300E  
 (#lith117) • Barrel Etcher (2.45 GHz)  
 • Multipurpose sytem  
 • O<sub>2</sub> flow: 200sccm (50%)  
 • Power: 500W  
 • Pressure: 1.2 mbar  
 Values for olinoir resist:  
 • Time: 10 min for 1-3 wafers, 400 nm/min  
 • Time: 20 min for 4-10 wafers  
 • End point detection by visual inspection of the plasma color.  
 • Blue color means still photoresist on the wafer, purple means clean.

Etching of the handle layer

**28 DRIE of Si** NL-CLR-Adixen SE Thickness: 400 µm.  
 (custom recipe) Aspect Ratio Controled Etching (No RIE lag) Until box layer is visible.  
 Time: 37 min.

Parameters	Etch	Deposition
Gas	SF6	C4F8
Flow sccm	500	175
Time sec	4	0.5
Priority	2	1
APC %	16.5	16.5
ICP Watt	2500	2500
CCP Watt [LF]	50	50
Pulsed (LF) ms	10on/90off	10on/90 off
He mBar	10	10
SH mm	110	110
Electrode temp.°C.	-40	-40

**Etching of the device layer**

<b>29</b>	<b>DRIE of Si</b> (custom recipe)	NL-CLR-Adixen SE			Thickness: 50 µm.
		Aspect Ratio Controlled Etching (No RIE lag)			Until box layer is visible. Time: 17 min.
		<b>Parameters</b>	<b>Etch</b>	<b>Deposition</b>	
		Gas	SF6	C4F8	
		Flow sccm	550	200	
		Time sec	6	2	
		Priority	2	1	
		APC %	100	100	
		ICP Watt	1500	1500	
		CCP Watt [LF]	100	100	
		Pulsed (LF) ms	10on/90off	10on/90 off	
		He mBar	10	10	
		SH mm	200	200	
		Electrode	-10	-10	
		temp.°C.			

**Removal of C4F8 using O2 plasma and piranha cleaning**

<b>30</b>	<b>Stripping resist in piranha private use (#lith195)</b>	NL-CLR-WB09	Application: stripping of resist		
			Mixture: H <sub>2</sub> SO <sub>4</sub> :H <sub>2</sub> O <sub>2</sub> (3:1) vol%		
			<ul style="list-style-type: none"> <li>• add H<sub>2</sub>O<sub>2</sub> slowly! to H<sub>2</sub>SO<sub>4</sub> (exothermic process!!)</li> <li>• due to mixing the temperature will increase to .....130°C</li> <li>• adjust the hotplate at 85 °C,</li> <li>• temperature: 130°C</li> <li>• time: depends in application ( 10- 30min)</li> </ul>		
<b>31</b>	<b>Stripping of resist in oxygen plasma (#lith142)</b>	NL-CLR-Tepla300	Barrel Etcher (2.45 GHz)		
			Ultra clean system only (no metals except Al)		
			See list with recipes in CR		
			<ul style="list-style-type: none"> <li>• O<sub>2</sub> flow: 200sccm (50%)</li> <li>• Power: up to 1000W</li> <li>• Pressure: 1 mbar</li> </ul>		

Pre-furnace cleaning		
<b>32</b>	<b>Clean HNO3-1</b> (#clean102)	NL-CLR-WB14 <ul style="list-style-type: none"> <li>• beaker 1: HNO<sub>3</sub> (99%) 5min</li> </ul>
<b>33</b>	<b>Clean HN03-2</b> (#clean138)	NL-CLR-WB14 <ul style="list-style-type: none"> <li>• beaker 2 : HNO<sub>3</sub> (99%) 5min</li> </ul>
<b>34</b>	<b>Quick Dump Rinse (QDR)</b> (#clean119)	NL-CLR-Wet benches Recipe 1 QDR: 2 cycles of steps 1 till 3, 1- fill bath 5 sec 2- spray dump 15 sec 3- spray-fill 90 sec 4- end fill 200 sec Recipe 2 cascade rinsing: continuous flow Rinse till the DI resistivity is > 10 ΩM
<b>35</b>	<b>Clean HNO3-3a/b</b> (#clean 118)	NL-CR-WB14 beaker 3a/b: HNO <sub>3</sub> (69%), <ul style="list-style-type: none"> <li>• temp 95°C,</li> <li>• time &gt; 10min</li> </ul>
<b>36</b>	<b>Quick Dump Rinse (QDR)</b> (#clean119)	NL-CLR-Wet benches Recipe 1 QDR: 2 cycles of steps 1 till 3, 1- fill bath 5 sec 2- spray dump 15 sec 3- spray-fill 90 sec 4- end fill 200 sec Recipe 2 cascade rinsing: continuous flow Rinse till the DI resistivity is > 10 ΩM
<b>37</b>	<b>Substrate drying</b> (#clean120)	NL-CLR-WB Single wafer dryer <ul style="list-style-type: none"> <li>• speed: 2500 rpm, 60 sec with 30 sec N<sub>2</sub> flow</li> </ul>
<b>38</b>	<b>Quick Dump Rinse (QDR)</b> (#clean119)	NL-CLR-Wet benches Recipe 1 QDR: 2 cycles of steps 1 till 3, 1- fill bath 5 sec 2- spray dump 15 sec 3- spray-fill 90 sec 4- end fill 200 sec Recipe 2 cascade rinsing: continuous flow Rinse till the DI resistivity is > 10 ΩM
<b>39</b>	<b>Substrate drying</b> (#clean120)	NL-CLR-WB Single wafer dryer <ul style="list-style-type: none"> <li>• speed: 2500 rpm, 60 sec with 30 sec N<sub>2</sub> flow</li> </ul>

Evaporating the rest of C4F8

<b>40</b>	<b>Wet Oxidation of Silicon at 800°C</b> (#film142)	NL-CLR-Furnace B2 Standby temperature: 800°C Check water level of bubbler Check water temp. 85 °C Program: Standby <ul style="list-style-type: none"><li>• Temp.: 800°C</li><li>• Gas: H<sub>2</sub>O + N<sub>2</sub> (Bubbler)</li><li>• N<sub>2</sub> Flow: 2 liter/min</li><li>• Ramp: 10 °C/min</li><li>• Cooldown: 7.5 °C/min</li><li>• Cooldown: 7.5 °C/min</li></ul>	Time: 1 hour.
-----------	--	---	---------------

Release etch

<b>41</b>	<b>Etching in HF 50%</b> (#etch130)	NL-CLR-WB9 or10 Use private beaker : HF 50% standard <ul style="list-style-type: none"><li>• temp.: 20°C</li></ul> Etchrates: <ul style="list-style-type: none"><li>• Si<sub>3</sub>N<sub>4</sub>-H<sub>2</sub> = 0.64 nm/min</li><li>• SiRN-G3<sup>#</sup> (nanolab) = 3.1 - 3.5 nm/min</li><li>• SiO<sub>2</sub> = 1 μm/min</li></ul>	Time: 2 min. Etch until structures are almost released.
<b>42</b>	<b>Quick Dump Rinse (QDR)</b> (#clean119)	NL-CLR-Wet benches Recipe 1 QDR: 2 cycles of steps 1 till 3, 1- fill bath 5 sec 2- spray dump 15 sec 3- spray-fill 90 sec 4- end fill 200 sec Recipe 2 cascade rinsing: continuous flow Rinse till the DI resistivity is > 10 ΩM	
<b>43</b>	<b>Vapor HF etching of SiO<sub>2</sub></b> # etch171	NL-CLR-WB-4 Idonius Vapor HF Tool	Time: 30 min. Check under etch.

